Coordinated Control of Two Macro / Micro Manipulators for Fiber Pigtailing Automation

by

Brandon W. Gordon

B.A.Sc., Mechanical Engineering
University of Waterloo, 1994

Submitted to the Department of
Mechanical Engineering
in Partial Fulfillment of the Requirements
for the Degree of

Master of Science as Recommended by the Department of
Mechanical Engineering

at the

MASSACHUSETTS INSTITUTE OF TECHNOLOGY
May 14, 1996

Signature of Author_____
Department of Mechanical Engineering
May 14, 1996

Certified by_____
Dr. Andre Sharon
Executive Officer, The Manufacturing Institute
Thesis Supervisor

Accepted by_____
Prof. Ain A. Sonin
Chairman, Departmental Graduate Committee

Coordinated Control of Two Macro / Micro Manipulators for Fiber Pigtailing Automation

by

Brandon W. Gordon

Submitted to the Department of Mechanical Engineering
on May 14, 1996 in partial fulfillment of the requirements for the
Degree of Master of Science, Mechanical Engineering

ABSTRACT

An investigation into the control of two macro/micro manipulators for an automated fiber pigtailing process is presented. This process involves the alignment of three fibers to an optoelectronic device with submicron accuracy in a minimum amount of time using the coordinated motions of two macro/micro manipulators. The macro/micro architecture employed consists of a five-bar micro manipulator controlled with piezoelectric actuators carried by a macro manipulator composed of a five-bar mechanism and a linear stage.

A mathematical model of the macro manipulator that includes transmission flexibility of harmonic drive gears, static and Coulomb friction, and presliding displacement is developed. Both simulations and experiments revealed a backlash type effect due to transmission windup of the flexible gearing under the influence of frictional loading which resulted in a substantial deviation of output position at the micron level. To improve accuracy a transmission windup compensation technique is developed based on estimation of the transmission windup from previous input. It is experimentally shown that this method reduces the effects of transmission windup by an order of magnitude.

Furthermore, a new alignment method for pigtailing optoelectronic devices is presented which employs a large diameter core sensing fiber to decouple an inherently four dimensional search process into successive two dimensional searches. This method is shown to reduce the time required by over two orders of magnitude while substantially increasing robustness to process uncertainties.

Thesis Supervisor: Dr. Andre Sharon
Title: Executive Officer of The Manufacturing Institute

Dedicated to My Parents

Acknowledgments

I would like to thank ARPA (Advanced Research Projects Agency) and Air Force-Rome Laboratories for sponsoring the Automated Fiber Pigtailing Machine (AFPM) Program, and the members of the AFPM consortium for their collaboration: Lawrence Livermore National Laboratories, Uniphase Telecommunications Products, Ortel Corporation, and Newport/Klinger Corporation.

I would like to thank Dr. Sharon for providing me with one intense robotic experience. That mud slide always seemed so close but yet so far away.

I would also like to thank my partner in crime Tiina Hämeenanttila for designing and building the micro manipulator and for all those other little things.

I would like to thank K.C. Ross at UTP for continuing the AFPM tradition.

I would like to thank Morris Fresko for designing and building the macro manipulators.

Furthermore, I would like to thank Charles, Wayne (I and II), Steve, and the rest of the lab for making my stay more enjoyable.

And finally, I would like to thank Bungie software for creating my favourite lab pastime.

TABLE OF CONTENTS

LIST OF FIGURES

1. Introduction

1.1 Background

The ability to manufacture low cost, high performance optoelectronic devices is becoming increasingly important as systems that rely on optoelectronic technology to enhance performance become more prevalent in industry. The process of attaching optical fibers to optoelectronic devices, referred to as "pigtailing", represents one of the key challenges facing the optoelectronic manufacturing industry. This process often requires submicron alignment accuracy and is usually performed manually under a microscope by highly trained technicians resulting in a low throughput process that is too costly for high volume manufacturing. It is estimated that the costs associated with packaging/pigtailing operations will eventually represent greater than 90% of the total cost of a packaged optoelectronic device for high volume applications without some improved form of automation.

To address this need an Automated Fiber Pigtailing Machine (AFPM) was developed at MIT in collaboration with Lawrence Livermore National Laboratory (LLNL) over a two year period with the objective of substantially reducing the cost of pigtailing optoelectronic devices. Figure 1.1 shows a schematic of the process. The integrated optical chips (IOC) and fiber coils are placed in a tray that is carried by a conveyor belt until it is in the workspace of two five degree of freedom manipulators. The manipulators then pickup the input and output fibers, get epoxy adhesive, and align the fibers to the device with submicron accuracy.

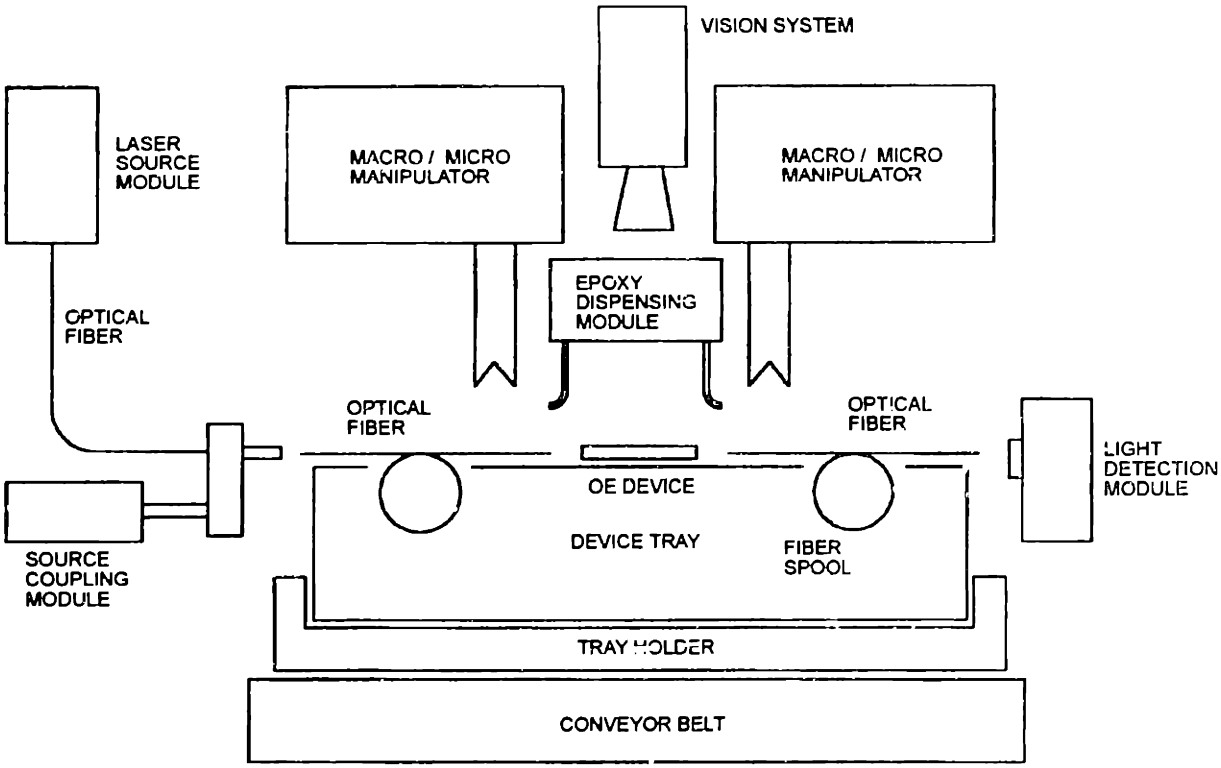

Figure 1.1 System Schematic for the AFPM process

The central feature of the AFPM are the two five degree of freedom manipulators which employ a macro/micro architecture. This configuration consists of a high resolution, high bandwidth micro manipulator with a small range of motion carried by a slower, less accurate macro manipulator with a large range of motion. Together this arrangement has the range of the macro manipulator required for fiber processing with the high resolution and high bandwidth of the micro manipulator needed for optical alignment. Macro/micro manipulators have been shown [1] to provide an inherently stable dynamic architecture for high-bandwidth, high resolution positioning at a relatively low cost. Figure 1.2 illustrates the design. The macro manipulator consists of a five bar mechanism actuated by servo motors through harmonic drives carried by a linear stage actuated by a belt driven

lead screw. The micro manipulator is a five bar flexible structure controlled by bimorph piezoelectric actuators.

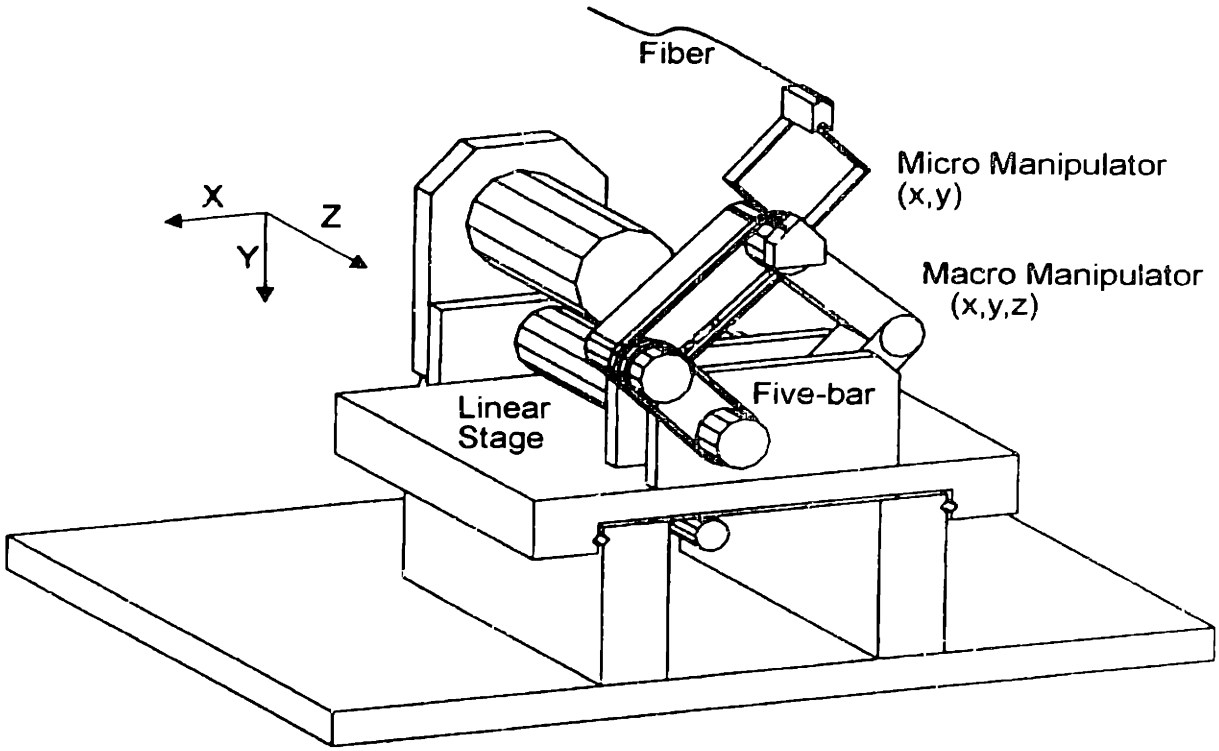

Figure 1.2 The Macro / Micro Manipulator Design

Three forms of feedback are employed to guide the macro/micro manipulators in the alignment process. The macro manipulator is controlled by closed loop encoder feedback. The micro manipulator is controlled using a an external closed feedback loop based on light intensity throughput measured through the optoelectronic device. In addition, a vision system is employed to guide the coarse alignment of the fibers. The production rate of the automated pigtailing process is highly dependent on the time required to perform optical alignment. This process must be performed in less than 90 seconds per fiber to achieve necessary productivity levels.

Coordinated control of the two macro/micro manipulators to achieve alignment in a minimum amount of time is a challenging task. High

performance low level control is required to rapidly move the macro manipulator. A four dimensional space must be quickly searched to initiate light coupling through the optoelectronic device. Further, on-line light throughput maximization using the micro manipulator is needed to achieve final alignment. The objective of this thesis is to develop control and trajectory planning algorithms that allow the alignment process to be carried out in a minimum amount of time. Furthermore, two novel nonlinear control techniques are developed that can substantially enhance performance of precision machines.

1.2 Thesis Organization

This thesis is organized as follows. In chapter 2 a mathematical model of the macro manipulator is developed to gain insight into the dynamics of the system. This leads to the development of an optimal controller for the macro manipulator. It is shown that the interaction of transmission flexibility of the harmonic drive motors employed in the macro manipulator with friction present produces a transmission windup effect that introduces backlash into the system. A model of this effect is made and is used to develop a compensation method that linearizes the harmonic drive response. An investigation into the resolution capability of the macro manipulator is also performed.

Chapter 3 develops trajectory planning algorithms for the pigtailing alignment process. It is shown that the introduction of a large diameter core fiber area sensor substantially improves robustness of the process and greatly reduces the time required for an alignment.

An investigation of two promising nonlinear control methods for precision applications is presented in chapter 4. In particular, a feed forward neural network controller is developed that can linearize the hysteresis behavior of

piezoelectric actuators employed in the micro manipulator. Further, a controller that uses torque impulses to move the macro manipulator very small increments is developed. Using this control method it is possible to improve the resolution of a precision machine by more than an order of magnitude.

Concluding statements are presented in Chapter 5.

2. Control of the Macro Manipulator

2.1 Introduction

The macro manipulator design is illustrated in Figure 2.1. The macro is a three degree of freedom manipulator that is capable of X-Y-Z motion in a 25mm workspace with fixed orientation at the endpoint. X-Y planar motion is achieved using a five-bar mechanism with two base links driven by harmonic drive DC motors with an 80:1 gear reduction. To maintain constant orientation two timing belts are connected in series between the endpoint and the base of the five-bar. This low inertia arrangement allows rapid motion and a relatively high bandwidth for a machine with the micro's 5nm resolution in a very compact package. Motion in the Z direction is achieved by a linear stage that carries the five-bar. The linear stage is driven by a 40 thread per inch lead screw which in turn is driven by a 5:1 timing belt connected to a DC motor. This design achieves high resolution with relatively small amounts of backlash. The motors of the macro manipulator are digitally controlled by a PC which employs encoder position feedback.

In this chapter a mathematical model of the macro manipulator is developed that accounts for frictional effects, transmission flexibility and presliding displacement of the output. An optimal controller based on the PID controller structure and ITAE (integral of time multiplied by the absolute error) performance index is also developed. Further, it is shown that the interaction of transmission flexibility of the harmonic drive motors employed in the macro manipulator with friction present produces a transmission windup effect that introduces backlash into the system. A model of this effect is made and is used to develop a compensation method that linearizes the harmonic drive response. An investigation into the critical resolution capability of the macro manipulator is also presented.

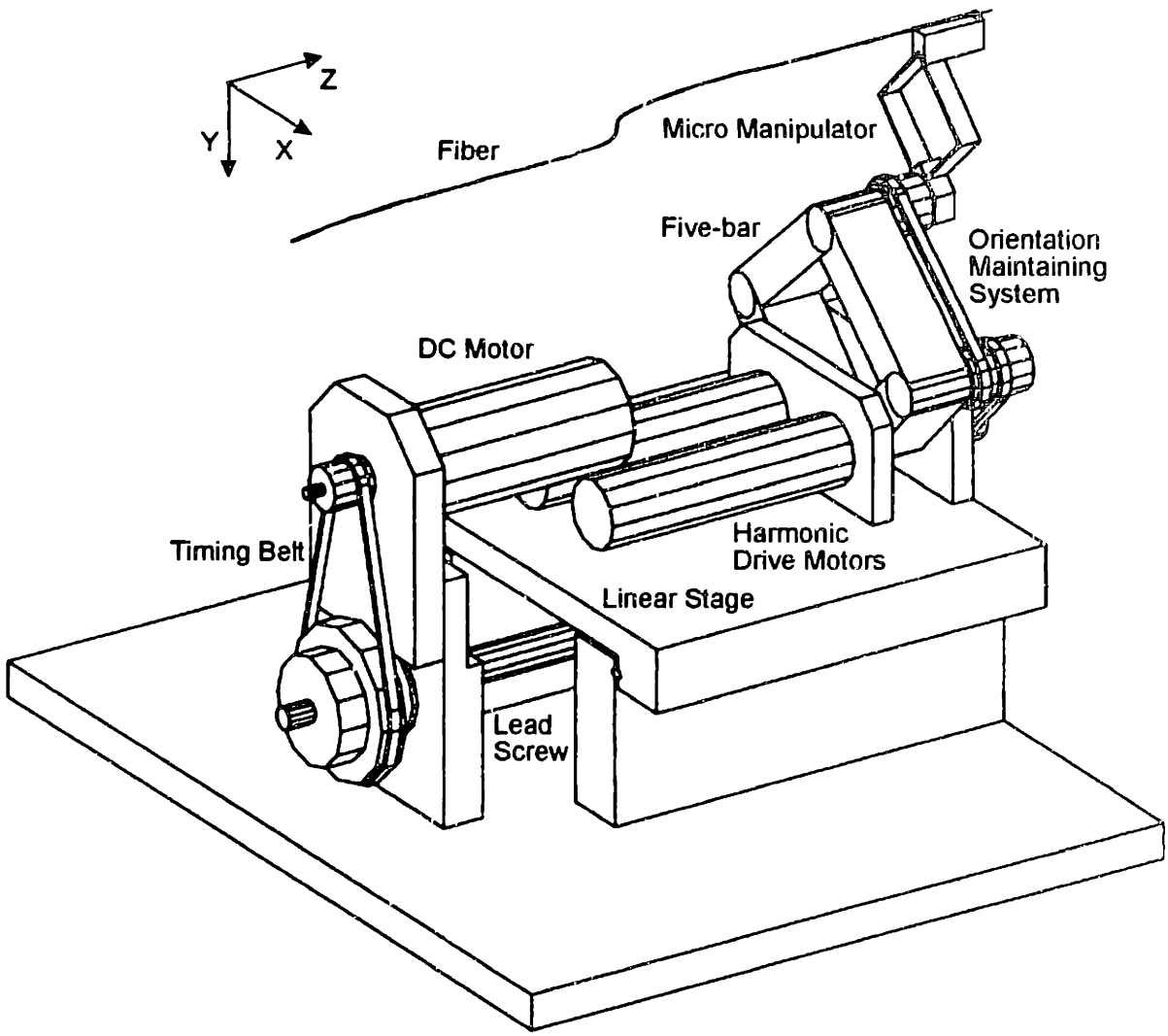

Figure 2.1 The Macro Manipulator

2.2 Mathematical Model of the Macro Manipulator

A mathematical model of the macro manipulator was constructed to provide insight into the dynamics of system and to facilitate control system design. In the development of the equations of motion for the system it is assumed that the motion of the micro manipulator has negligible effect on the motion of the macro manipulator. This assumption is valid because the mass of the micro and payload is far less than the mass of the macro.

Another assumption that will be made is that the dynamics of the three motor axes are uncoupled. This is valid for the five-bar because of the high gear ratio employed in the harmonic drive motors (80:1) which effectively divides load torques by the gear ratio and the five-bar mechanism inertia terms by the gear ratio squared. Thus the coupling centripetal and Coriolis terms in the dynamics of the five-bar mechanism act as small disturbances to the motor output. Frictional coupling in the five bar joints, however, could have an effect on the motion of the links. This effect will be experimentally investigated later in this chapter. The z-stage dynamics are decoupled from the five-bar because it employs a high pitch lead screw (40 threads/in) combined with a timing belt reduction (5:1) that greatly reduces load disturbances. The dynamics of the orientation system will also be neglected since they have relatively high frequency and are not actively controlled. Furthermore, the natural frequencies associated with the bearings and interfacial contacts of the macro are much greater than the control system and do not effect positioning at the scale of the macro resolution (~1um). It should be noted that the kinematics of the macro manipulator are coupled and forward and inverse kinematics routines are employed in the trajectory generation algorithms to convert between Cartesian and joint coordinates.

Figure 2.2 shows a free body diagram of the independent joint model. The control input torque T_m from the motor acts on the motor inertia J_m which is connected via a gear reduction r to the load inertia J_l. The intrinsic flexibility of the timing belt and the harmonic drive motors play a significant role in the system dynamics and are modeled using a torsional spring that produces a torque T_s. Static, Coulomb and viscous frictional torques on the motor F_m and the load F_l have a strong influence on the system. These significant levels occur as a result of intrinsic properties of the harmonic drives and the tight tolerances used in the lead screw and five-bar to avoid backlash. Furthermore, there are no significant disturbance torques on the system.

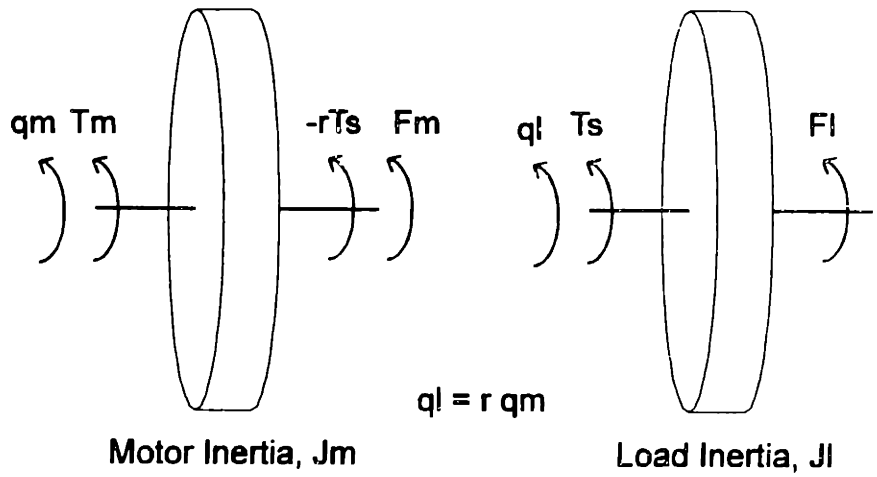

Figure 2.2 Free Body Diagram of the Independent Joint Model

From the free body diagram the acceleration of the two inertia can be found:

$$J_m\ddot{q}_m = T_m - rT_s + F_m \tag{2.1}$$

$$J_l\ddot{q}_l = T_s + F_l \tag{2.2}$$

where q_m and q_l are the positions of the motor and load inertia.

The equation for the torque of a DC motor is given by:

$$T_m = k_m i(t) \tag{2.3}$$

where k_m is the motor torque constant and i(t) the motor current. The motor amplifiers employed with the system act as voltage sources so a relation between the voltage and current is required. Since the electrical time constant (L/R) of both motors is small compared to the system bandwidth the motor inductance can be neglected in which case the current is given by:

$$i(t) = \frac{u(t) - k_b \dot{q}_m}{R} \tag{2.4}$$

where the command voltage, motor voltage constant (back emf), and winding resistance are given by u(t), k_b, and R respectively. Substituting this result into the previous relation gives:

$$T_m = -\frac{k_m k_b}{R} \dot{q}_m + \frac{k_m}{R} u(t) \tag{2.5}$$

It can be seen from this equation that the main effect of operating the amplifier in voltage mode is to add some damping to the motor dynamics. The tradeoff, however, is that the input gain is now dependent on the winding resistance which can be effected by heat dissipation if the motors are driven hard. The torsional spring torque is given by:

$$T_s = k_s(rq_m - q_l) + k_h(rq_m - q_l)^3 \tag{2.6}$$

where k_s is the spring constant and k_h is an empirically derived term to account for the spring hardening characteristic of the harmonic drive gears. The harmonic drive gear train flexibility is highly nonlinear and according to its specifications the effective spring constant can increase by over a factor of three as loading increases. The frictional torques on the system are:

$$\begin{aligned}
F_m &= -\psi_m \quad \text{if } \dot{q}_m = 0 \ , \ |\psi_m| \le f_{sm} \\
F_m &= -\text{sgn}(\psi_m) f_{sm} \quad \text{if } \dot{q}_m = 0 \ , \ |\psi_m| > f_{sm} \\
F_m &= -\text{sgn}(\dot{q}_m) f_{cm} - b_m \dot{q}_m \quad \text{if } |\dot{q}_m| > 0 \\
\psi_m &= -r\left(k_s(rq_m - q_l) + k_h(rq_m - q_l)^3\right) + \frac{k_m}{R} u(t)
\end{aligned} \tag{2.7}$$

$$
\begin{aligned}
F_l &= -\psi_l \quad \text{if } \dot{q}_l = 0 \ , \ |\psi_l| \le f_{sl} \\
F_l &= -\text{sgn}(\psi_l) f_{sl} \quad \text{if } \dot{q}_l = 0 \ , \ |\psi_l| > f_{sl} \\
F_l &= -\text{sgn}(\dot{q}_l) f_{cl} - b_l \dot{q}_l \quad \text{if } |\dot{q}_l| > 0 \\
\psi_l &= k_s (r q_m - q_l) + k_h (r q_m - q_l)^3
\end{aligned}
\tag{2.8}
$$

where ψ_m and ψ_l are the other external torques on the motor and load inertia. The static and Coulomb coefficients of friction for the two inertia are represented by f_{sm}, f_{sl} and f_{cm}, f_{cl}. These equations represent the effects of viscous damping, stiction and Coulomb friction. The static friction term causes the inertia to stick if the total torque is less than the static friction coefficient. If the inertia is in motion, a constant torque equal to the Coulomb friction coefficient and a viscous torque proportional to the velocity are applied in the reverse direction. In the model it is assumed that the friction parameters are constant. Experimentally it was found that positional dependence and spatial noise is small compared to friction levels over the range of interest. Further, friction is not acceleration dependent in the z-stage since inertial force on the leadscrew is small for typical acceleration rates of the stage.

Combining the previous relations gives the equations of motion for the system:

$$
J_m \ddot{q}_m = F_m - r\, k_s (r q_m - q_l) - r\, k_h (r q_m - q_l)^3 - \frac{k_m k_b}{R} \dot{q}_m + \frac{k_m}{R} u(t) \tag{2.9}
$$

$$
J_l \ddot{q}_l = F_l + k_s (r q_m - q_l) + k_h (r q_m - q_l)^3 \tag{2.10}
$$

where the equations for the frictional torques are given by equations (2.7) and (2.8).

The output of the z-stage is given by:

$$z = Pq_1 \tag{2.11}$$

where P is the lead screw pitch. For the five-bar output it was found that that a presliding displacement phenomena occurred in the motion of the links. This effect is the result of contact compliance in the frictional interface where asperities come into contact and deform as a result of tangential force but do not slide. The result is elastic behavior during stiction mode when the output inertia is stuck. The output moves an extra amount proportional to the force applied until it reaches the critical static friction threshold after which sliding occurs. This phenomena is quite common in frictional mechanisms [3] and elastic displacements can typically be as high as 5um for a steel to steel interface. However, angular motion of robotic links can amplify this motion considerably. The contact stiffness is sufficiently high in this system so that the high frequency dynamics associated with presliding can be modeled using a simple static relationship:

$$q_o = q_1 - \frac{F_1}{k_c} \tag{2.12}$$

where q_o is the joint output and k_c is the contact stiffness. The contact stiffness can be calculated from the expression:

$$k_c = \frac{f_{sl}}{q_p} \tag{2.13}$$

The magnitude of the maximum presliding displacement q_p was found to be 12 encoder tics corresponding to approximately 20um endpoint displacement.

The mathematical model developed in this section is composed of two coupled highly nonlinear second order differential equations. This nonlinear behavior is largely the result of the stiction and Coulomb friction interacting

with the nonlinear torsional spring between the motor and load inertia. The system parameters for the model were estimated from calculations and simple open loop response tests. The model was numerically simulated in C using a fourth order Runge-Kutta method and verified for a number of cases. It was found in sections 2.4 and 4.3 that the model showed close agreement with experimental data over a wide range of operating conditions.

2.3 Controller Design

During the mathematical modeling it was found that the coupling between the motor actuators is negligible due to the large gear ratios employed in the macro manipulator. For this reason each joint may be controlled independently of the other joints. The control of the macro manipulator therefore reduces to three single input single output (SISO) control designs. The well known PID controller structure was chosen for its simplicity, good performance robustness, and the fact that the controller card used has the capability to perform the PID control loop in hardware leaving the host CPU free for trajectory generation and other functions. The PID control law has the form:

$$u(t) = k_p e(t) + k_i \int e(t)dt + k_d \frac{de(t)}{dt} \qquad (2.14)$$

$$e(t) = q_{md}(t) - q_m \qquad (2.15)$$

where e(t) is the error computed from the difference between the desired and actual motor position. The command voltage u(t) is computed from the weighted sum of the error, the integral of the error, and the derivative of the error. The controller board also includes a saturation function that stops

integration when the integral is too large. This reduces overshoot and improves stability.

The design of a PID controller essentially consists of selecting the three coefficients from a three dimensional search space. Very often these parameters are tuned using intuition or heuristic rules of thumb. The engineer tries different parameter combinations until satisfactory performance is achieved. Tuning is often preferred to classical control techniques because it is usually faster and system nonlinearities such as friction substantially reduce the effectiveness of linear methods. However, this technique rarely produces an optimal PID controller. Regions of the search space may be overlooked, the tuning period may not be long enough, and the performance criteria are often not rigorously defined. Furthermore, system nonlinearities such as friction and input saturation can reduce the effectiveness of intuition and heuristic rules. In an effort to automate the gain selection procedure and provide optimal performance a PID autotuning method was developed. This algorithm automatically searches the parameter space in a systematic way to find optimal control gains with respect to some specified performance criteria.

The most important factor in developing an optimal control method is the selection of the performance index to optimize. This determines the characteristics of the optimal performance obtained and affects the convergence rate of the optimization procedure. With these factors in mind the ITAE (integral of time multiplied by the absolute error) performance index [4] for a step input was selected. The cost function has the form:

$$I = \int_0^T t|e(t)|dt \tag{2.16}$$

where T is the desired integration period. This function integrates the absolute error for a step input while the time weighting puts increased

emphasis on errors occurring later in the response. This provides a good trade off between transient performance and steady state error. Furthermore, the ITAE is known to be highly selective with respect to control parameter variations which will help the optimization process to converge rapidly. No penalty is applied for control input activity because it is desired to achieve maximum performance regardless of controller activity or input saturation.

2.3.1 Optimal Controller Search

The optimal controller is determined by minimizing the performance index with respect to the PID parameters. That is:

$$I^{\circ}(k_p^{\circ}, k_i^{\circ}, k_d^{\circ}) = \min_{[k_p, k_i, k_d]} I(k_p, k_i, k_d) \qquad (2.17)$$

This is not a trivial task since the system and cost function are very nonlinear which can result in numerous local minima that a conventional minimization algorithm can get trapped in. To avoid this difficulty a Random Neighborhood Search [6] minimization method was employed. This technique consists of searching randomly in a small area centered on the point of lowest known cost. If the randomly selected gains have a lower cost the point of lowest known cost is replaced with them. The process continues until a desired level of converges occurs. This method has the advantage that if the search area is sufficiently large it will not get trapped in local minima. This makes it highly suitable for control system design where the global minimum is desired.

The Random Neighborhood Search algorithm was implemented on-line to avoid modeling approximations and to provide the most realistic optimal

design. It was found that averaging the performance index from two different step sizes increased the convergence rate by decreasing the number of local minima associated with the mass sticking near the desired position. The results for the five-bar controller are shown in Figure 2.3. This illustration shows the successful steps taken in parameter space as the algorithm converges for three substantially different initial conditions. It is apparent that the algorithm converges for a wide range of starting points. The convergence period was consistently less than 100 iterations or 10 minutes. The optimal PID controllers were digitally implemented on a controller board with a sampling rate of 2500Hz. Since this is more than twenty times the bandwidth of the system digital sampling effects are negligible.

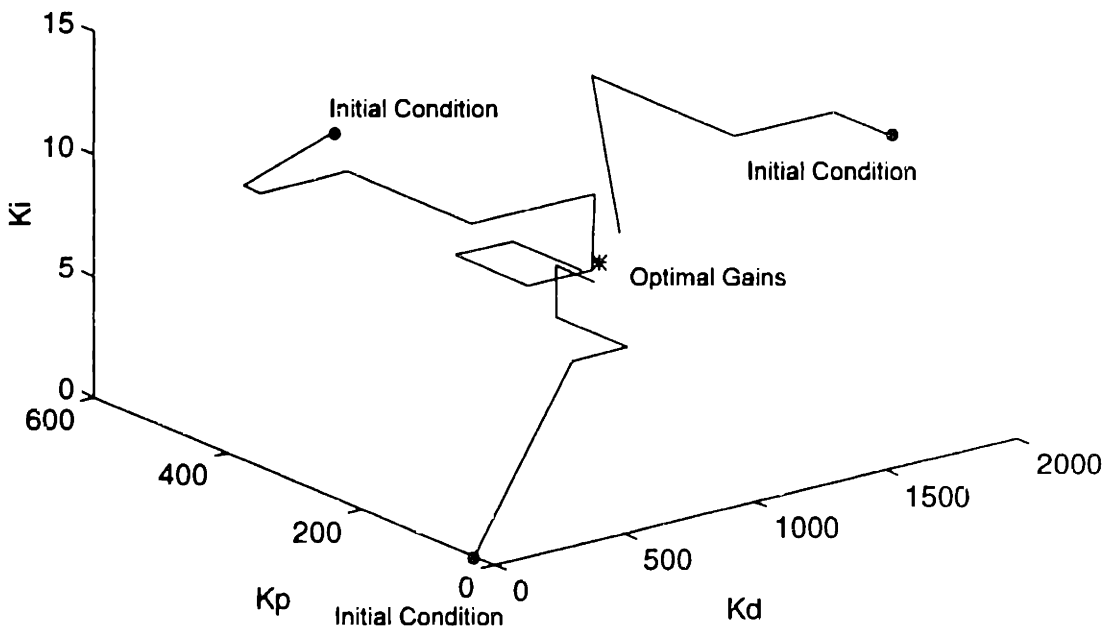

Figure 2.3 Successful Parameter Steps During Optimal Controller Search

2.3.2 Tracking Performance

The tracking response of the step command used for the performance index of the five-bar and the z-stage is shown in Figure 2.4 and Figure 2.5. It can be seen that an impressive settling time of 42ms and rise time of 11ms is achieved for the five-bar. A settling time of 37ms and rise time of 14ms was achieved with the z-stage. The response of the system to 20% smaller kd for the five-bar and 20% smaller ki for the z-stage is also included for comparison. It is apparent that the optimal gains represent a significant improvement over the slightly untuned case. This clearly indicates the advantage of using the autotuning method. The tracking performance of the five-bar to a 10 Hz sinusoidal trajectory is shown in Figure 2.6. It can be seen that the five-bar is able track at 10 Hz with no attenuation and a phase lag of less than 9.9 degrees. The response of the z-stage to a sinusoidal trajectory appears in Figure 2.7. It is apparent that the z-stage is able to track a sinusoidal trajectory of 8 Hz with no attenuation and a phase lag of less than 9.5 degrees.

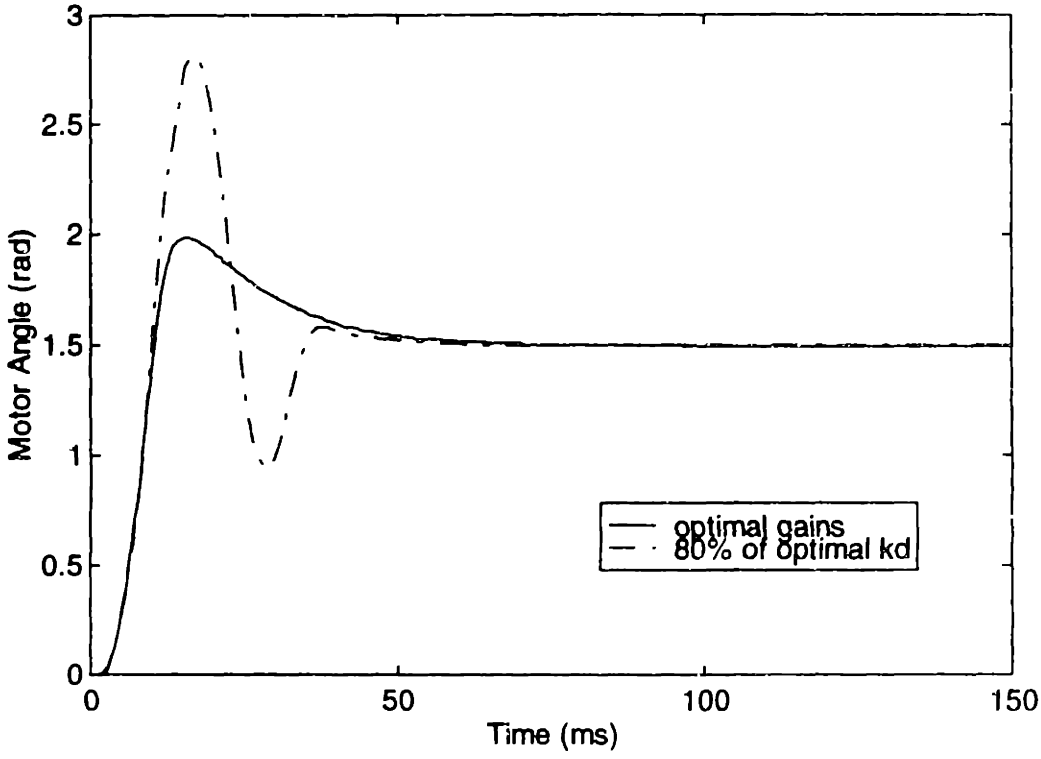

Figure 2.4 Five-bar Step Response

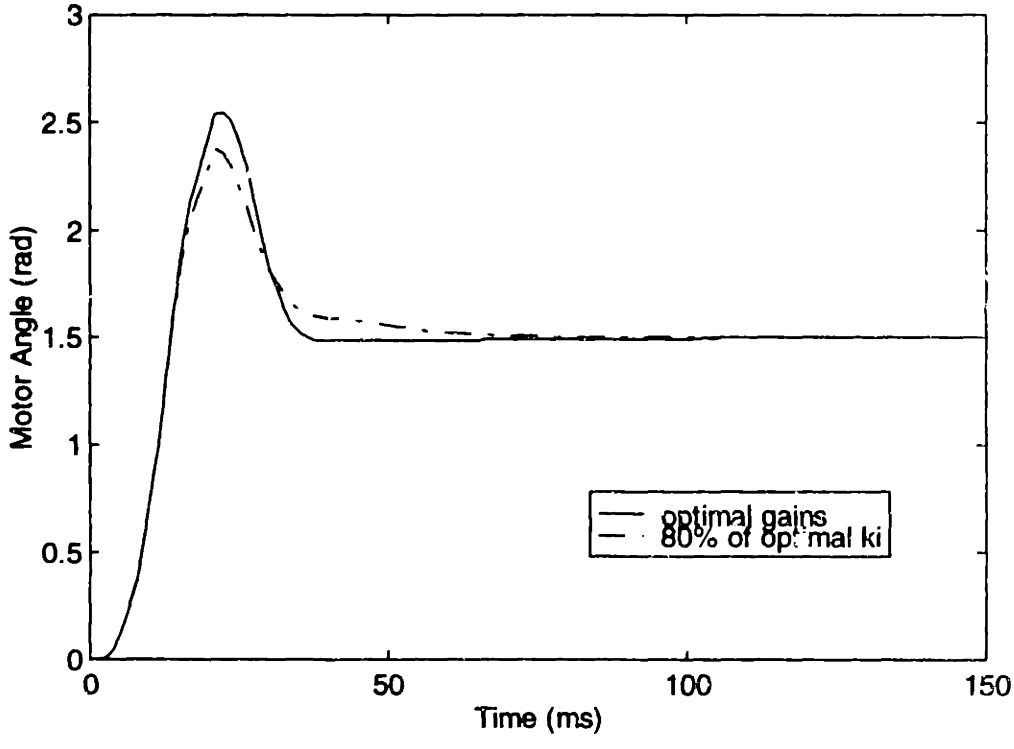

Figure 2.5 Z-stage Step Response

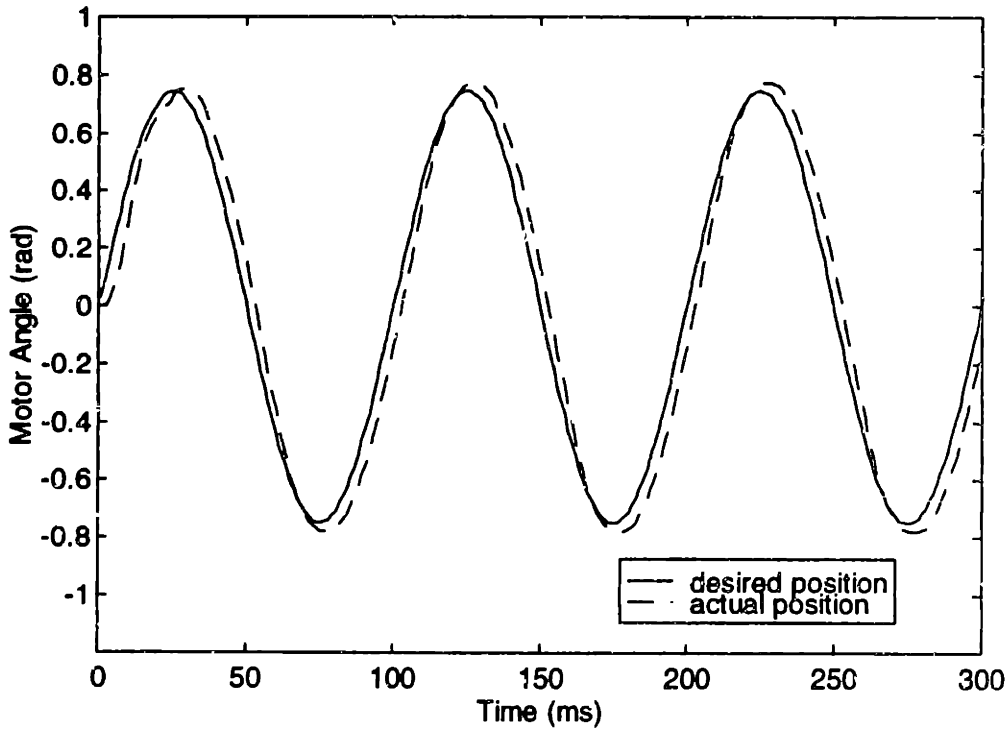

Figure 2.6 Sinusoidal Response of Five-bar

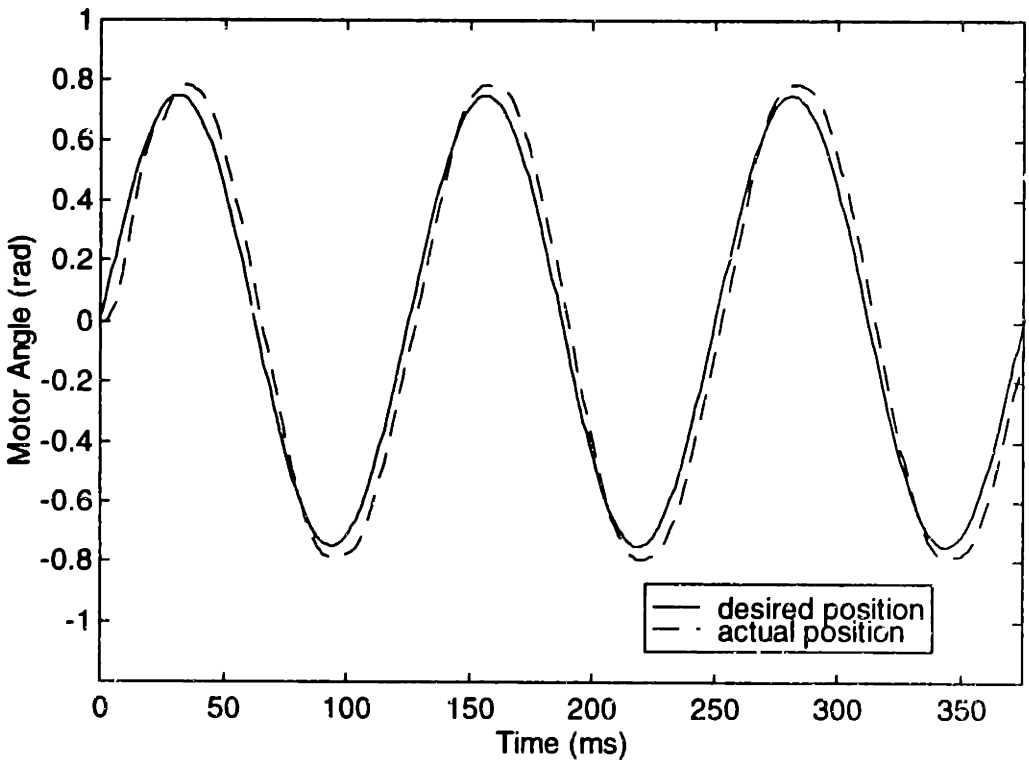

Figure 2.7 Sinusoidal Response of Z-stage

2.4 Transmission Windup Compensation

In experimental tests performed on the macro manipulator a backlash type of behavior was observed between the input to the transmission as read from the motor shaft encoders and the output measured from high accuracy position sensors. It was determined the effect was the result of elastic windup of the flexible transmission under the influence of high frictional torques associated with the output loads of the five-bar joints and the z-stage lead screw. Transmission windup was found to be particularly significant for the five-bar manipulator since the output of the two harmonic drives are kinematically coupled. As a result the five-bar could not travel in a straight line in Cartesian space and the position of the endpoint was highly path dependent which made trajectory planning for the alignment process more difficult to implement. In this section the transmission windup phenomena is investigated and methods to compensate for its effects are examined in order to simplify trajectory planning of the macro manipulator.

2.4.1 Transmission Windup

The effect of transmission windup can be illustrated by plotting the output of the gear train as a function of the input. Figure 2.8 shows a plot of the five-bar response to a forward and backward trajectory over a 700um range. The angles are scaled to approximate endpoint displacements to illustrate the impact of the effect. The input was measured from the motor shaft encoder. The output was measured using capacitance sensors mounted parallel to the five-bar base links. It is apparent that there is a lag in response after a direction reversal but it is not a completely horizontal dead zone that would occur for pure backlash. Instead the reverse trajectory

gradually diverges from the forward as the transmission winds up in the other direction until a maximum value of 100um is achieved. This type of behavior is more difficult to predict and compensate for than pure backlash because the response is dependent on the history of the input whereas for backlash the response is just dependent on the direction of motion.

Transmission windup, as previously mentioned, is the result of frictional loading of the flexible transmission which causes a difference between the motor shaft input and the measured output. This cause was theoretically verified through simulations and also experimentally verified. Simulations of the five-bar mathematical model for three different levels of friction on the output inertia are shown in Figure 2.9. It is evident that the amount of transmission windup increases with the coefficient of friction and that it can be eliminated for very small values. The lack of a completely horizontal dead zone after direction reversals was also observed in the simulations. This was the result of the presliding displacement stiffness interacting with the transmission flexibility. However the simulations predict a linear transition which only approximates the actual curve. This suggests that there could be some other factors involved in this behavior, perhaps nonlinear presliding displacement or some unmodelled dynamics of the harmonic drive gears.

The effect of friction was experimentally verified by measuring the response of a link disconnected from the rest of the five-bar mechanism thus having no load friction. The result is illustrated in Figure 2.10. It is apparent that transmission windup is reduced by more than a factor of ten without frictional loading. The small amount of windup still present could be the result of internal friction in the harmonic drive gearing. Both simulations and experiments suggest that low friction bearings for the five-bar have the capability to eliminate most of the transmission windup effect.

The response of the z-stage to a forward and backward trajectory is illustrated in Figure 2.11. It is apparent that transmission windup also occurs for this system to some extent. However, its 0.2um magnitude is

relatively small compared to the smallest increment 0.5um required for the alignment process in the z direction. Therefore, its effect will be neglected in trajectory planning and the investigation will focus on the transmission windup of the five-bar.

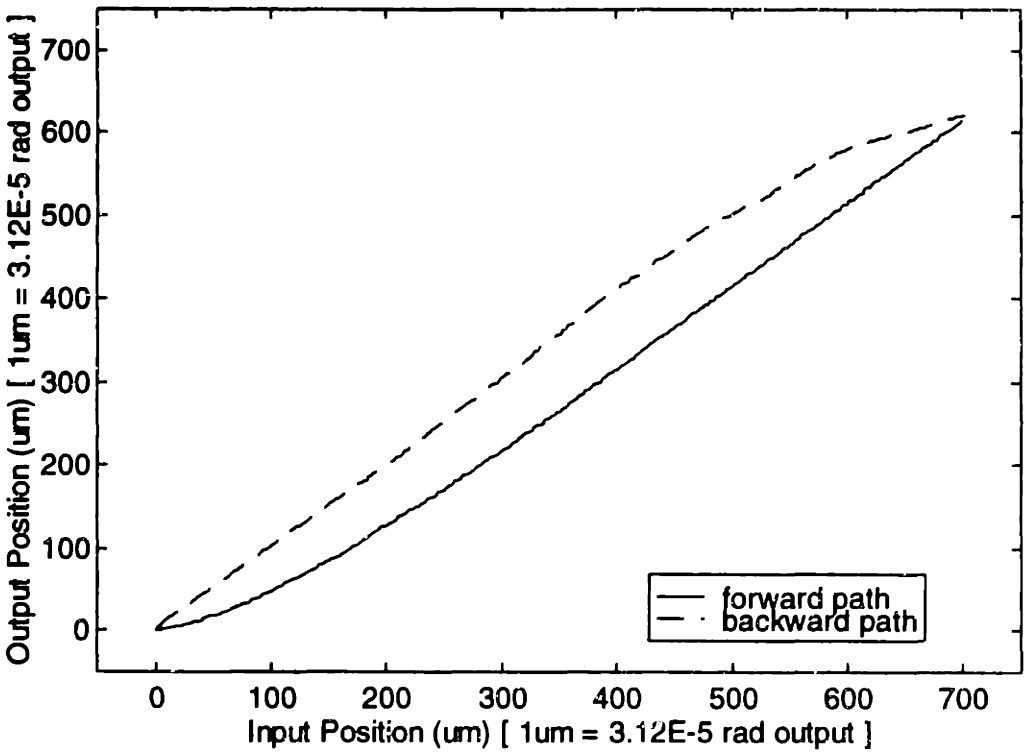

Figure 2.8 Illustration of Five-bar Transmission Windup

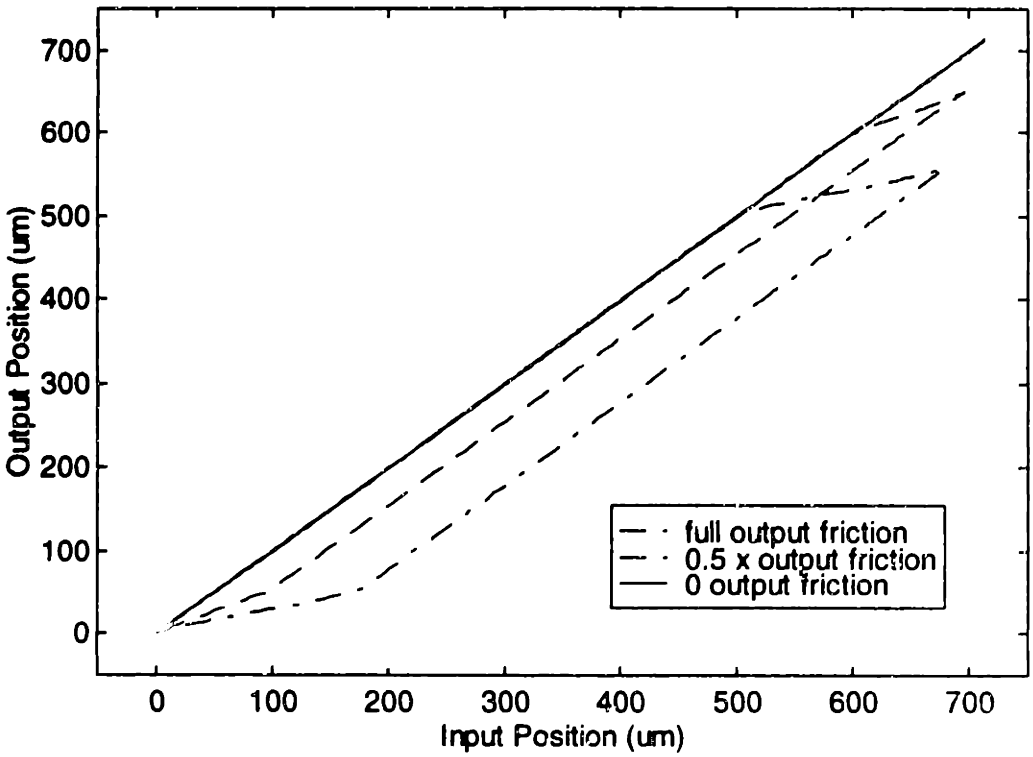

Figure 2.9 Numerical Simulation of Transmission Windup

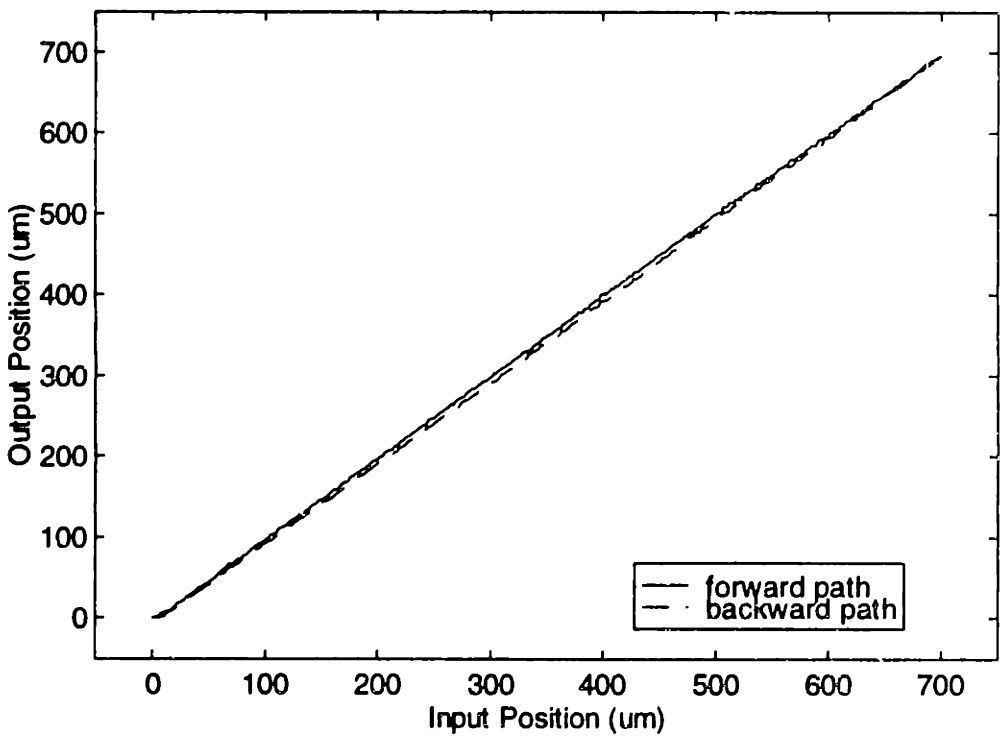

Figure 2.10 Five-bar Response without Frictional Loading

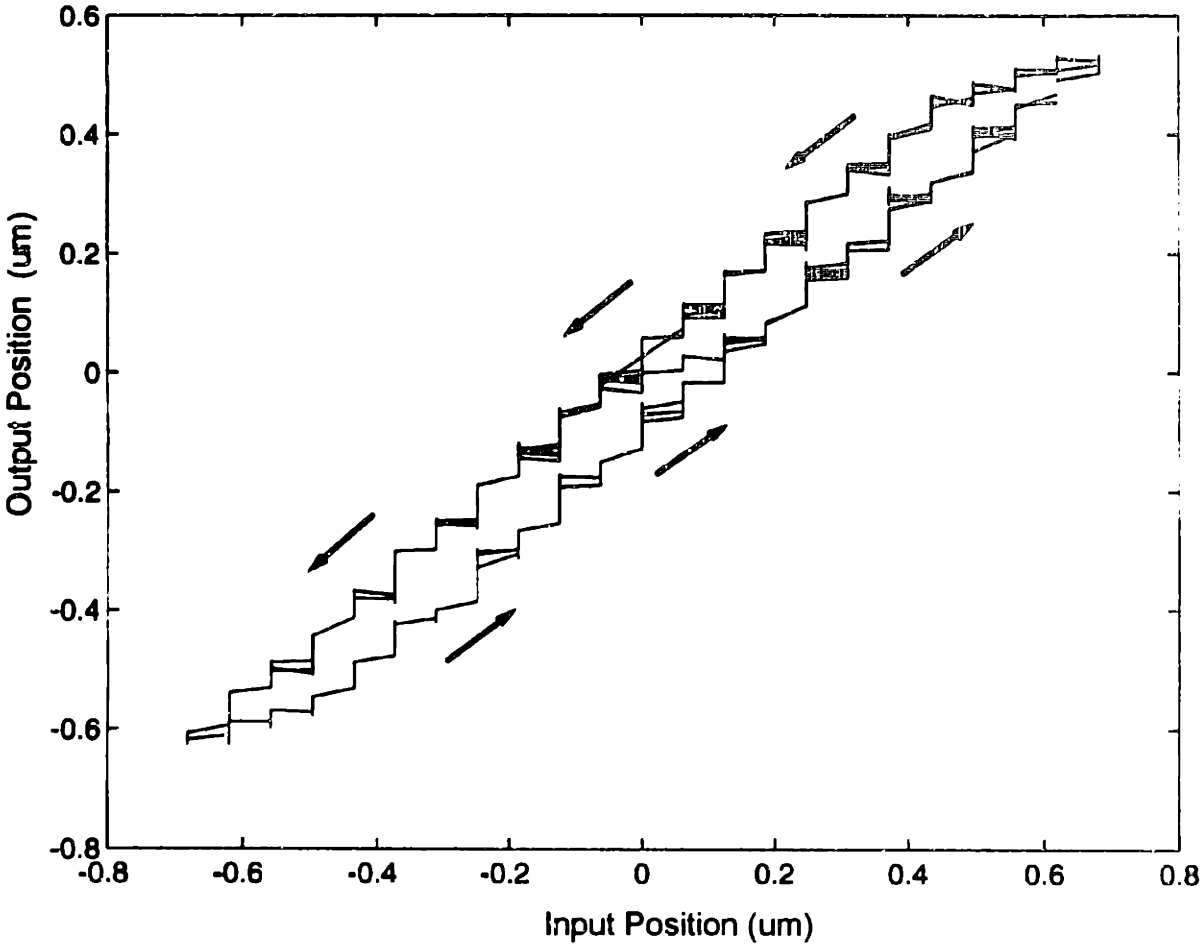

Figure 2.11 Illustration of Z-stage Transmission Windup

2.4.2 Effect of Preloading

In an effort to reduce the amount of backlash the output of the gear train was preloaded using a spring connected between the five-bar base link and the frame. This essentially adds a constant biased torque on the output inertia since the force produced by the spring is approximately constant over the range of motions encountered. Preloading is a common method of reducing conventional backlash in gears, but it was not obvious what effect this would have on the imperfect type of backlash encountered. The results of simulations for three different preloads are shown in Figure 2.12. It is

evident that the transmission windup decreases with increasing preload and that it is most effective when the preload is greater than the output coefficient of friction. As preloading increases the torque on the nonlinear spring increases which increases the effective stiffness of the gears. This reduces the amount of windup required to make the output inertia slide.

Experiments confirm the positive effect of preloading. The results are shown in Figure 2.13. It can be seen that a preload greater than the output coefficient of friction effectively reduces windup by a factor of two. It was also found that increasing the preload much beyond this has little effect. This appears to be the result of finite stiffness of the harmonic drive gears which was confirmed by the manufactures performance specifications and is a consequence of the inherently flexible nature of the harmonic drive gear design.

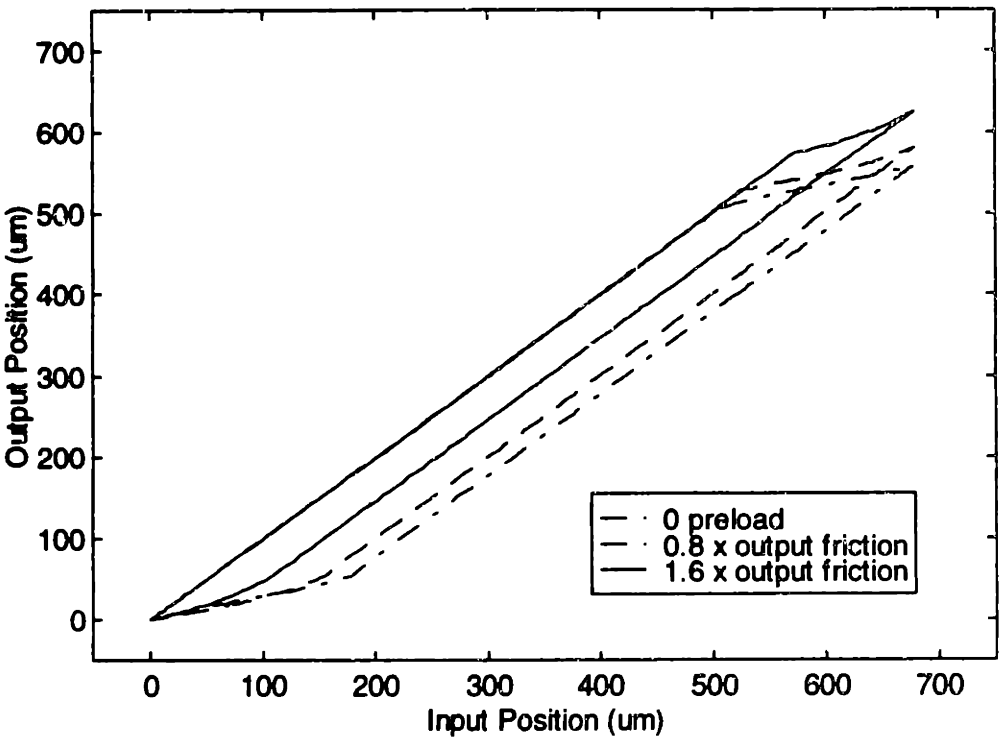

Figure 2.12 Numerical Simulation of Preloading Effect

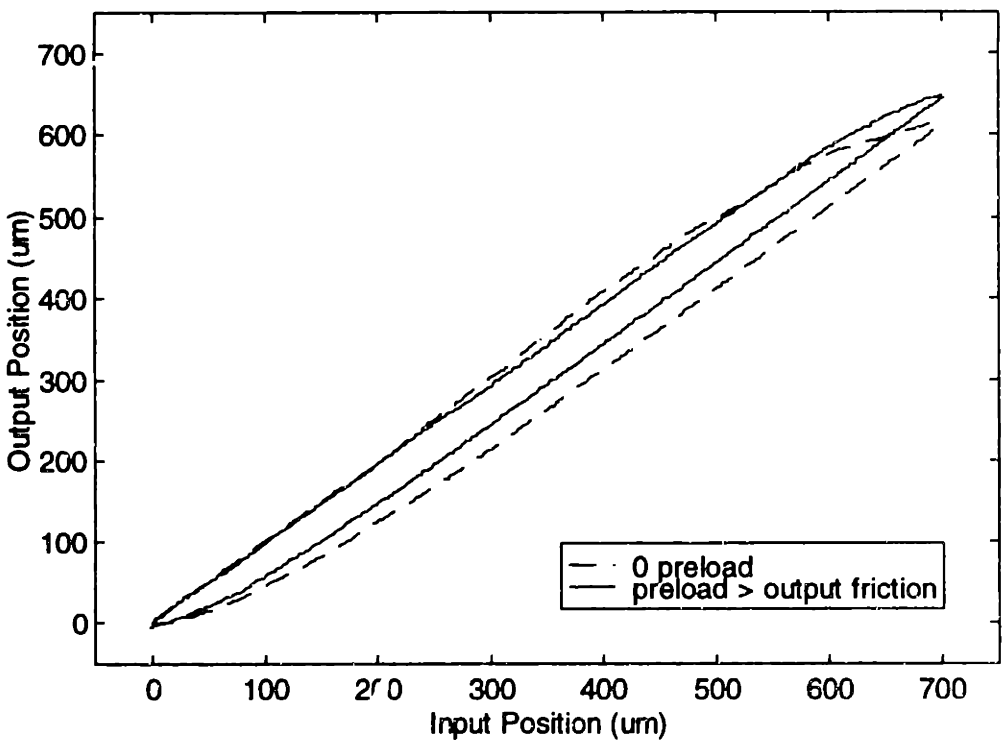

Figure 2.13 The Effect of Preloading

2.4.3 Estimation of Windup

An alternative approach to reduce the effects of transmission windup is to estimate its value based on previous input encoder values and use this estimate to directly compensate. This method could be combined with preloading to further enhance performance. The transmission windup W is defined as the difference between the input and the output of the gear train:

$$W = q_i - q_l \qquad (2.18)$$

$$q_i = rq_m$$

where q_l is the load inertia position, and q_i is the input position which is equal to the product of the reduction ratio r and the motor inertia position q_m. A plot of transmission windup versus load position for the five-bar is illustrated in Figure 2.14. It is apparent that the transmission windup has a maximum magnitude before a direction reversal. It then unwinds and winds up in the opposite direction. The shape of the curve produced was found to be consistent for large scan ranges. This implies that the transmission windup is a function of the position displacement from a direction reversal. The expression for this relationship is:

$$W = W(q_l - q_{lr}) \qquad (2.19)$$

where q_{lr} is the load position of the last direction reversal. This behavior was also observed with preloading of the system. A simple empirical relationship was adopted to approximate the transmission windup function.

This approach simplifies compensation and identification of the function. The form of the approximation is:

$$W(q_1 - q_{1t}) = W_{max}\, sgn(q_1 - q_{1t})\left[1 - 2\exp\left(-\frac{4|q_1 - q_{1t}|}{Q}\right)\right] \qquad (2.20)$$

The parameters of the function are easily identified as the maximum magnitude of the transmission windup W_{max} and the displacement Q required to completely wind the transmission in the opposite direction.

A comparison between the transmission windup estimation function and the actual response appears in Figure 2.15. It is evident that the function is a good approximation to the actual response and is always within 10um of the data. Furthermore, it was found that the approximation was highly robust to variations of the fitting parameters. It should be noted that this method of estimation assumes that the transmission windup function is not rate or acceleration dependent. This is a good approximation because the output inertial force is small compared to the spring and friction forces in the system. Experimental evidence also supports this assumption.

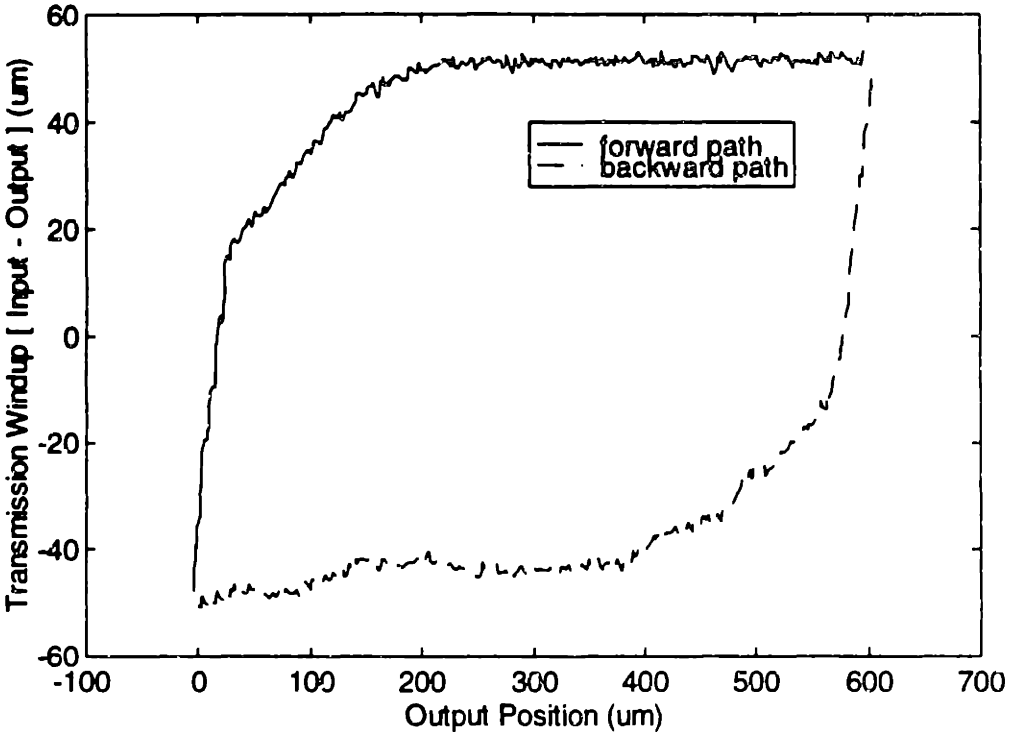

Figure 2.14 Transmission Windup vs. Load Position

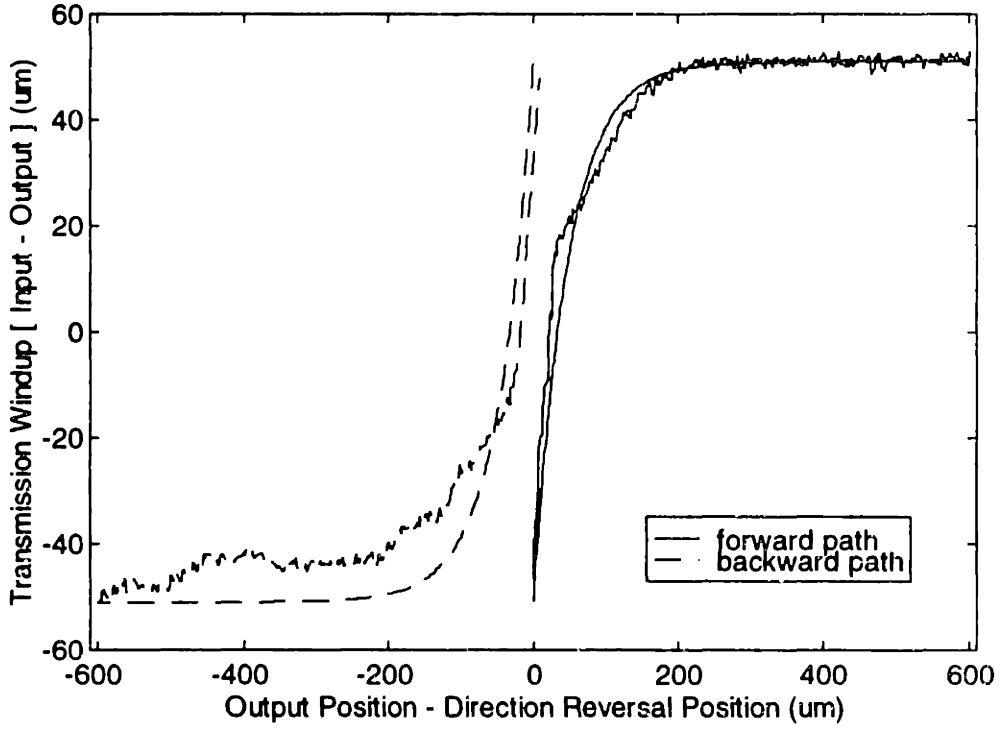

Figure 2.15 Transmission Windup Estimation Function

2.4.4 Windup Compensation

With an accurate estimate of the transmission windup available it is now possible to directly compensate by calculating the required input position from the desired output position and the transmission windup estimate. Combining equations (2.18) and (2.19) we have:

$$q_i = q_l + W(q_l - q_{li}) \tag{2.21}$$

Since we are interested in calculating the desired input trajectory the desired output trajectory will be used in place of the actual output position. Furthermore, to avoid the effects of servo errors and encoder noise the desired output trajectory is used to calculate the direction reversal position. The compensation scheme just described is:

$$q_{id} = q_{ld} + W(q_{ld} - q_{lrd}) \tag{2.22}$$

where q_{id} is the desired input, q_{ld} is the desired output, and q_{lrd} is the direction reversal output position calculated from the desired output trajectory. Intuitively this compensation scheme amounts to adding a variable offset to the required input after a direction reversal to linearize the output response.

For internal consistency of the trajectory generation functions the transmission windup must be subtracted from the position of the axis measured from the encoders. The equation for this is:

$$q_l = q_i - W(q_{ld} - q_{lrd}) \tag{2.23}$$

where q_l is the actual load inertia position and q_i is the input position measured from the motor shaft encoders.

Another issue that must be addressed is the possibility that the desired output position may reverse before the harmonic drives are completely wound. This is a important factor because the estimate of the transmission windup is based on the assumption that the transmission is completely wound up before a direction reversal. This assures that the transmission will be in a known state and the response of the output will be a known function of the distance from the reversal position. If this is not the case then some method of estimating the internal state of the transmission must be used and reflected in the transmission windup function. The current value of the transmission windup estimate is a measure of the internal state of the system. This information can be used to calculate an equivalent direction reversal position that reflects the estimate of the internal state. The equation for the equivalent reversal position is:

$$q_{lrd} = q_{lrd} - \delta q \tag{2.24}$$

where δq is an additional offset to account for the current value of transmission windup. This can be calculated by inverting the transmission windup function:

$$\delta q = W^{-1}(W, q_{ld} - q_{lrd}) \tag{2.25}$$

The current argument to the transmission windup function must also be included in the inverse because the windup function is not strictly invertable. This results in the relation:

$$\delta q = \mathrm{sgn}(q_{id} - q_{lid})\frac{Q}{4}\ln\left[\frac{1}{2}\left(\frac{W}{W_{max}}\mathrm{sgn}(q_{id} - q_{lid}) + 1\right)\right] \qquad (2.26)$$

Figure 2.16 graphically illustrates this method. After a direction reversal an equivalent direction reversal point based on δq is calculated. This essentially allows the transmission windup estimate to jump from the current curve to the opposite direction curve while preserving continuity. It is apparent that if the transmission is fully wound $\delta q = 0$ and the equivalent reversal position reduces to the reversal position.

It should be noted that the transmission compensation method developed in this section represents a feed forward open loop compensation scheme and consequently may be sensitive to disturbances and parameter variations. Therefore the performance should be carefully verified through experimentation.

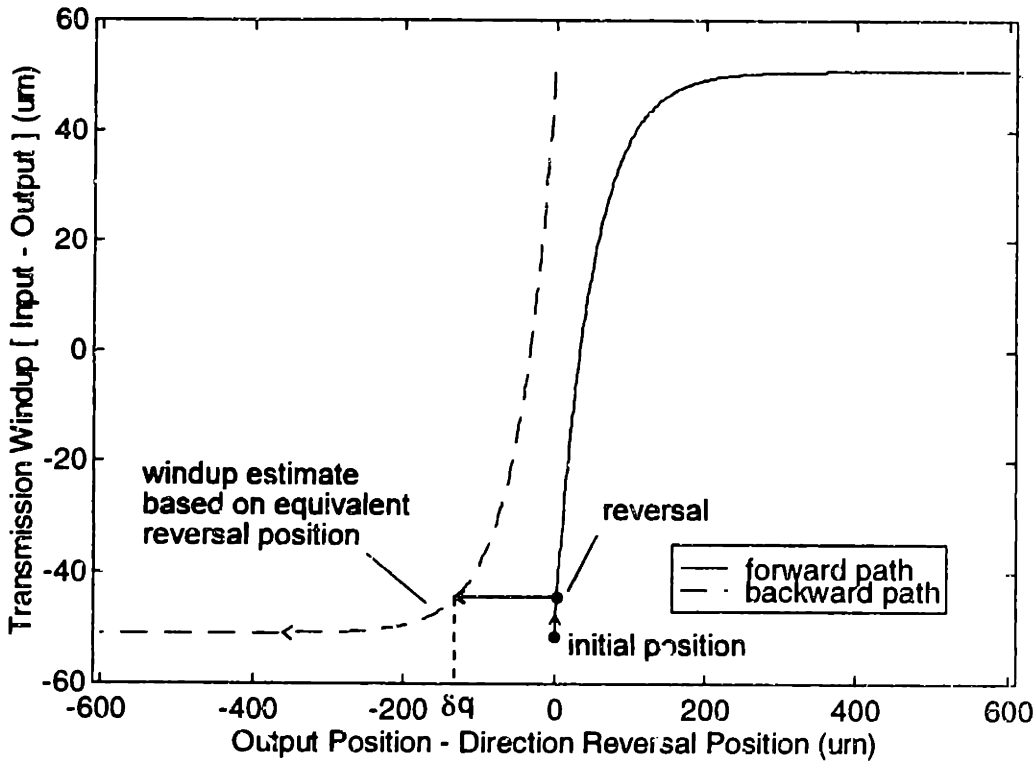

Figure 2.16 Estimation of Equivalent Reversal Position

2.4.5 Performance

The performance of the windup compensation method was experimentally investigated over a broad range of operating conditions in order to verify the robustness of the control scheme. The first test consisted of scanning a forward and backward trajectory over a large range ensuring that the transmission is fully wound before a direction reversal. This is the most ideal situation and the controller should perform best under these circumstances. The result is in Figure 2.17. It can be seen that a substantial improvement has been made. Note that the x-axis now becomes the desired output position. The difference between the forward and backward trajectories shows that the backlash has been reduced to 15um. This is a factor of 7 times better than the uncompensated performance. The same test

was also performed with preloading. The results in Figure 2.18 unexpectedly show little improvement over no preloading. To test the validity of the equivalent direction reversal position concept a test over a small range was performed where the transmission would not have a chance to fully windup before direction reversal. The results in Figure 2.19 show that the performance does not degrade over small ranges. Further, a test for several successive direction reversals for the same range was performed to demonstrate the repeatability and stability of the method. It is apparent from Figure 2.20 that the performance does remain consistent over successive direction reversals.

The response of both five-bar links performing coordinated motion was also investigated. The endpoint of the manipulator was commanded to move in a square trajectory and the output of the links was measured using two capacitance sensors. The position of the links was fed through the forward kinematics to calculate the endpoint position. The uncompensated motion for a 300um square trajectory is illustrated in Figure 2.21. It can be seen that the shape of the response is substantially deformed and that the position is off by as much as 120um corresponding to 40% of the range of motion. The response with windup compensation is shown in Figure 2.22. It can be seen that a substantial improvement is made. The shape of the trajectory is far more regular and the maximum error is 30um. The factor of 4 improvement, however, is somewhat less than expected. This is probably the result of frictional coupling between the two links which was not modeled in the windup estimate. It should be noted that this coupling affects the output dynamics only and the assumption that the motor actuator dynamics are uncoupled remains valid due to the large gear reductions. To help reduce coupling effects preloading of the links was attempted. The response illustrated in Figure 2.23 shows a substantial improvement over windup compensation alone. The maximum error observed was less than 15um. Thus windup compensation combined with preloading improves coordinated

motion performance by a factor of 8 which is approximately the same performance improvement observed for single axis motion.

From the tests performed it is evident that transmission windup compensation makes a dramatic factor of 8 improvement over the uncompensated response. The broad range of tests performed indicate that the estimate of the internal state using the equivalent direction reversal position is valid. Preloading showed no significant improvement over windup compensation alone for single axis motion. However, it significantly decreased the effects of frictional coupling between the five-bar links.

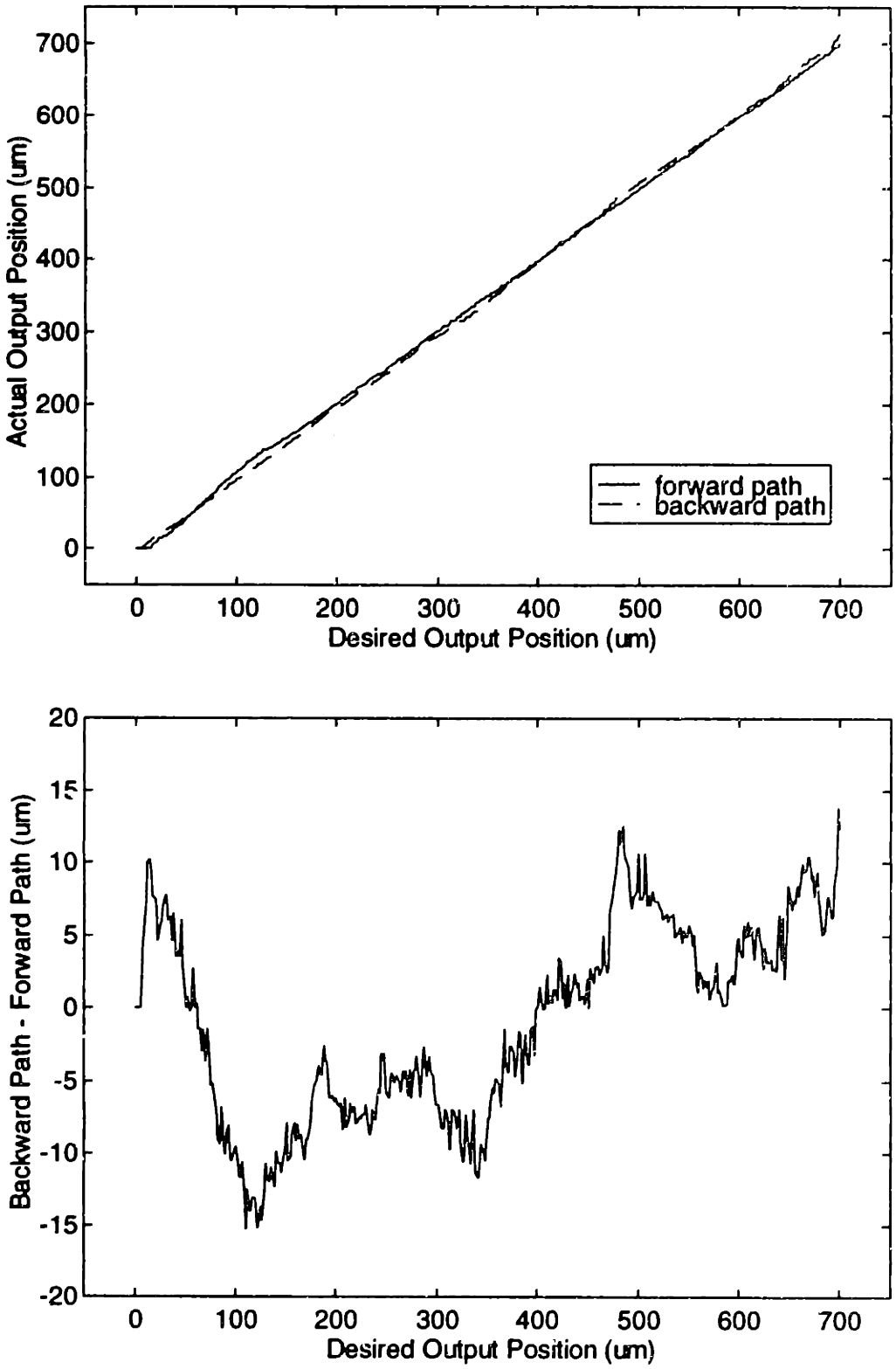

Figure 2.17 Windup Compensation over 700um Range

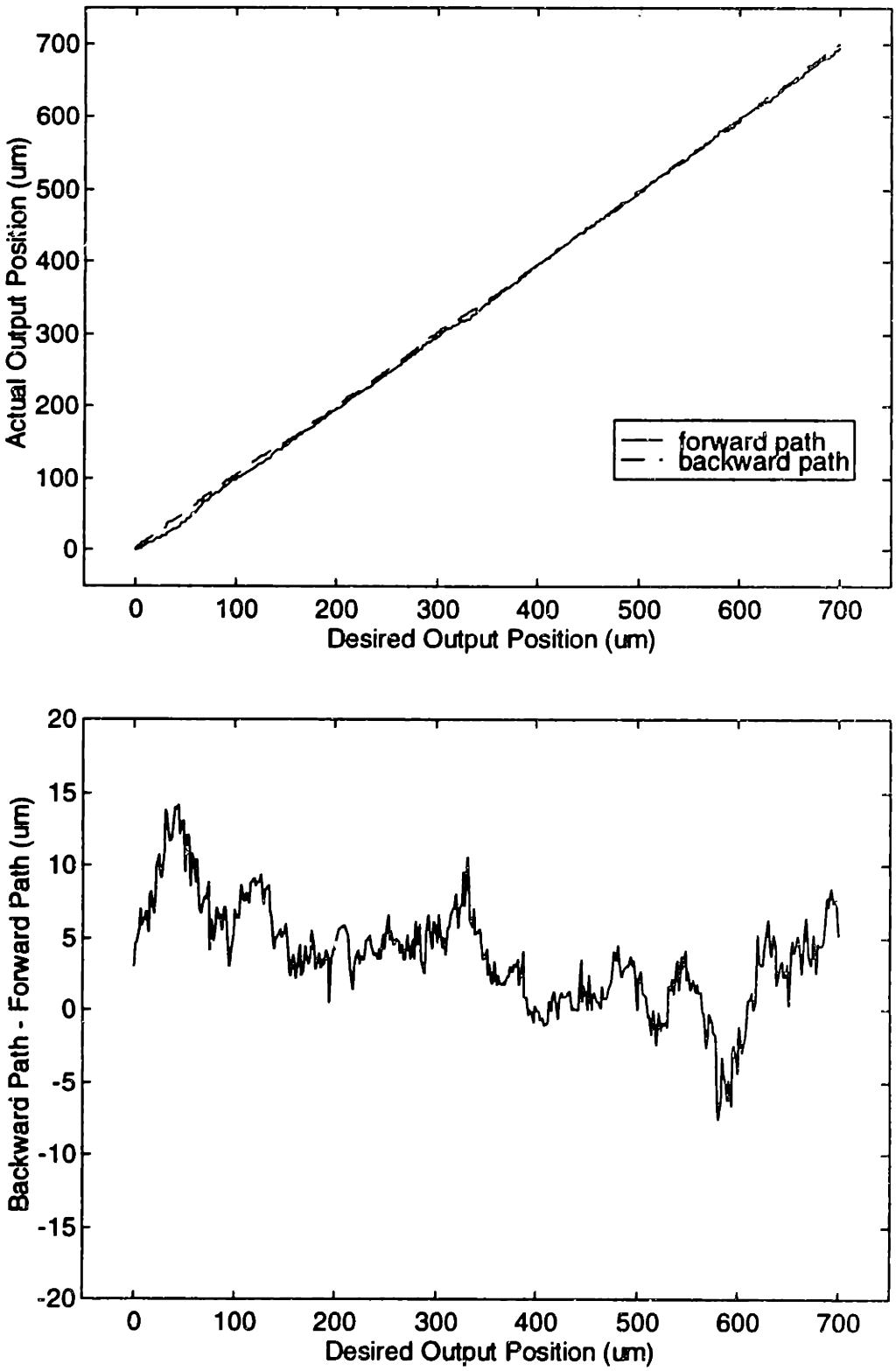

Figure 2.18 Windup Compensation with Preloading

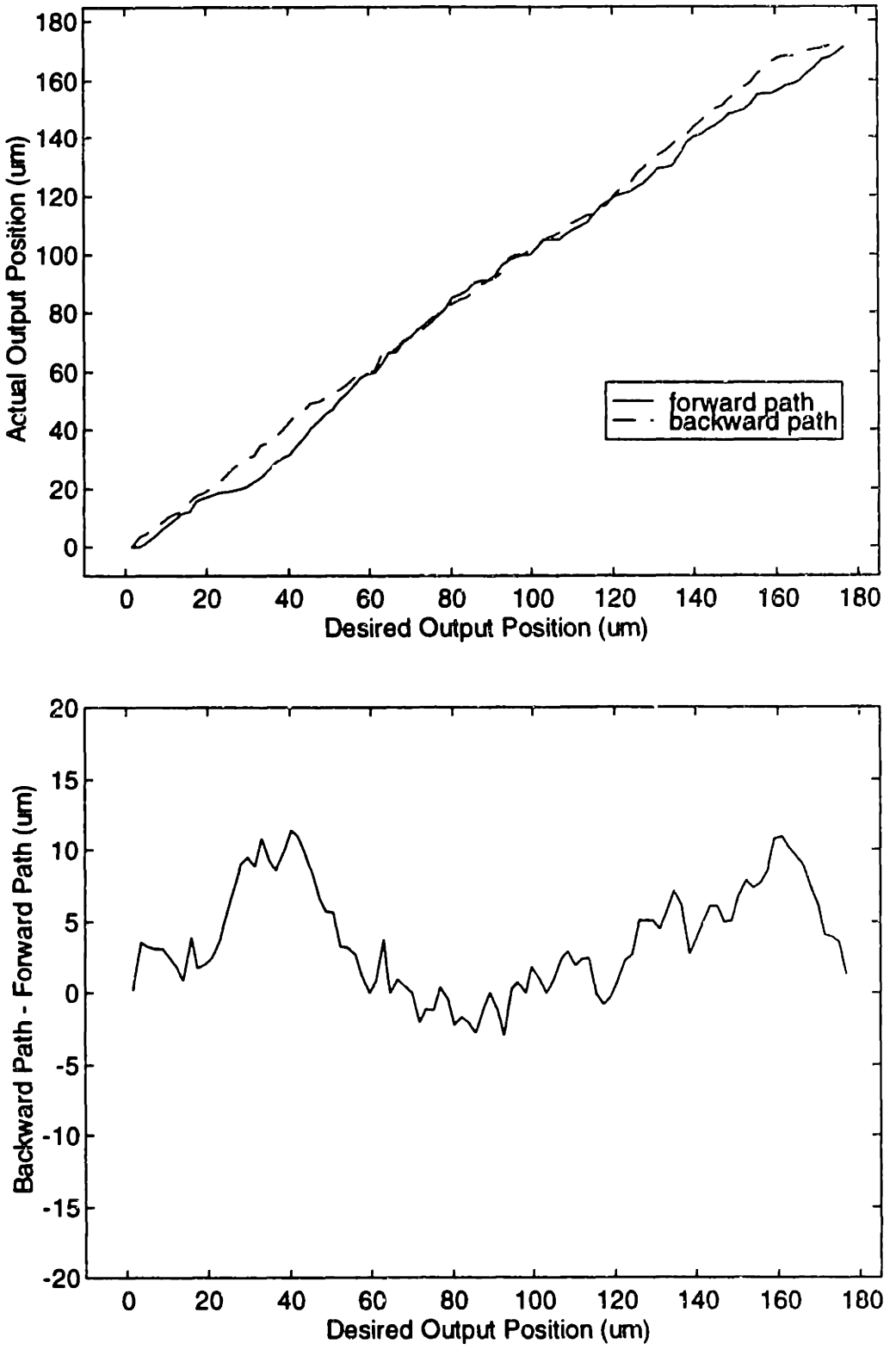

Figure 2.19 Windup Compensation over 175um Range

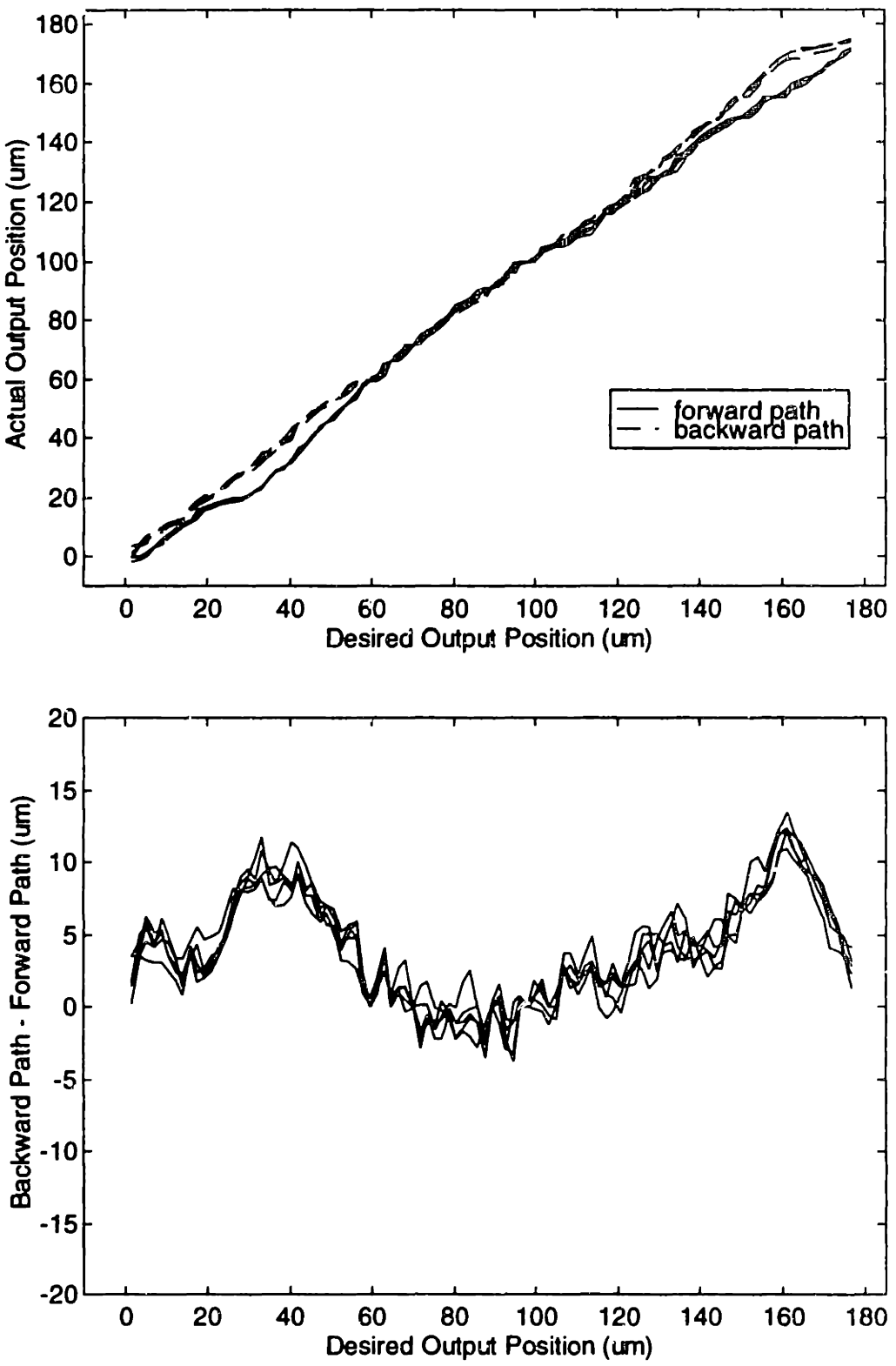

Figure 2.20 Repeated Scanning over 175um Range

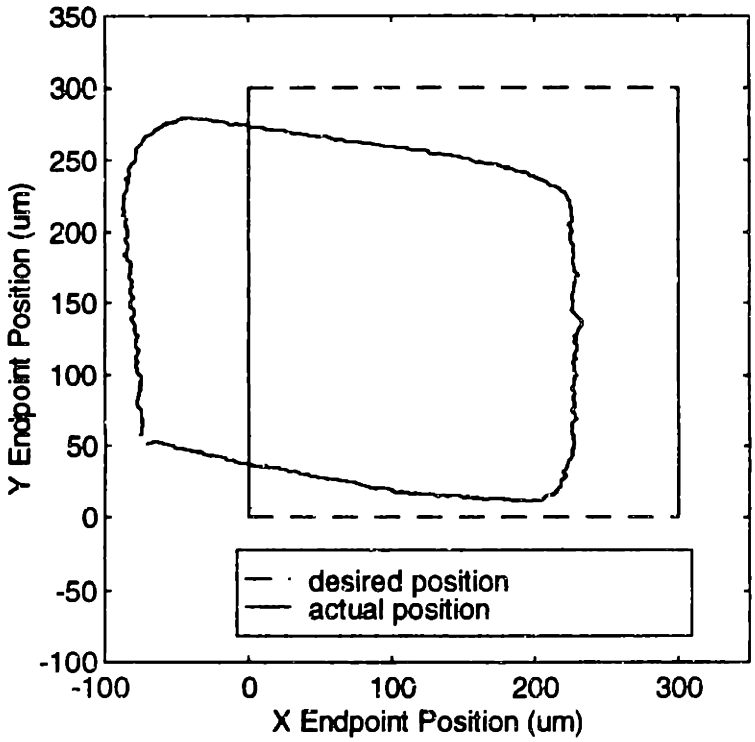

Figure 2.21 Square Trajectory without Windup Compensation

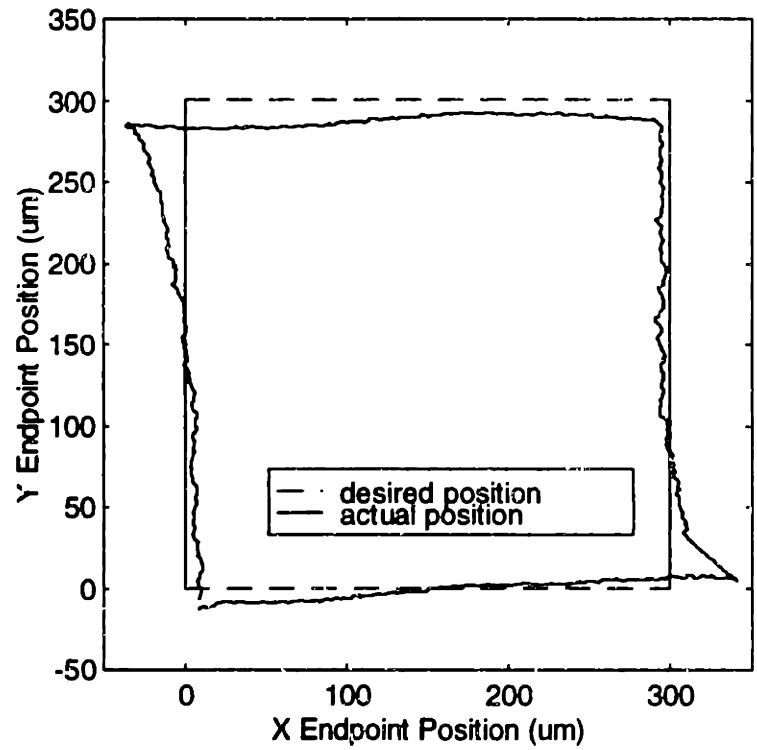

Figure 2.22 Square Trajectory with Windup Compensation

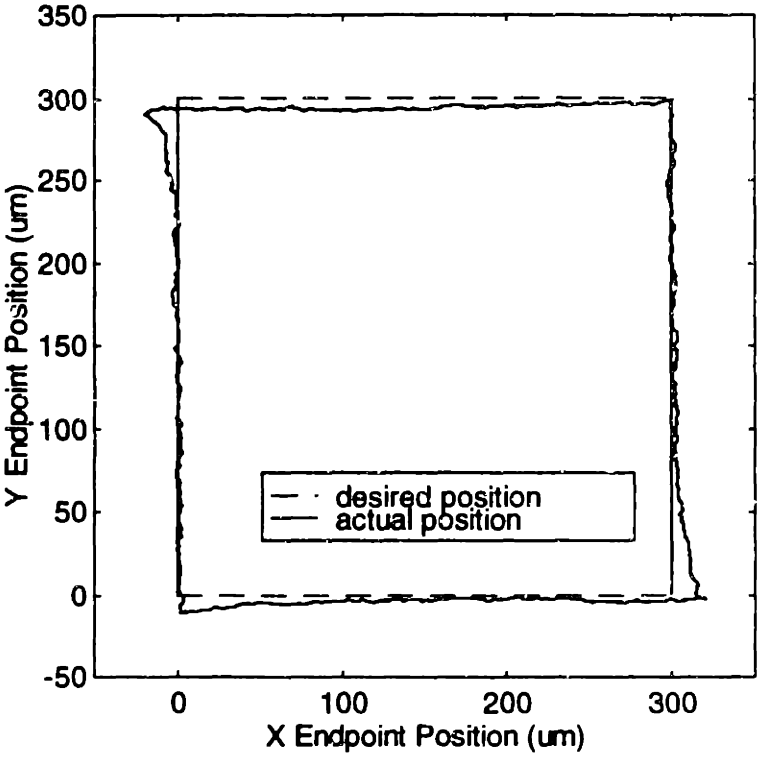

Figure 2.23 Square Trajectory with Preloading and Windup Compensation

2.5 Resolution Characterization

One of the most critical performance characteristics of the macro manipulator is the ability to consistently move small motion increments. This characteristic known as resolution is defined as the smallest step the machine can consistently make during point to point motion. A machine's resolution effectively puts an upper limit on the repeatability and accuracy that can be achieved even with closed loop feedback. For the alignment process a resolution of 0.5um is required for the z-stage to maximize light throughput. A resolution of less than 5um is required for the five-bar so that it can scan a grid sufficiently dense to initiate light coupling. The resolution of a machine must be determined experimentally since it often depends on subtle machine dynamics factors that are difficult to model such gear meshing, bearing noise, and transmission stiffness. Statistical measures should also be used since the factors that influence resolution can vary over time and the range of the mechanism. With these issues in mind a resolution test was devised for the z-stage and five-bar. The test consists of 1000 steps in one direction from which a histogram of the resultant displacements are made. The displacements are determined using high accuracy sensors that measure the output of the mechanism. The initial step size used is one motor encoder count. If this size produces inconsistent increments the magnitude of the step is increased by one encoder count and the test is run again. This process is repeated until consistent motion is observed. The maximum value of the consistent increments is the resolution of the mechanism.

The results for the z-stage for increments of one encoder count are shown in Figure 2.24. The output was measured using a high accuracy interpolation encoder. The first plot shows the histogram of motion increments. It can be seen that a bimodal distribution is produced with the z-stage making increments of roughly two encoder counts (0.125um) half of

the time and the other half the stage doesn't move. The z-stage position as a function of time for several steps shows what is happening. It appears that two encoder counts in sequence are required to make the stage move forward. This is probably the result of a minimum amount of transmission windup required to overcome static friction. Since consistent incremental motion was not observed a second test with step size equal to two encoder counts was performed. The results are in Figure 2.25. It is apparent from the histogram that consistent motion of two encoder counts is possible. The vast majority of increments are less than 0.14um. Therefore the resolution of the z-stage is 0.14um. This is more than 3.5 times the required specification. The time history of the z-stage confirms consistent increments of two encoder counts.

The results of the resolution test for the five-bar with increments of one encoder count (approximately 1.75um) appear in Figure 2.26. The output for the five-bar was measured using capacitance sensors mounted parallel to the five-bar links. It is evident from the histogram that consistent motion of one encoder count is possible. It should be noted that due to the non-Cartesian nature of the five-bar kinematics one encoder tic can represent between 1um to 2um depending on the position in the workspace. However, for most of the workspace one encoder count is less than 1.75um. The maximum motion that occurs is two encoder counts (3.5um). Therefore the resolution of the five-bar is 3.5um. This is more than 1.4 times the required value.

From the resolution tests performed it is evident that the resolution capability of the macro manipulator is well within the performance specifications.

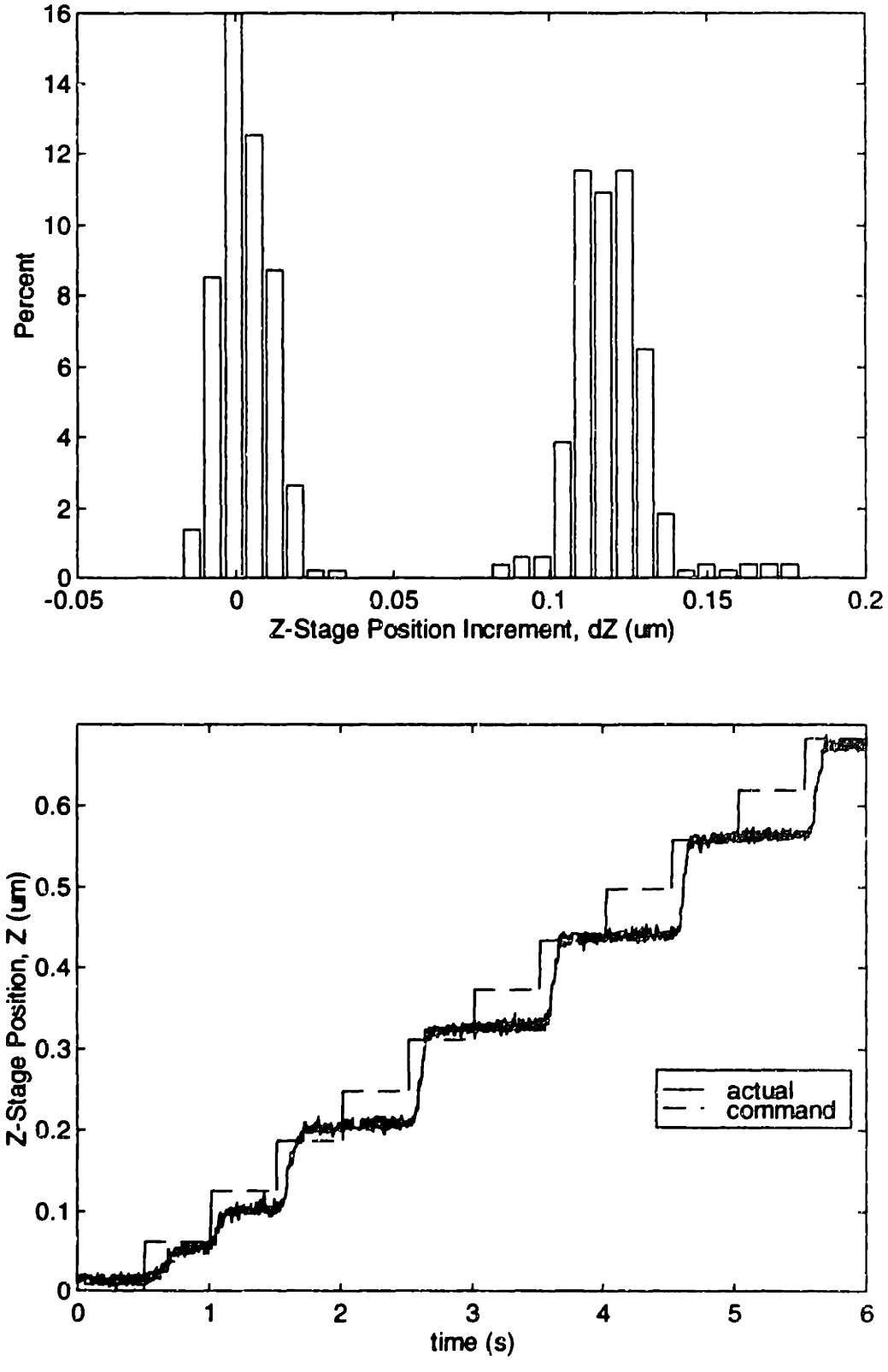

Figure 2.24 Resolution of Z-stage for One Encoder Count (0.062um) Steps

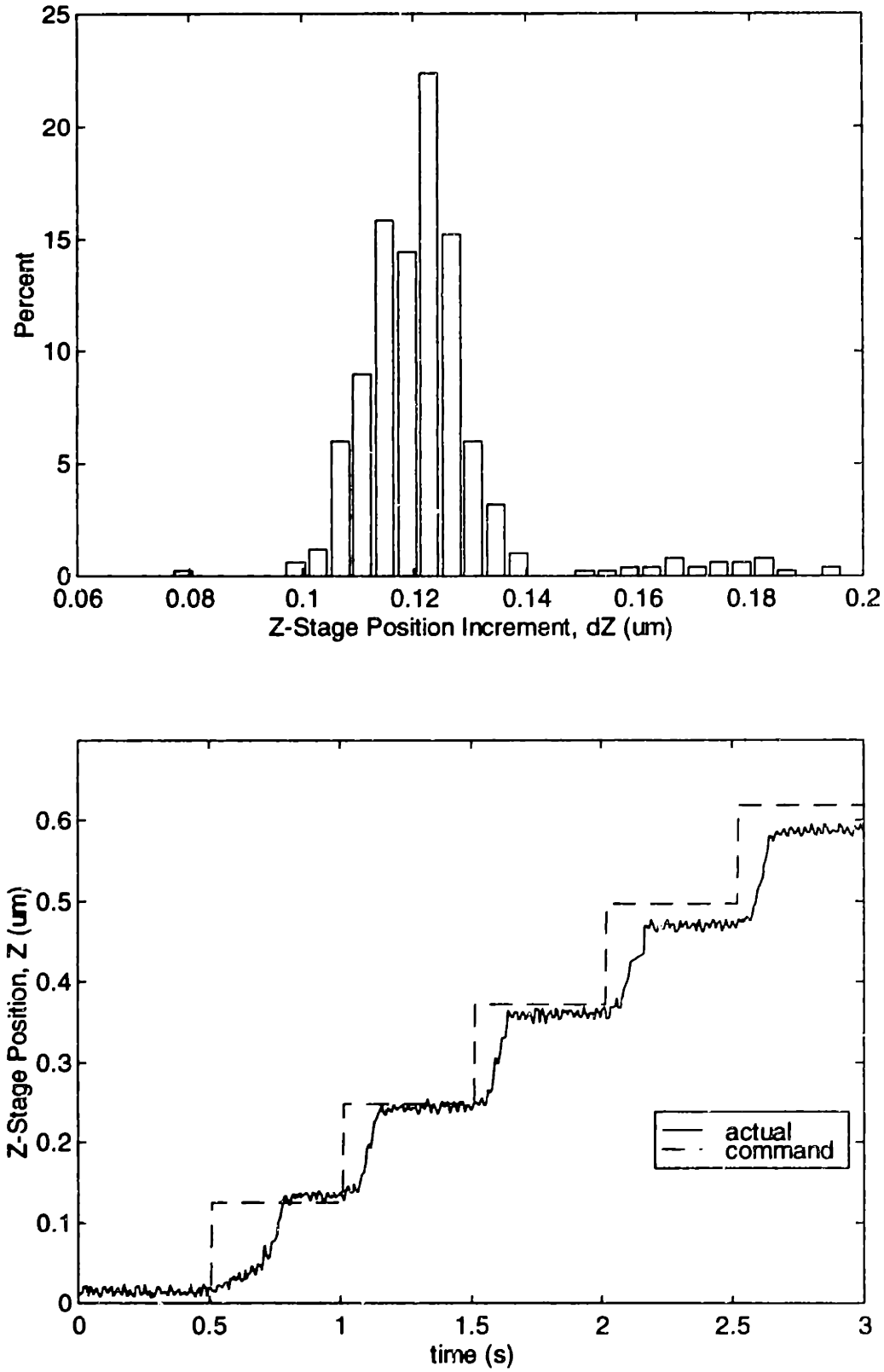

Figure 2.25 Resolution of Z-stage for Two Encoder Count (0.125um) Steps

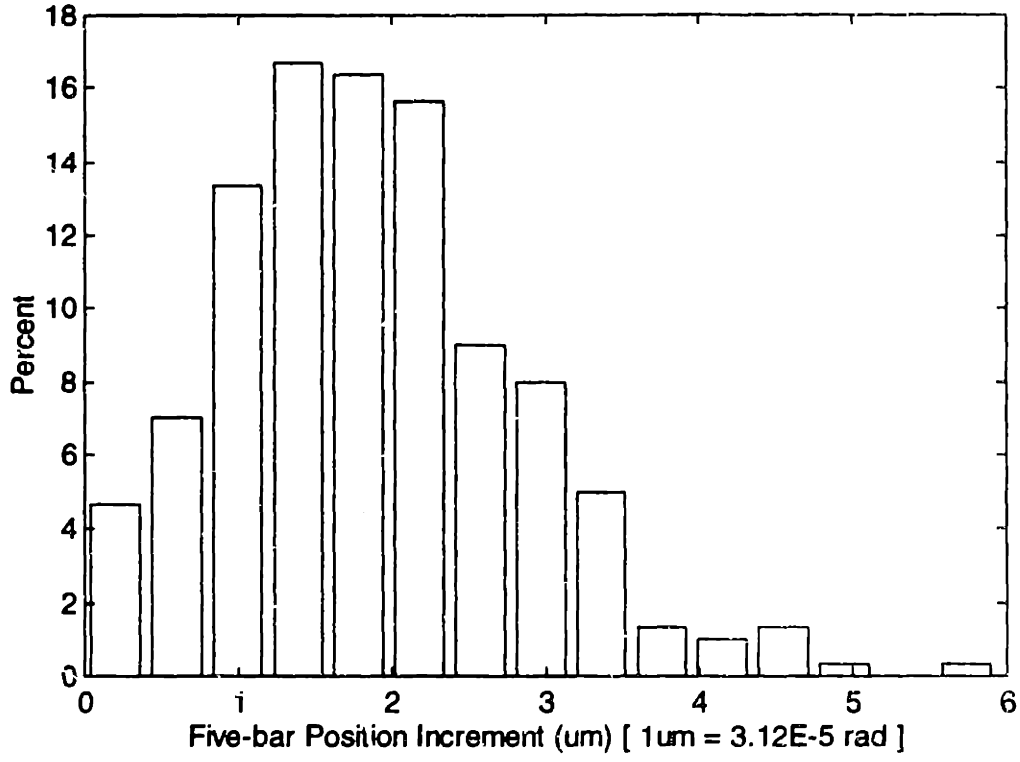

Figure 2.26 Resolution of Five-bar for One Encoder Count (1.75um) Steps

3. Path Planning for the AFPM

3.1 Introduction

In this chapter path planning algorithms are developed for the pigtailing alignment process. Figure 3.1 shows a schematic of the workspace. The optoelectronic device contains one input and two output locations. Three 5um core diameter polarization maintaining fibers are attached to these locations through movement in the x, y, and z directions using the two macro/micro manipulators. The x direction is at an angle to the z axis to account for refractive effects. In order to reduce coupling losses to acceptable levels (11 %) the fibers must be aligned with an accuracy of 2um in the z direction and 0.1um in the x and y directions. This includes uncertainties in the angular alignment of the fibers achieved through fixturing.

To guide the alignment two forms of sensing are available. A vision system mounted above the device can locate the z position of the fibers and chip to within 2um and the x position of the fibers with respect to the chip to within 50um. Light throughput feedback is also available when both an input and output fiber are within 5um of the optimal locations in the x-y plane. The source of the light is a laser coupled to the input fiber. The light throughput through the device is measured using photodiode sensors connected to the end of the output fibers. Approximately equal amounts of light pass through the outputs of the chip when light enters the input. Figure 3.2 shows the light intensity profile obtained by scanning the input location with the micro manipulator with one of the outputs coupled. It is apparent that the profile is a smooth Gaussian like function that can be maximized to achieve x-y alignment. The same profile also occurs at both outputs when the input is coupled. In addition to the two sensors available it

is known that the device location in the y direction is fixtured with an uncertainty of 100um.

The fibers are moved using specially designed fiber holders located at the endpoints of the macro/micro manipulators. The input is moved with one manipulator and the outputs are moved with the other. The macro manipulator was previously shown to have a range of 25mm and a resolution of 3.5um in the x, y directions and 0.14um in the z direction. The performance of the micro manipulator is investigated in [13] from which it was determined that the micro had a range of 70um and a resolution of 5nm in the x-y plane. Combined, the macro/micro manipulator has a range of 25mm and a resolution of 0.14um in the z direction and 5nm in the x-y plane. This is well within the required performance for the alignment. Paths for the macro manipulator are implemented as trapezoidal velocity profile functions in Cartesian space with the corresponding joint coordinates computed on-line using the inverse kinematics relations. The micro is controlled by supplying analog output commands to the piezoelectric actuator amplifiers which produce a displacement approximately proportional to the command voltage. An analog to digital converter is used to read the light intensity measured with the photodiodes.

The difficulty of the alignment process is largely due to the uncertainties associated with the vision information in the x direction and fixturing in the y direction. With an initial uncertainty of 50um in the x direction and 100um in the y direction for the input and output fibers both must be brought to within 5um of the optimal locations to initiate the light coupling required for light throughput feedback. This entails blindly searching both sides of the chip together through a four dimensional search space (Xin,Yin,Xout,Yout) with a fine 5um mesh. The main tasks required for alignment can be broken down into two steps. The first is the initiation of light coupling by suitably coordinating the motion of the input and output fibers. Maximization of the light throughput is then performed to move the

fibers to the optimal locations. Both of these operations must be performed in a minimum amount of time.

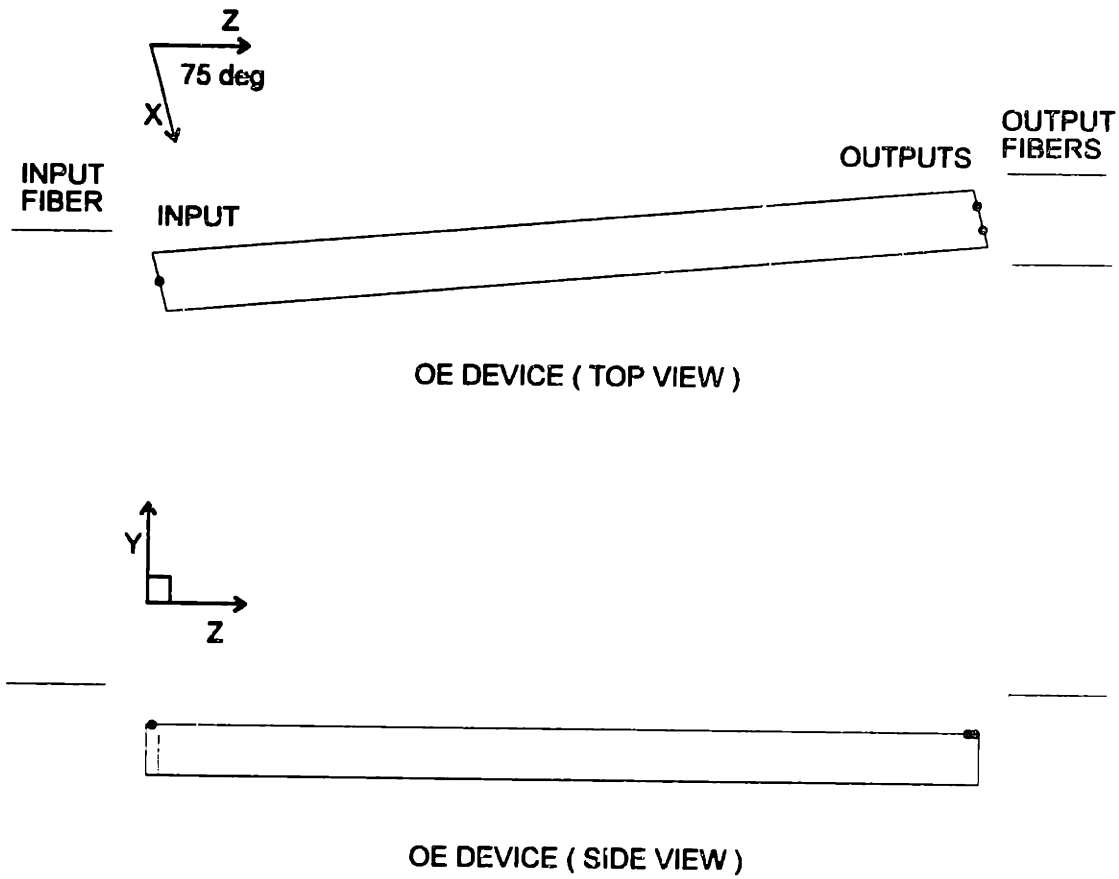

Figure 3.1 Schematic of the Workspace

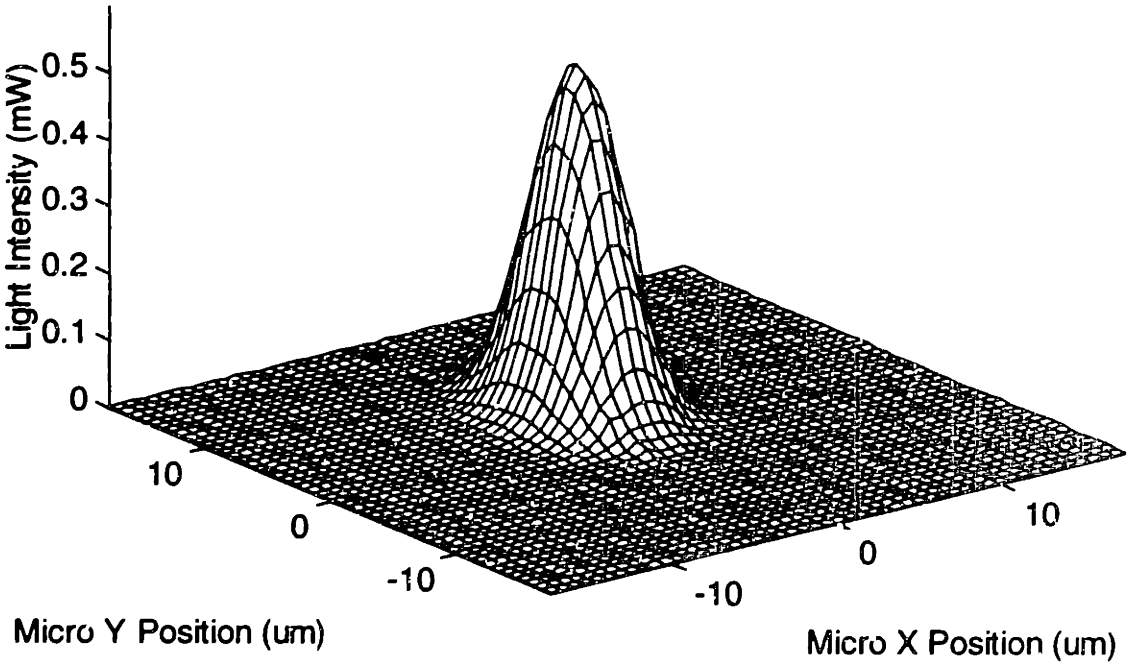

Figure 3.2 Light Intensity Distribution around Optimal Alignment Position

3.2 Light Coupling Initialization

The main objective of the light coupling initialization process is to move an input and output fiber to within 5um of the optimal locations so that some amount of light passes through the device allowing light throughput feedback. Outside of the 5um radii negligible light coupling exists since the fiber diameters are so small (5um) relative to the device size (~1000 um). The light profiles actually increase in radius as the z distance increases. It was originally thought that this could be used to reduce the alignment tolerances. However, in practice it was found the light intensity decreases extremely rapidly since the loss is the product of both the input and the output losses and the associated light coupling levels quickly became below noise thresholds. For this reason the z distance between the fibers and the chip had to be within 50um. It was also found that the tolerances are higher

for coupling two fibers at once compared to single fiber coupling because the loses are the product of the input and the output and as a result the light levels drop much faster from the peak values and below noise thresholds. Furthermore, for single fiber coupling it is possible to move backward in z to decrease alignment tolerances.

The light coupling process starts with the input and one output fiber placed within 50um the optimal locations in the x direction and 100um in the y direction. The z distance is at 50um to within 2um. This requires a blind search of both sides of the chip together over an area with x and y dimensions of 100um and 200um with a mesh size of 5um. Fundamentally, this is a four dimensional search space that must be covered as rapidly as possible. In the path planning the motion of macro manipulator is limited by a bandwidth of 10Hz and the micro manipulator is limited by a bandwidth of approximately 100Hz. The sampling rate of the photodiodes also limits the speed at which the manipulator can move. If it moves too fast the spacing of the sampled points will be greater than 5um. The photodiode sampling rate is 500 Hz. Thus the maximum speed that can be moved is:

$$v = \frac{5um}{1/500s^{-1}} = 2500um/s \tag{3.1}$$

The bandwidth of the photodiode similarly limits the maximum speed, but at 1000Hz it is not a factor. Thus, for a sinusoidal trajectory over a 100um range the scanning frequency is limited to:

$$\begin{aligned} v &= 2\pi fA \\ f &= \frac{v}{2\pi A} = \frac{2500um/s}{2\pi(50um)} = 8Hz \end{aligned} \tag{3.2}$$

This implies that the scanning frequency should be limited to 8Hz over the search area.

3.2.1 Proposed Methods

With the light coupling objectives determined three different approaches were proposed. These methods are illustrated in Figure 3.3. Method #1 is the most obvious approach in which the macro manipulator scans a Cartesian pattern of the input side for each point in a Cartesian grid of the output side. This is inherently a four dimensional search process and as a result the time required varies as the fourth power of the number of mesh points per axis. The result is that the time required explodes as the mesh density or size increases. Consequently, this method is not very robust to process variations. The time required to scan the search space is approximately:

$$t_s = \frac{XY^2}{f\Delta^3} = \frac{\pi T_p X^2 Y^2}{\Delta^4} \qquad (3.3)$$

where f is the scan frequency, X and Y are the scan dimensions, and Δ is the grid spacing. The equation can also be expressed in terms of the photodiode sampling period T_p. For a scan rate of 8 Hz with the required range and mesh spacing this method takes 67 minutes. Even with an unreliable grid spacing of 10um the process still takes 8.3 minutes. Obviously, this method is too slow and is not robust to uncertainties. Therefore it was not selected.

In order to decrease scanning time the use of the faster micro was investigated in Method #2. In this method the micro manipulators scan a Cartesian pattern in the Xin-Xout plane for each point on a grid in the Yin-Yout plane formed using the macro manipulators. This method exploits the much higher bandwidth of the micro manipulators combined with the larger range of the macro manipulators. The micro manipulator can actually scan diagonally across its workspace to achieve a range of 100um since its

coordinate frame is at a 45 degree angle to the x, y axes and it has a range of 70um. Fundamentally, this is still a four dimensional search algorithm and as a result it is not robust to uncertainties. However, the micro manipulators have the capability to scan at 100 Hz which helps offset this effect. The time required to scan the search space is approximately given by:

$$t_s = \frac{XY^2}{f\Delta^3} \tag{3.4}$$

At the increased scanning rate the space can be covered in 5.3 minutes. Since this four dimensional search needs to be done only once per device this amounts to 1.8 minutes per fiber which is within the required time period. However, to scan at 100 Hz over a 100um area it is necessary to increase the photodiode sampling rate by a factor of 12.5 to 6250 Hz which would require substantial control hardware changes.

It is evident from the previous calculations that the four dimensional nature of the search space places severe performance requirements on the system. Method #3 attempts to overcome this limitation by using a large area sensor at the output to guide the coupling of the input fiber. This essentially decouples the four dimensional search problem into two dimensional searches for each fiber. As a result the time required is greatly reduced and the robustness to uncertainty is dramatically increased since the search time varies as the power of two. A large diameter core multimode fiber connected to a photodiode sensor was used as the area sensor because it is compact, light, and inexpensive. This fiber sensor was mounted to the side of the fiber holder. With the multimode fiber roughly aligned to the output the input fiber can be coupled by performing a two dimensional cartesian scan of the input. After the input is aligned the outputs can be coupled by successive cartesian scans. The time required for the search is approximately:

$$t_s = \frac{Y}{f\Delta} = \frac{\pi T_p XY}{\Delta^2} \qquad (3.5)$$

For a scan rate of 8 Hz the time required is 5 seconds per fiber. This is a vast improvement over the two previous methods and requires less hardware modification than method two. For these reasons method #3 was selected as the light coupling initialization algorithm.

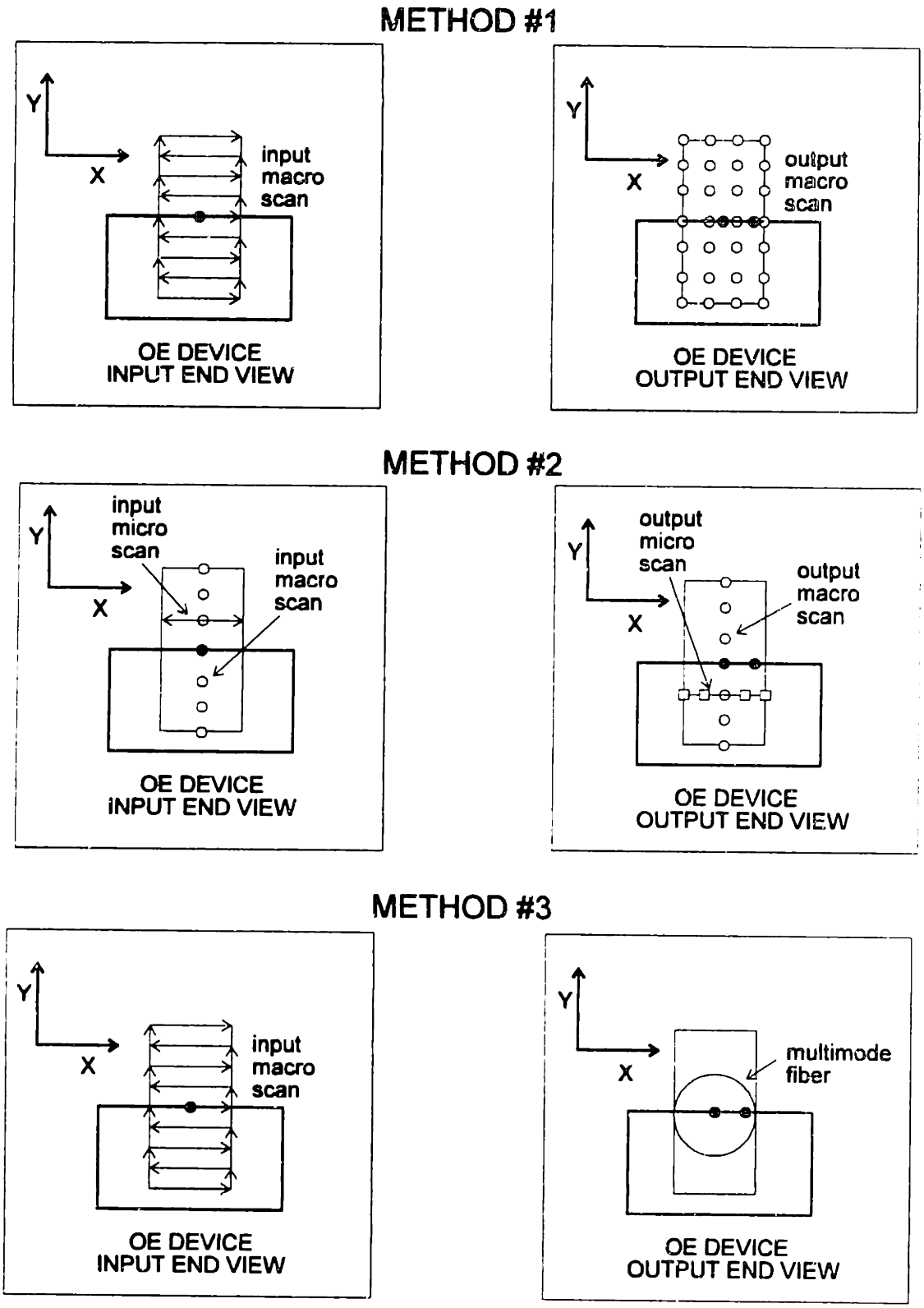

Figure 3.3 Proposed Light Coupling Initialization Methods

3.2.2 Multimode Fiber Approach

The multimode fiber light coupling initialization method begins with the coarse placement of the input fiber to within 100um of the input position in the x and y directions and 50um from the chip in the z direction. This can be achieved using the vision system and fixturing. At this point a sufficient amount of light travels through the device to allow alignment of the multimode fiber. The light from the input fiber scatters through the device and produces a light distribution of the form shown in Figure 3.4. The placement accuracy of the multimode fiber must be within the radius of the core to initiate coupling with the output. It is thus apparent that using a larger diameter core reduces the alignment tolerances. From testing different size fibers it was found that if the diameter is too large an excessive amount of light passes into the fiber from the device which interferes with the detection of the input alignment and can result in a false input detection. It is evident that there is a tradeoff between alignment tolerance and background interference effects. It was found that a core diameter of 100um provided the best compromise. This requires an alignment tolerance of 50um radius in the x-y plane and also 50um in the z direction.

The alignment in the x and z directions can be performed with the vision system. However, the fixturing tolerance of 100um in the y direction is insufficient for alignment. For this task the form of the device light distribution was used. It is apparent from the distribution that the light level drops to zero at the output position which occurs at the top of the device. The alignment in the y direction is accomplished by positioning the multimode fiber 200um below the top of the device after it is aligned in the x and z directions. The fiber is then moved upward until the light level drops below a predetermined threshold (10% of the maximum light level). At this point the multimode is within 50um of the output location in the y direction.

This method was found to be robust to light level variations and position errors. The time required was under 5s. After the multimode fiber is aligned with the output a cartesian scan of the input (100um in the x direction and 200um in the y with a grid density of 5um) is performed to initiate light coupling. The input light throughput can now be maximized to complete the input alignment. With the input fiber aligned light coupling initialization of the outputs can be performed by a Cartesian scan of the output locations. The time required to initiate light coupling was found to be mainly a function of the cartesian scan time which amounts to 6.7s per fiber.

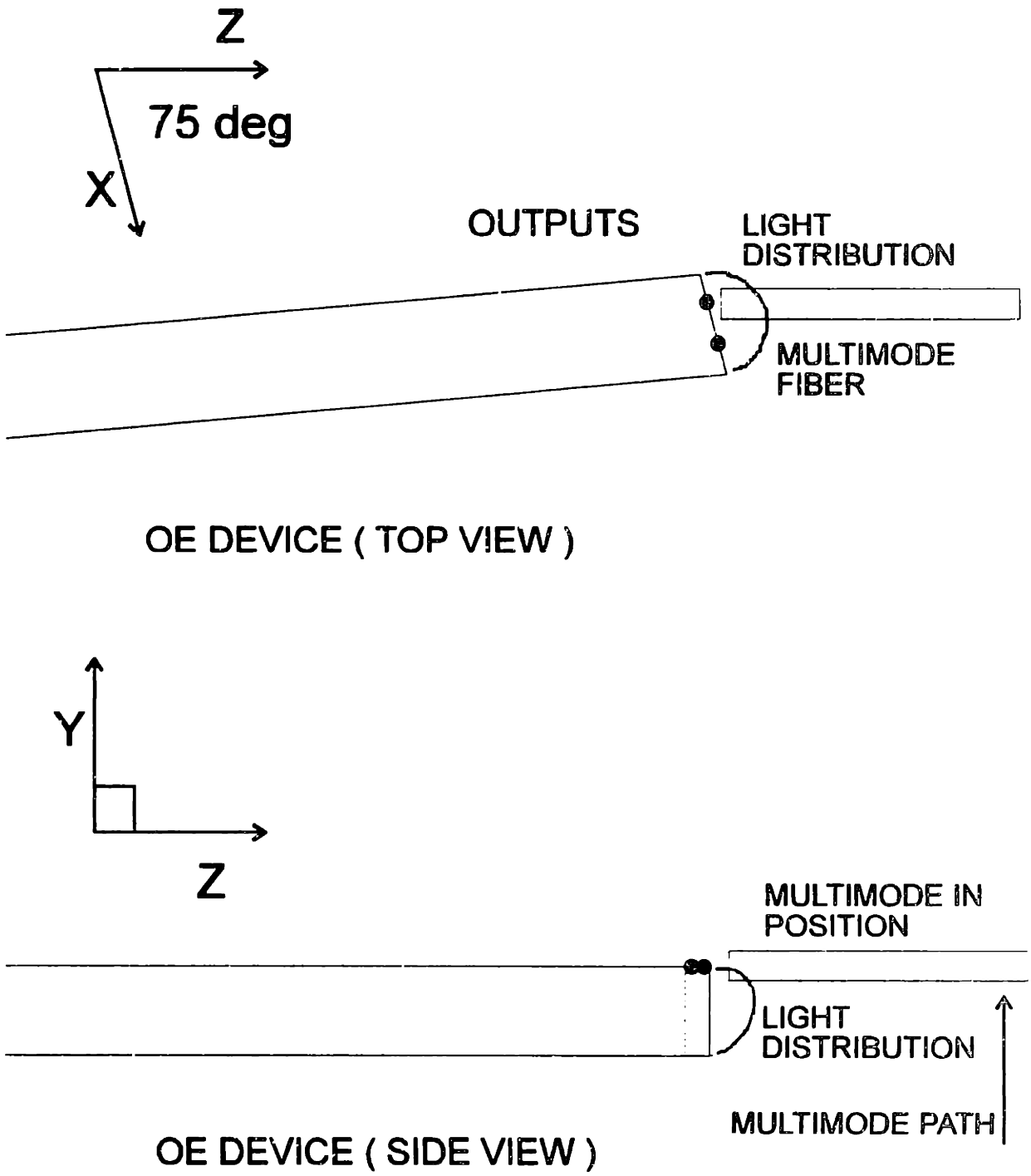

Figure 3.4 Multimode Fiber Placement

3.3 Light Throughput Maximization

After initial light coupling is obtained maximization of the light throughput is required to complete the alignment. For maximization in the x-y plane the micro manipulator is used. It was found that a simple hill climbing algorithm provided good performance for this task. The algorithm consists of moving the micro in a nine point pattern centered on the point of maximum known light throughput. After the intensity at the nine points have been examined the micro moves to the point of maximum light intensity. Figure 3.5 illustrates this procedure.

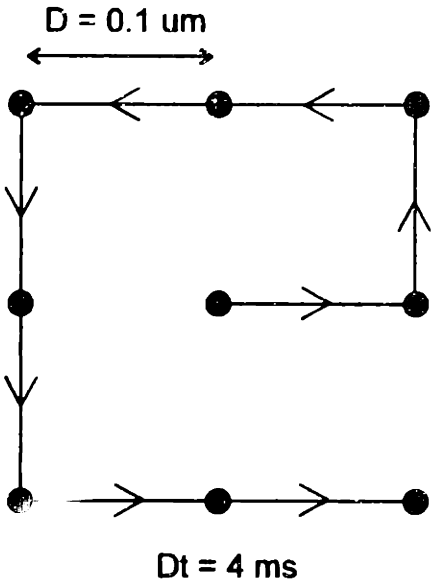

Figure 3.5 Light Maximization Algorithm for Micro Manipulator

As the process is repeated the micro climbs up the intensity profile and continually tracks the peak. This effectively allows the micro to reject low frequency disturbances such as movement of the macro manipulator and drifting of the piezoelectric actuators. There are three parameters associated with this method. The time delay between successive points, the time delay

between nine point patterns, and the distance between the points. As the time delays are decreased the time required for maximization decreases and the tracking performance improves. However, the time delays are limited by the maximum frequency at which the micro manipulator can move which in turn is limited by its bandwidth. The optimal time delays were determined experimentally to be 4ms which corresponds to an oscillation period of 25Hz. The distance between points influences the maximization time, the tracking rate, and the accuracy of the alignment. In order to achieve the alignment specification of 0.1um a step size of 0.1um or less must be used. As the step size is decreased beyond a certain point, the maximization time increases, the tracking performance decreases and the process becomes more susceptible to noise disturbance. For this reason the step size is chosen to be 0.1um which allows a maximum tracking rate of 2.5um/s. For these parameters it was found that a complete x-y alignment could be performed in less than 5s.

Maximization in the z direction consists of moving the z-stage forward with the micro continually maximizing to account for refractive effects between the device and the air gap. The amount moved is a computed distance supplied by the vision system to within 2um. A final maximization in the x-y directions is performed to complete the alignment. The maximization in the z direction can be accomplished in less than 10s.

3.4 Alignment Performance

By adding the times required for light coupling initialization and maximization it is apparent that the time required for alignment is 21.7 s/fiber. This is well within the required time of 90s. The performance of the light coupling initialization is limited mainly by the sample rate of the photodiode light sensor which effects the maximum scanning rate. If the sampling rate can be increased by a factor of 5 than a scan rate of 40 Hz

would be possible which would decrease the time required by a factor of 5. The scanning time is also directly proportional to the area that has to be scanned which depends on the uncertainty in fixturing and the vision system. If the area to be scanned could be reduced by a half, the time required would decrease by a factor of 2. With both these changes the time required to initiate light coupling could be reduced by a factor of 10 to 0.7s. The maximization time is directly proportional to the bandwidth of the micro manipulator. If the bandwidth could be doubled using improved control methods or increased structural stiffness/damping the time required would drop by a factor of two. Using variable step sizes in the hill climbing could also improve performance perhaps by a factor of two. Furthermore, direct compensation for refractive effects using the macro or the micro could reduce the z maximization time by at least a factor of two. These effects combined could reduce the maximization time required by a factor of 6 to 2.5s. It is evident from these back of the envelop calculations that there is room for significant performance optimization of the alignment process. If all measures suggested were incorporated the alignment time could be reduced to 3.2s which represents over a 600% improvement.

4. Nonlinear Control Methods for Improved System Performance

4.1 Introduction

An investigation of two promising nonlinear control methods for precision applications is performed in this chapter. In particular, a feed foward neural network controller is developed that can linearize the hysteresis behavior of piezoelectric actuators employed in the micro manipulator. Further, a controller that uses torque impulses to move the macro manipulator very small increments is developed. Using this control method it is possible to improve the resolution of a precision machine by more than an order of magnitude.

4.2 Neural Network Compensation for Hysteresis of Piezoelectric Actuators

The basic design of the micro manipulator is illustrated in Figure 4.1 and Figure 4.2. The micro manipulator is a four link flexible structure actuated by two base links composed of bimorph (cantilever) piezoelectric strips. The two forward links are inert strips. When a voltage vx is applied the end of the manipulator moves in the x direction. Applying a voltage vy moves the endpoint in the y direction. There is negligible geometrical coupling in the x and y directions because the size of the workspace (50um x 50um) is very small compared to the dimensions of the manipulator (25mm links). Static coupling in the system occurs, however, which is the result of joint stiffness in the micro. This effect can be easily modeled using a linear transformation.

The uncontrolled open loop response of the micro manipulator to actuation of a link can be determined by manually placing the tip of a

sensing fiber in proximity of a laser beam and scanning forward and backward trajectories in vx with vy set equal to zero. The result is shown in Figure 4.3. The light intensity measured is a indication of the endpoint position. The intensity as a function of x can be computed using the following formula which can be derived from optical principles:

$$I = I_{min} + (I_{max} - I_{min})\exp\left(-\left(\frac{x - x_o}{\sigma}\right)^2\right) \qquad (4.1)$$

I_{min} and I_{max} represent the minimum and maximum light intensity. x_o and σ are the center and width of the curve. The units of x are normalized such that 1 unit of x corresponds to 1V of input. In order to generate x position data using this relationship it is assumed that a linear relationship exits between x and vx on the forward path. This assumption was found not to affect the results of the investigation.

The resolution (limited by D/A resolution and electrical noise) of the micro is 5nm. However, the open loop accuracy is limited by the hysteresis nonlinearity of the actuator response. This result is apparent from the disparity between the forward and backward intensity profiles in Figure 4.3. It can be seen that the hysteresis results in a maximum deviation of 15% of the actuator range. Piezoelectric actuator hysteresis can be a significant problem in applications that use open loop control because it substantially degrades accuracy and bi-directional repeatability. The resolution, however, is not affected and it is possible to align a fiber to the required accuracy using light intensity feedback. However, a method to reduce hysteresis effects has the potential to considerably simplify path planning and decrease the time required for operations such as device characterization and scanning functions.

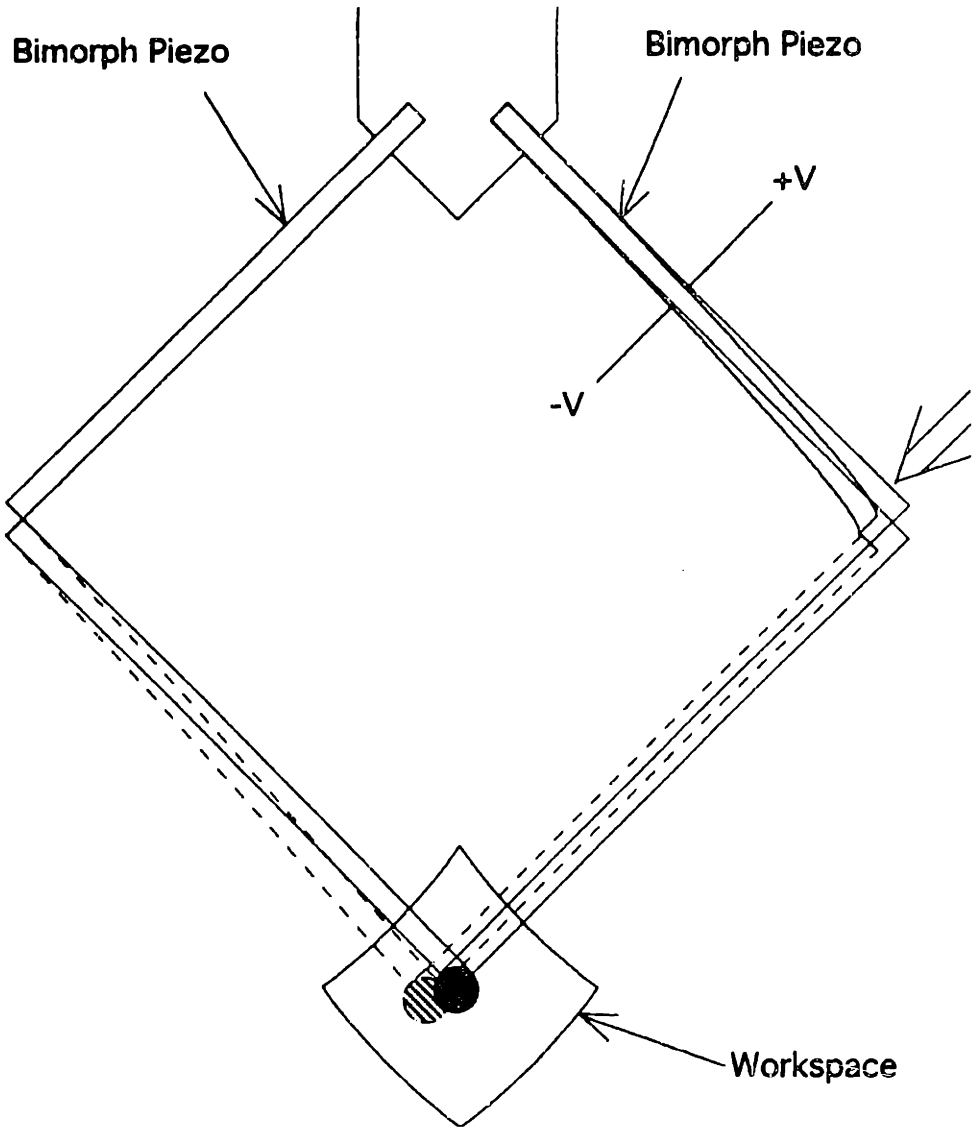

Figure 4.1 Workspace of the Micro Manipulator

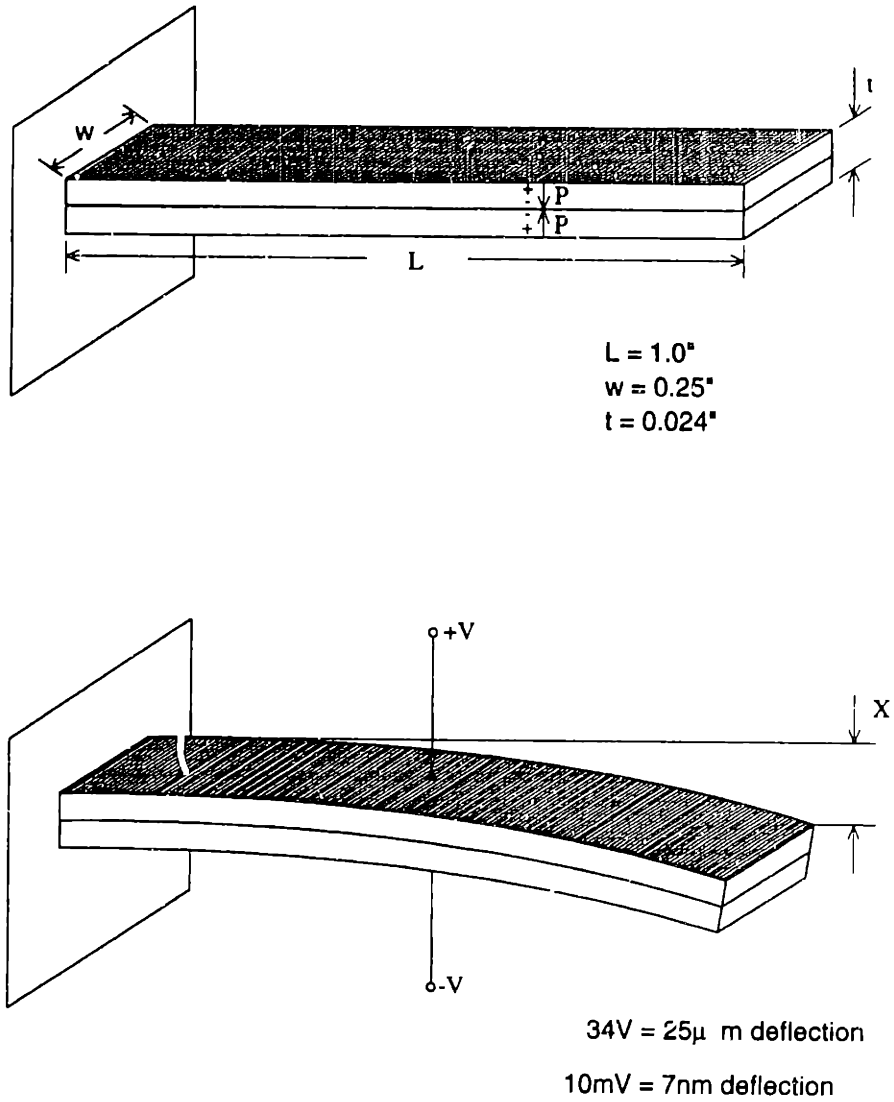

Figure 4.2 Bimorph Piezo

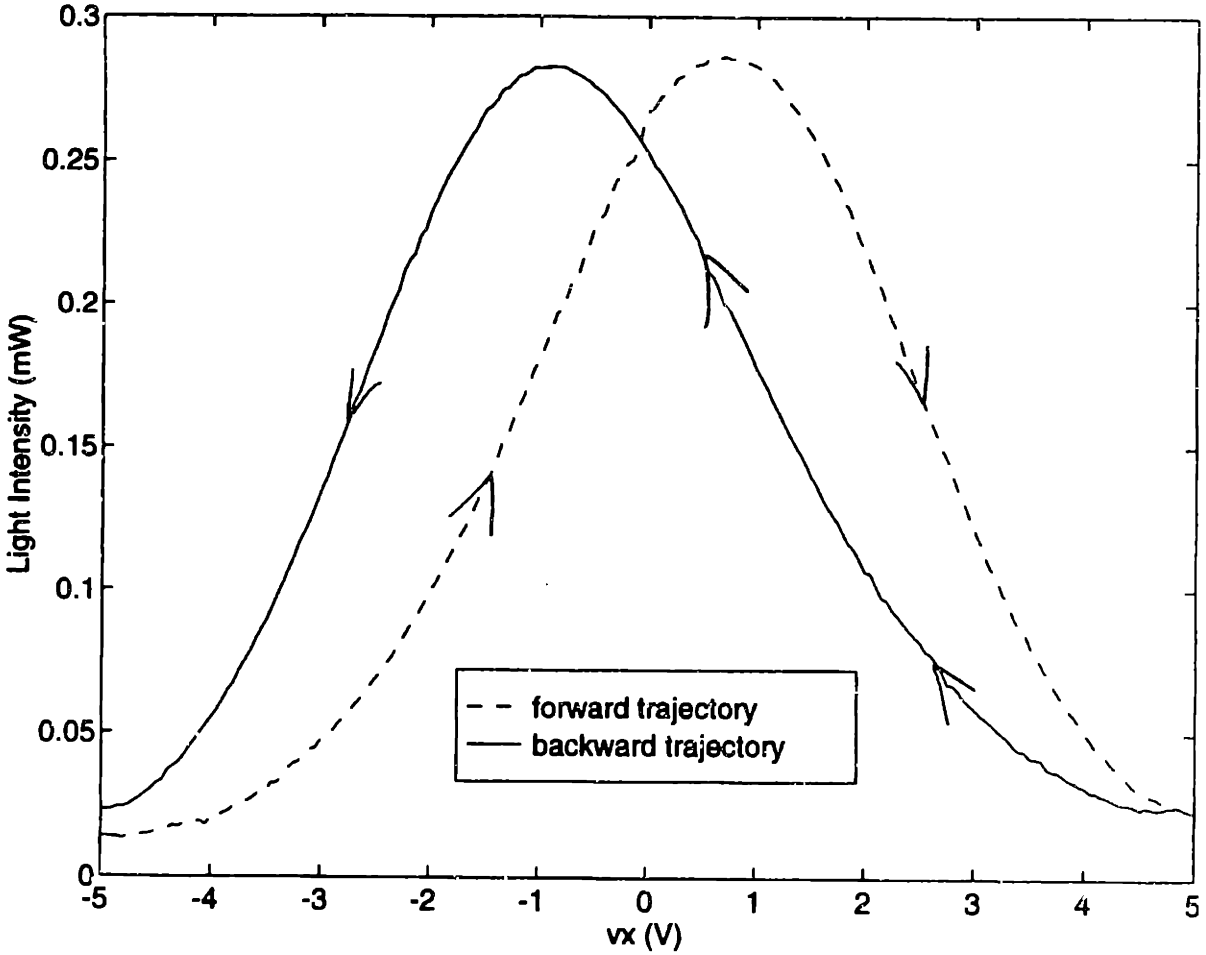

Figure 4.3 Uncontrolled Actuator Response

4.2.1 Approach

The difficulty in modeling hysteresis is that the response is dependent on the internal state of the actuator which cannot in practice be directly measured. This must be inferred from the time history of the voltage input. A hysteresis curve showing how the x position varies with vx is illustrated in Figure 4.4. The forward path is from A to B. It reverses at the turning point voltage vx = v1 and then returns along the path from B to C. The return curves for other turning point voltages v1 are also included. It is apparent that the actuator response depends on vx and v1 for the return path. In

general the x position is a function of the turning point voltages along a path v1, v2, ..., vn and the input voltage vx. This concept is illustrated in Figure 4.5. The equation expressing this relation is:

$$x = f(vx, v1, v2, \ldots, vn) \tag{4.2}$$

This function assumes a quasi static relationship. That is, the function is not rate dependent. This assumption is valid because the inertia of the micro manipulator is small and the piezoelectric actuator reaches internal equilibrium in less than 0.5ms. However, the frequency of the input should be lower than half the natural frequency of the manipulator to avoid resonance. Furthermore, creep is not significant since the time scale of typical scanning rates (0.01s) is much smaller than the creep time scale (10s-100s).

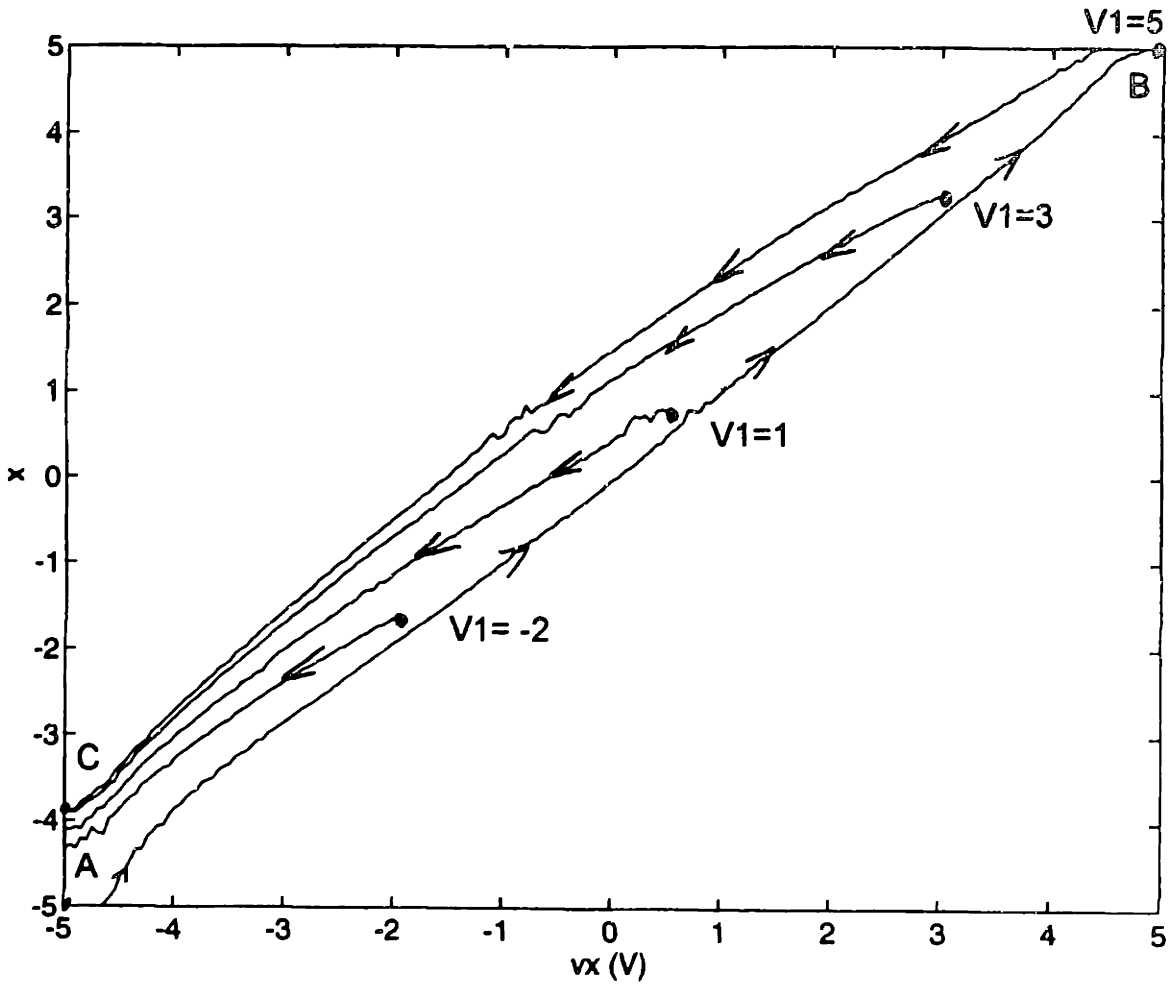

Figure 4.4 Hysteresis Curves

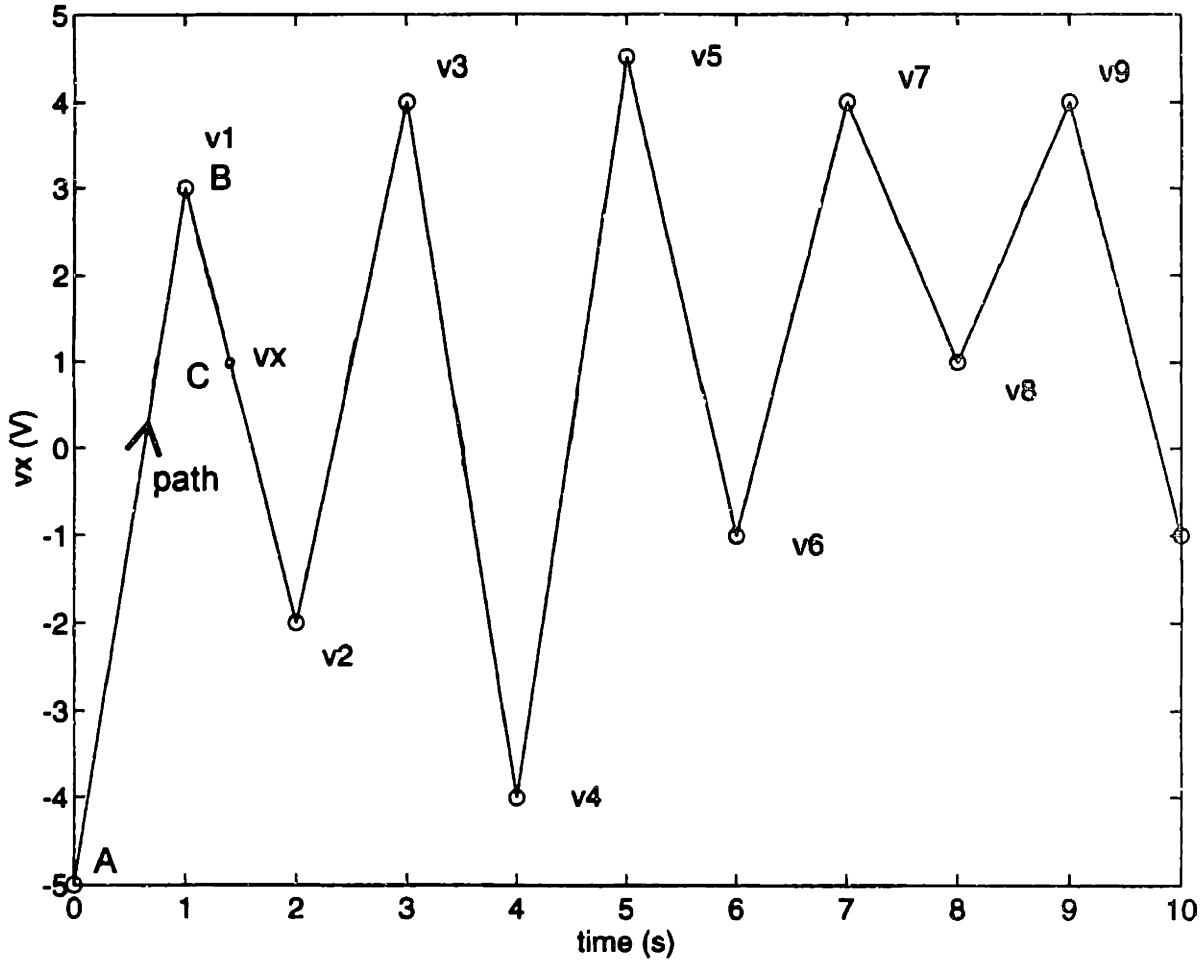

Figure 4.5 Actuator Input versus Time

The actuator response was modeled for one turning point using a two dimensional Radial Basis Function Network (RBFN). This method can be used to approximate a nonlinear function of an n dimensional vector X to any given degree of accuracy using the form:

$$F(\mathbf{X}) = \sum_{i}^{M} w_i \exp\left(-\frac{\|\mathbf{X} - \mathbf{C}_i\|^2}{\sigma^2} \right) \qquad (4.3)$$

The distribution C_i and widths σ of the Gaussians can be predetermined by the properties (frequency content) of the system to be modeled. The weights w_i are trained either off line or in real-time by numerically minimizing the approximation error with respect to them. The accuracy of the approximation increases with the number of radial basis functions M used. However, this is traded off against computational complexity for learning and real-time performance. The RBFN approach was chosen over a conventional neural network structure because the theory of configuration design is more established and it has the capability to learn in real-time using a recursive least squares algorithm.

The actuator response for one turning point voltage was modeled as:

$$x = f(vl, vx) \tag{4.4}$$

The inverse function which can be used to provide feed forward, open loop hysteresis compensation is:

$$vx = g(vl, x) \tag{4.5}$$

where x is the desired output given the last turning point voltage v1. The inverse model was trained using the direct approach since the mapping is one to one if v1 is known. The response for the forward path (before the turning point) is defined by setting v1 = -5. This part of the domain was not being used since it corresponds to an unrealistic turning point voltage. It should be noted that the one turning point model was selected for computational simplicity. It is possible to extend this approach to more than one turning point so that more complicated trajectories can be followed.

4.2.2 Results

It is apparent from the hysteresis curves of Figure 4.4 that there is a substantial noise component in the x position signal. This could potentially degrade the accuracy of the network if too many functions are used and overfitting occurs. The frequency spectrum of a typical curve is in Figure 4.6. It is apparent that the largest component corresponds to the first harmonic (f = 0.1Hz). This makes intuitive sense. However, there are substantial components up to around (f = 0.5Hz). To accurately approximate the data the Radial Basis Functions must be spaced with a spatial frequency at least equal to twice the maximum frequency desired (Shannon's Sampling Theorem). This minimum sampling bound is used to avoid modeling high frequency noise components and for computational efficiency. Thus, f = 0.5Hz corresponds to a required spatial sampling rate of $\Delta = 1/(2f) = 1$. The same sampling rate was used for the v1 direction. The Radial Basis Function receptive width was initially determined by the variance rule:

$$\sigma^2 = \pi\Delta^2 \qquad (4.6)$$

and then tuned to minimize the squared error between the network and the data.

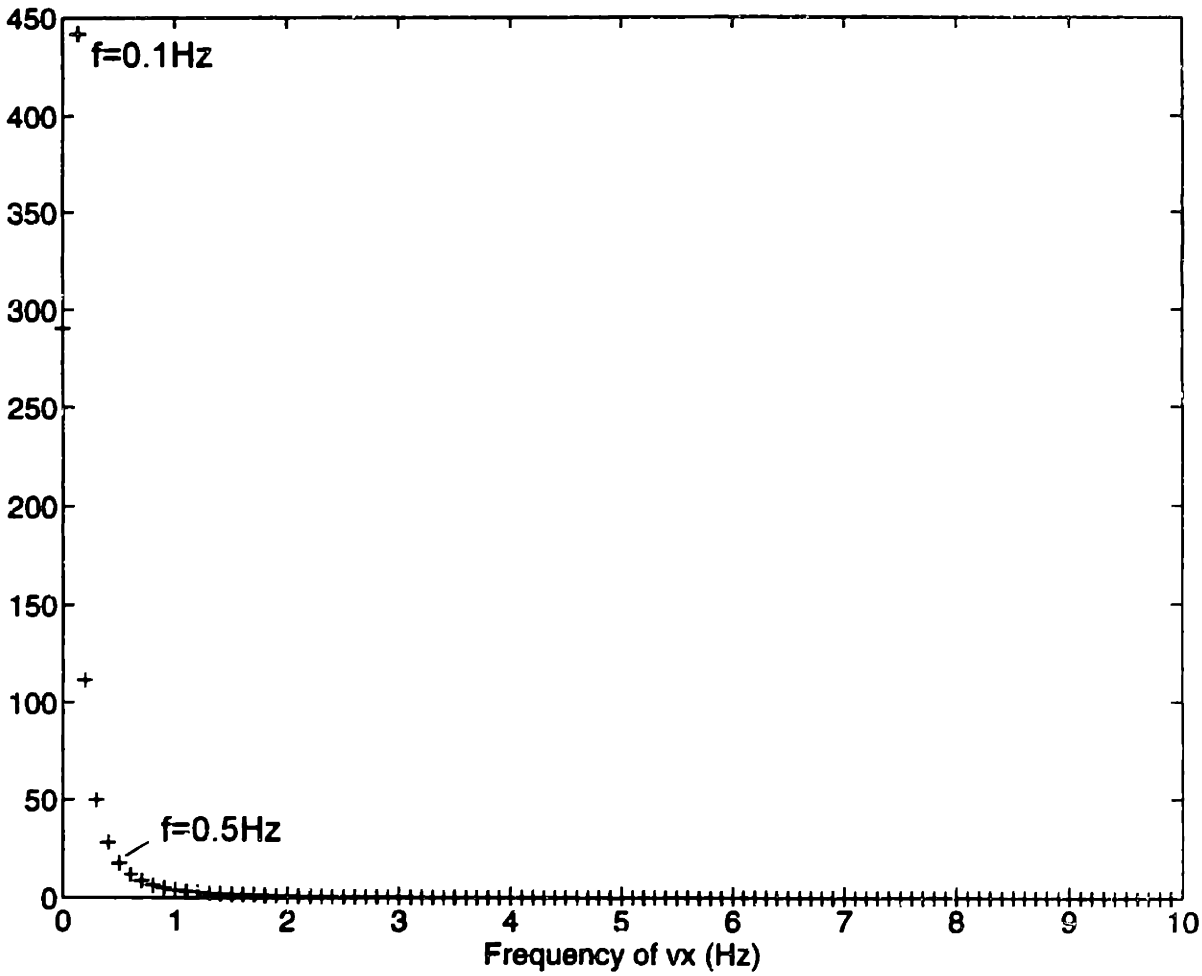

Figure 4.6 Power Spectral Density of x for v1 = 5

The forward and inverse networks were trained off line using the distribution of center points and training data displayed in Figure 4.7. It was found that 75 radial basis functions were required to approximate the forward and inverse functions. A plot of the forward model is in Figure 4.8. and the inverse is illustrated in Figure 4.9. Note that the function is valid only for the domain behind the dividing line, vx < v1 for the backward path and v1 = -5 for the forward path. The trained inverse network was implemented as a feed forward open loop controller using a rule that changes the value of v1 when the command direction reverses. A light intensity

profile was then performed. The result is shown in Figure 4.10. Comparing this to the uncontrolled actuator response in Figure 4.3 it is evident that open loop accuracy is increased by a factor of 20.

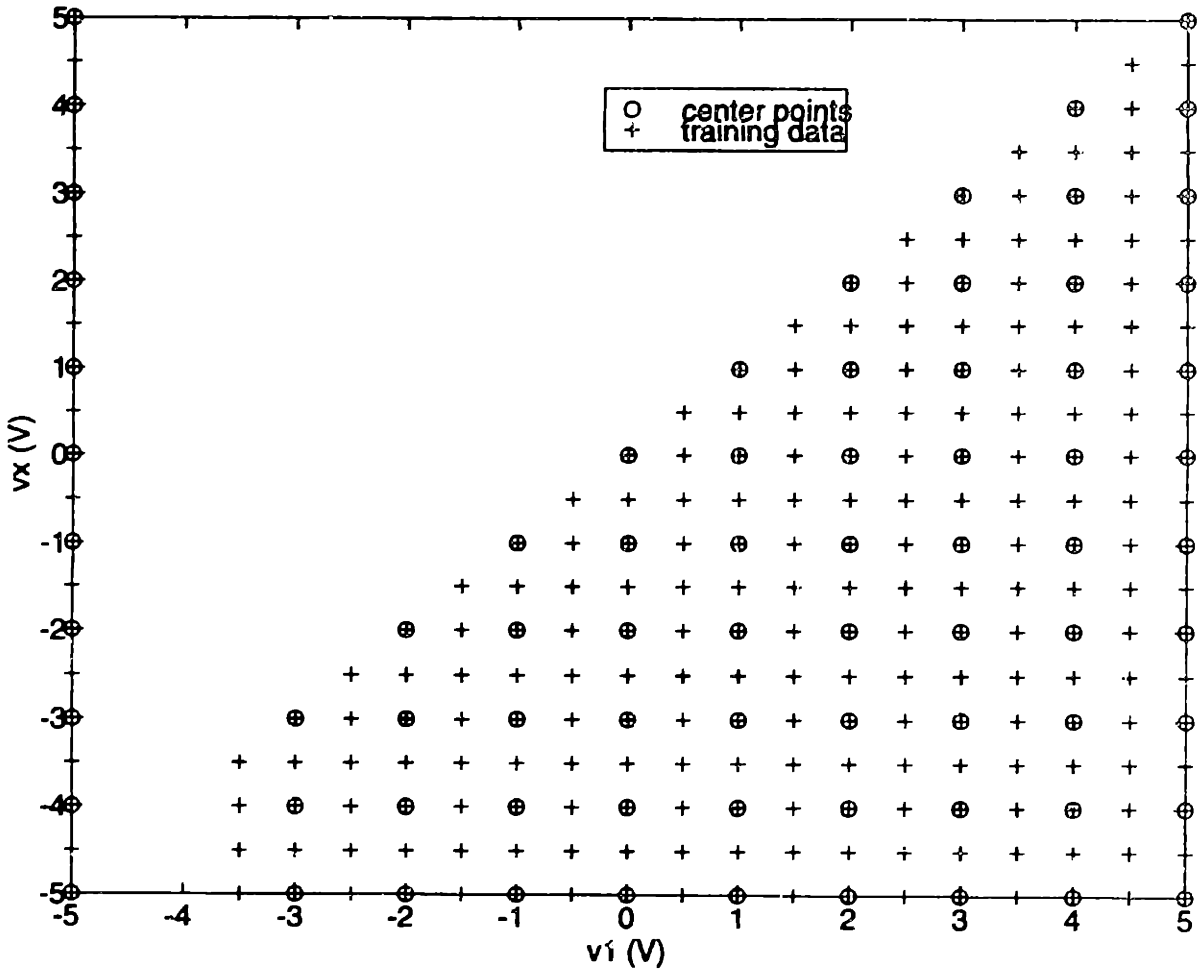

Figure 4.7 Center Points and Training Data Distribution

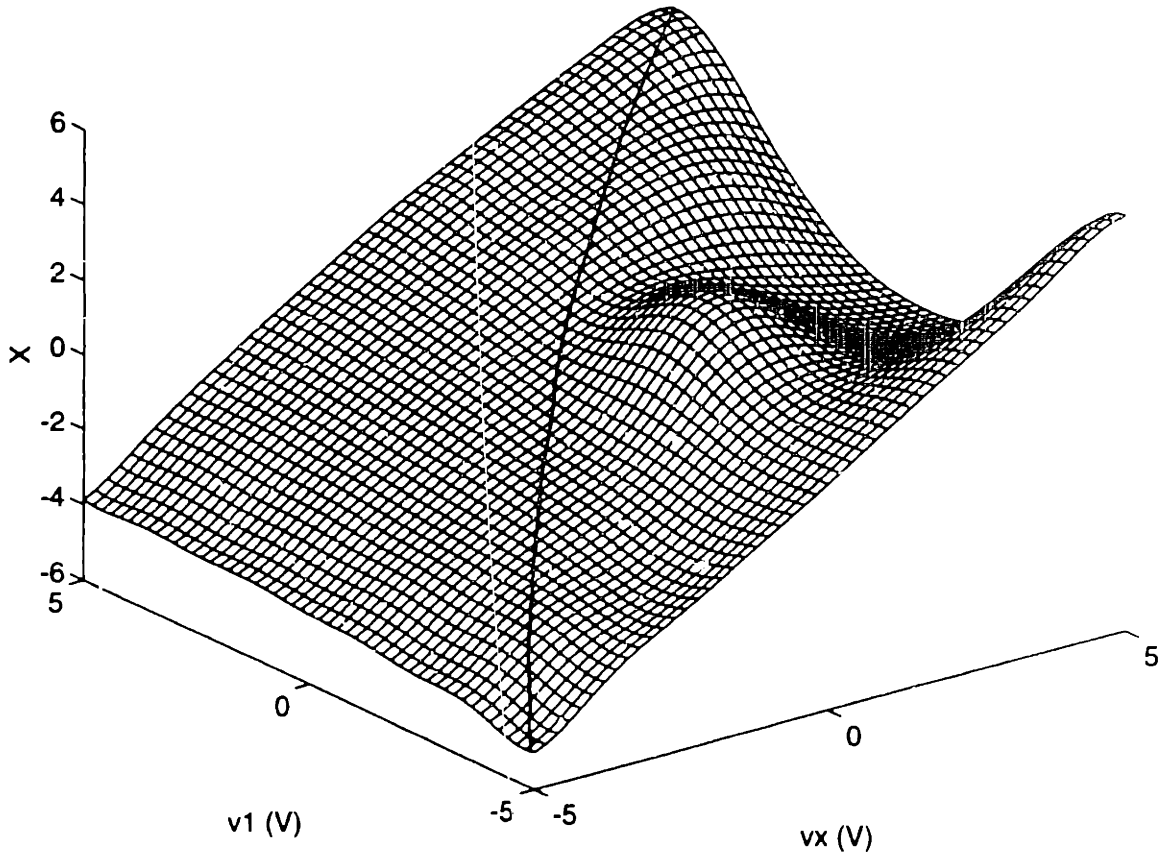

Figure 4.8 x = f(v1,vx)

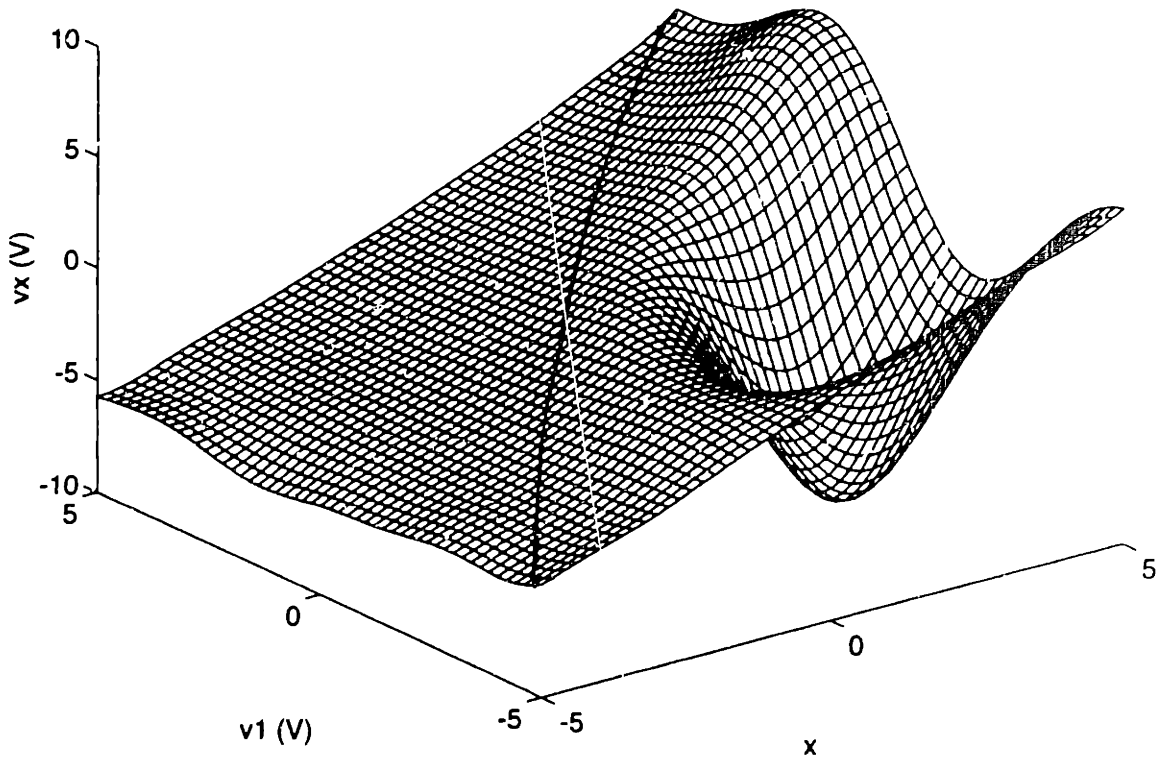

Figure 4.9 vx = g(v1,x)

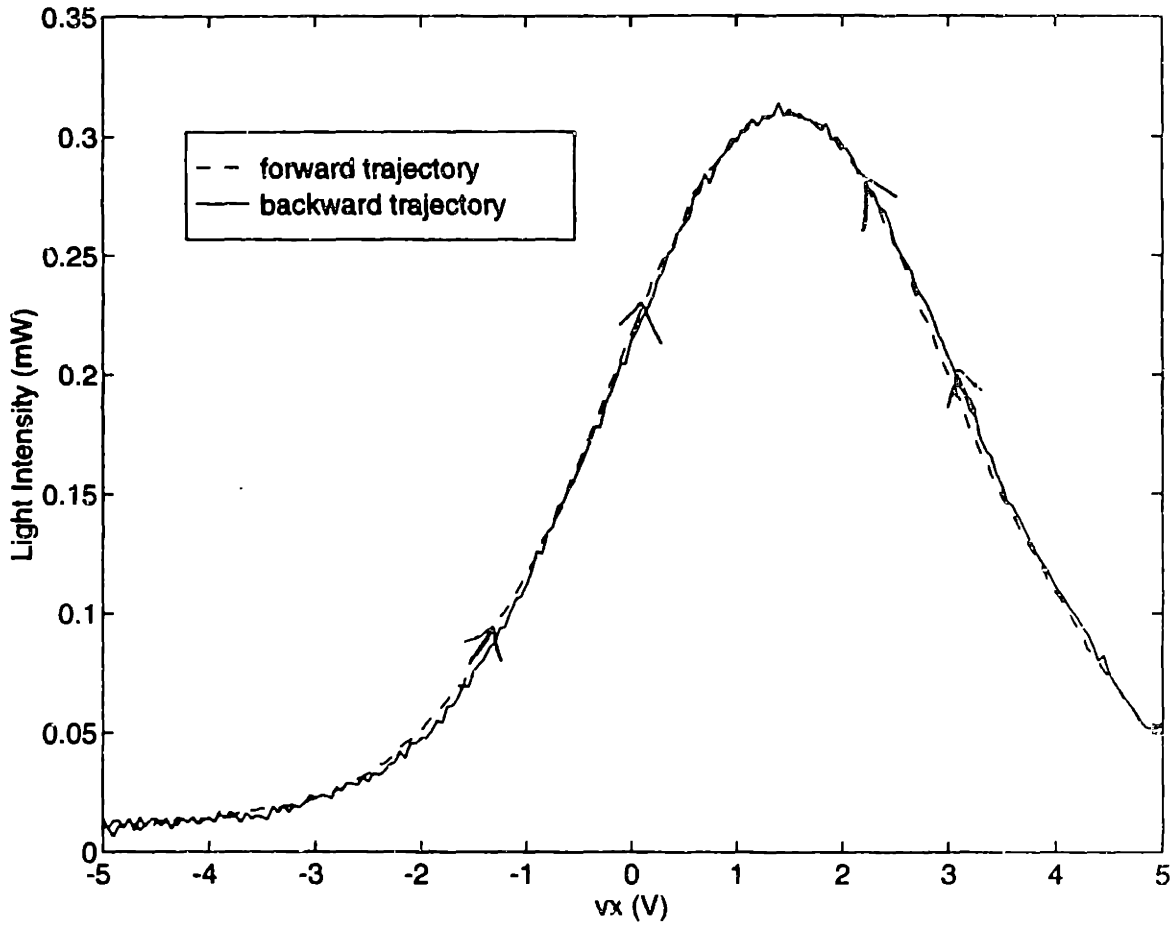

Figure 4.10 Actuator Response with Neural Network Control

4.2.3 Conclusions

In this chapter a model based on a Radial Basis Function Network was developed to describe the hysteresis nonlinearity of a piezoelectric actuator. It was determined that the actuator response is a function of the past turning point voltages and the present input voltage. The forward and inverse relationships were found for one turning point voltage and the inverse model was implemented as a feed forward open loop controller. The open loop accuracy was improved by a factor of 20.

4.3 Impulse Control to Increase Resolution of the Macro Manipulator

One of the main objectives of the macro manipulator control system is to achieve maximum resolution in the presence of high friction levels. A common problem that occurs when conventional linear control techniques are applied to high friction systems is that the system sticks before the desired position is reached resulting in a steady state error. Increasing control parameter gains often does not help beyond a certain point due to instabilities that arise. An alternative solution is to apply a large control input for a very short period of time to achieve small motion increments (see Figure 4.11). The magnitude of the impulse is typically four times the level of static friction and the duration about one millisecond. Using this technique it is actually possible to increase the resolution of a system beyond the encoder resolution for applications where some form of external feedback (such as light intensity measurement) is available. This control method known as impulse control has received some attention in recent literature [3,9,10]. However, the research does not address the effects of transmission flexibility. Transmission flexibility plays a significant part in the dynamics of many control systems and occurs in the macro manipulator due to the elastic timing belt that couples the motor shaft to the lead screw and due to the characteristic flexibility of the harmonic drive motors. The response of the z-stage to a typical impulse is shown in Figure 4.12. It can be seen that the stage moves forward 20nm after a brief transient. This provides evidence that the z-stage has the capability to move 20nm increments or less using impulse control inputs. This is seven times better than the smallest motion (140nm) that could be achieved with linear control. In this section the mathematical model developed in chapter 2 will be used to predict the impulse response of the z-stage and to guide the development of an optimal

impulse wave form. The optimal input will then be used in the development of a discrete control law. The performance of the controller will be verified with experiment and simulation. In addition, the resolution capability of the macro manipulator using impulse control will be experimentally investigated.

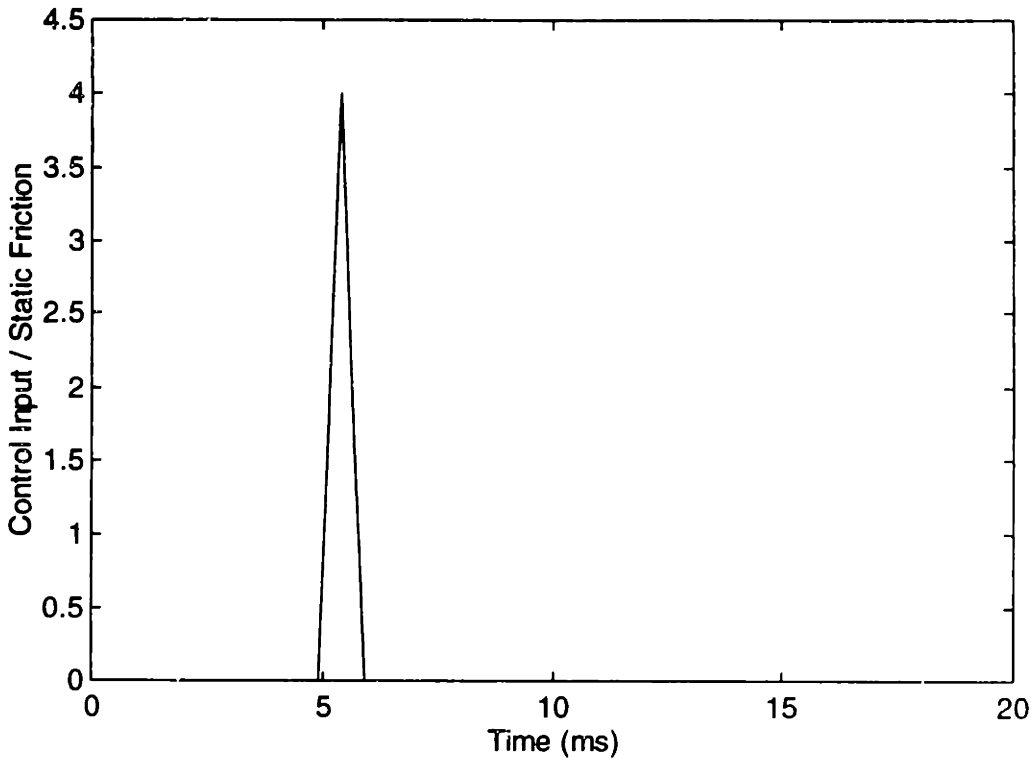

Figure 4.11 Impulse Control Input

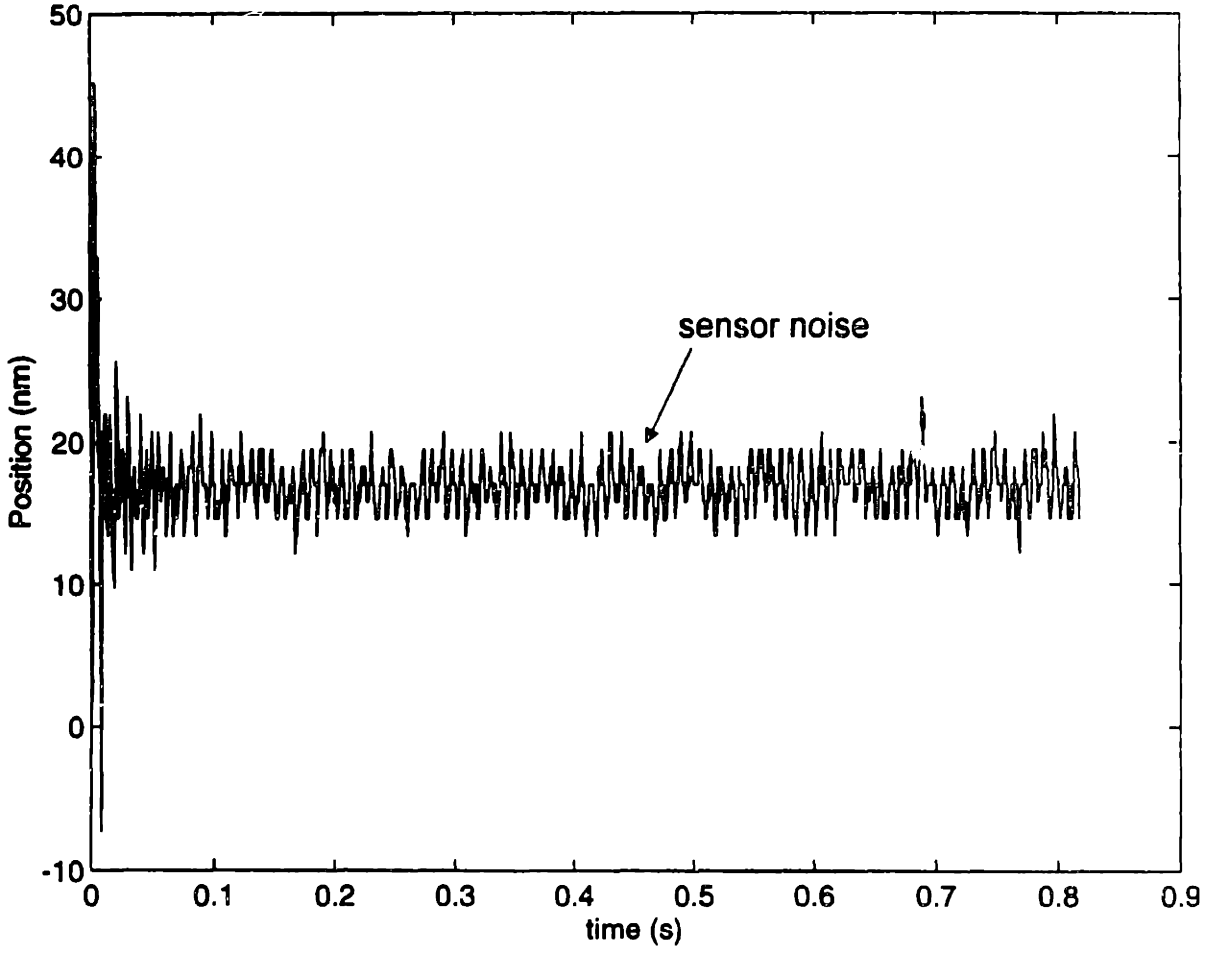

Figure 4.12 Impulse Response of Z-stage

4.3.1 Impulse Response

Previous work on impulse control methods has focused on impulses of fixed shape, either square or triangular. In an attempt to improve performance the response for a generalized impulse shape consisting of the first two harmonics of a general series expansion with fixed endpoints was considered. The equation for this input u is:

$$u(t) = a_1 \sin\left(\pi \frac{t}{T}\right) + a_2 \sin\left(2\pi \frac{t}{T}\right), \quad 0 \le t \le T \tag{4.7}$$

where a1 and a2 are variable coefficients, and T is the pulse width. The system was simulated for a1 = 1.5 fsm (static friction level of the motor inertia), a2 = 12.5 fsm, and T = 1ms. The input is shown in Figure 4.13. The angular positions are shown in Figure 4.14. The velocity profiles in Figure 4.15 are particularly revealing. It is apparent that most of the motion of the motor inertia occurs during the 1ms impulse whereas most of the motion of load inertia occurs after the impulse. This is a result of the indirect link due to the flexible timing belt and is significantly different than the response of a one inertia system. The resulting z displacement of 35nm is shown in Figure 4.16.

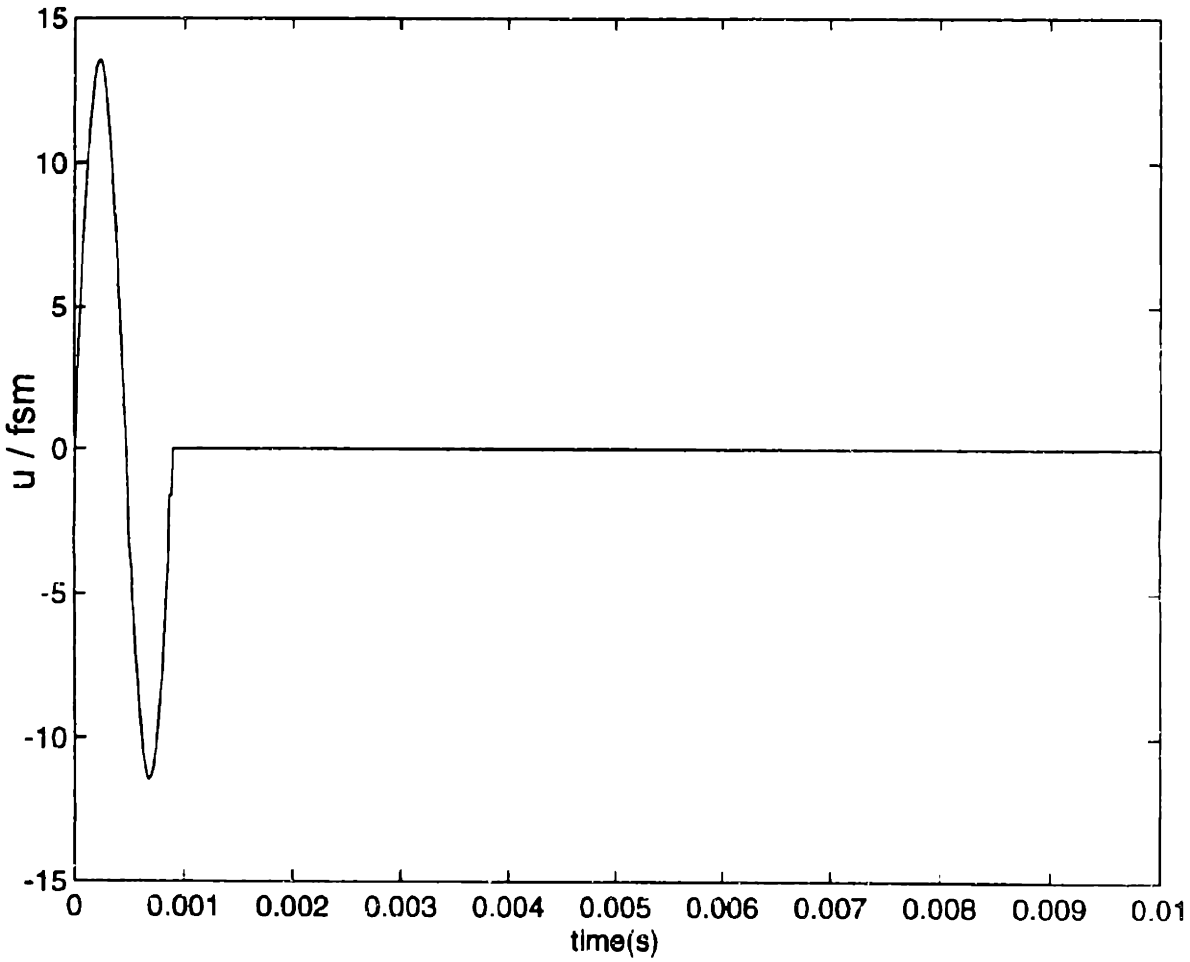

Figure 4.13 Impulse Response Input, a1 / fsm = 1.5 , a2 / fsm = 12.5

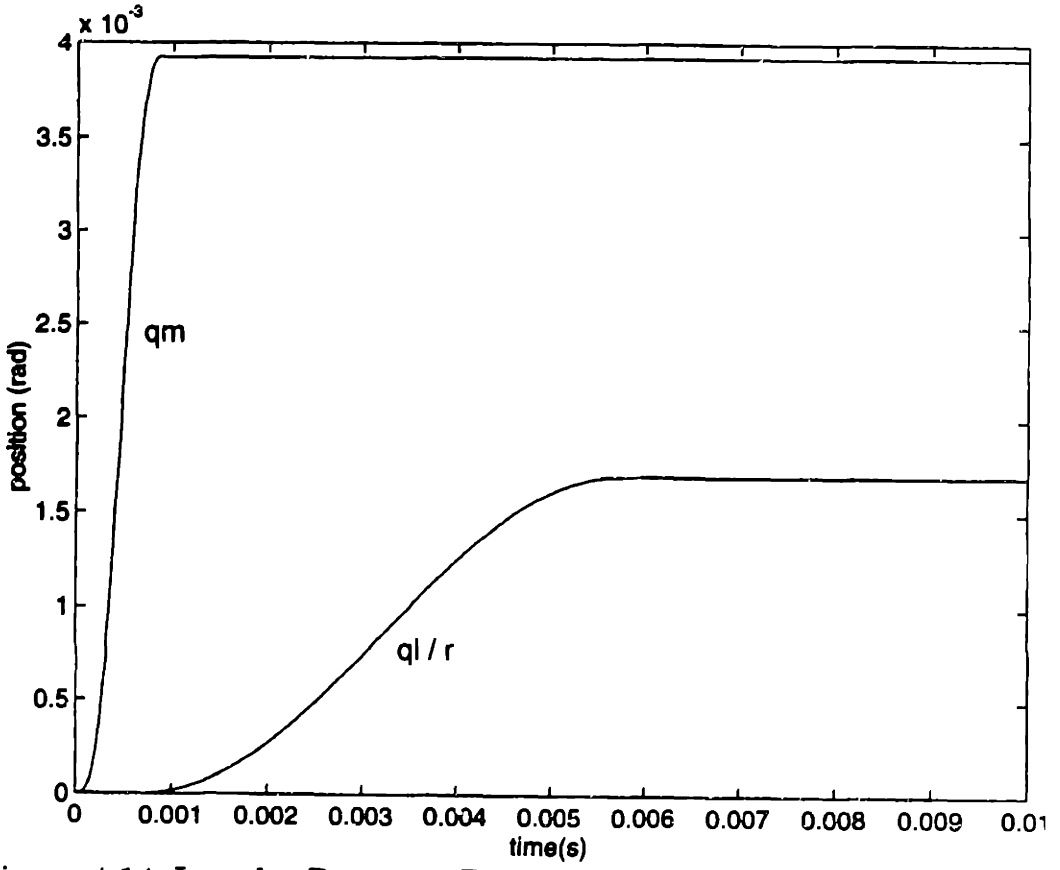

Figure 4.14 Impulse Response Positions, a1 / fsm = 1.5 , a2 / fsm =12.5

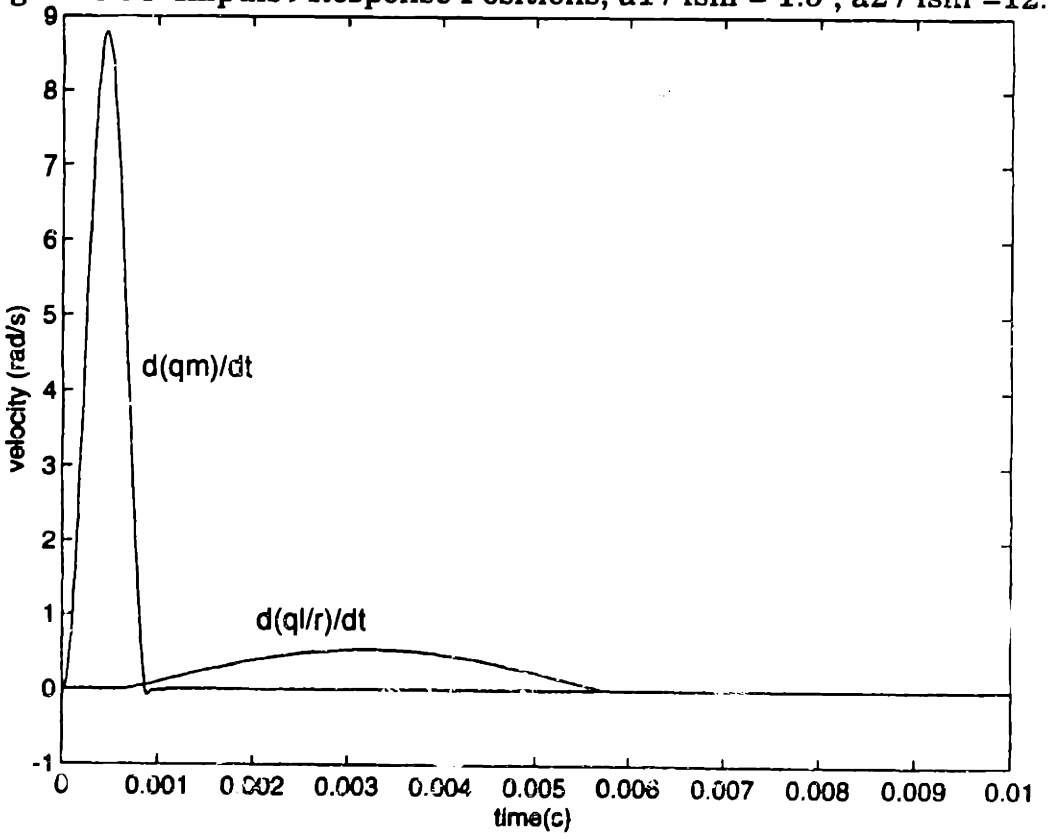

Figure 4.15 Impulse Response Velocities, a1 / fsm = 1.5 , a2 / fsm = 12.5

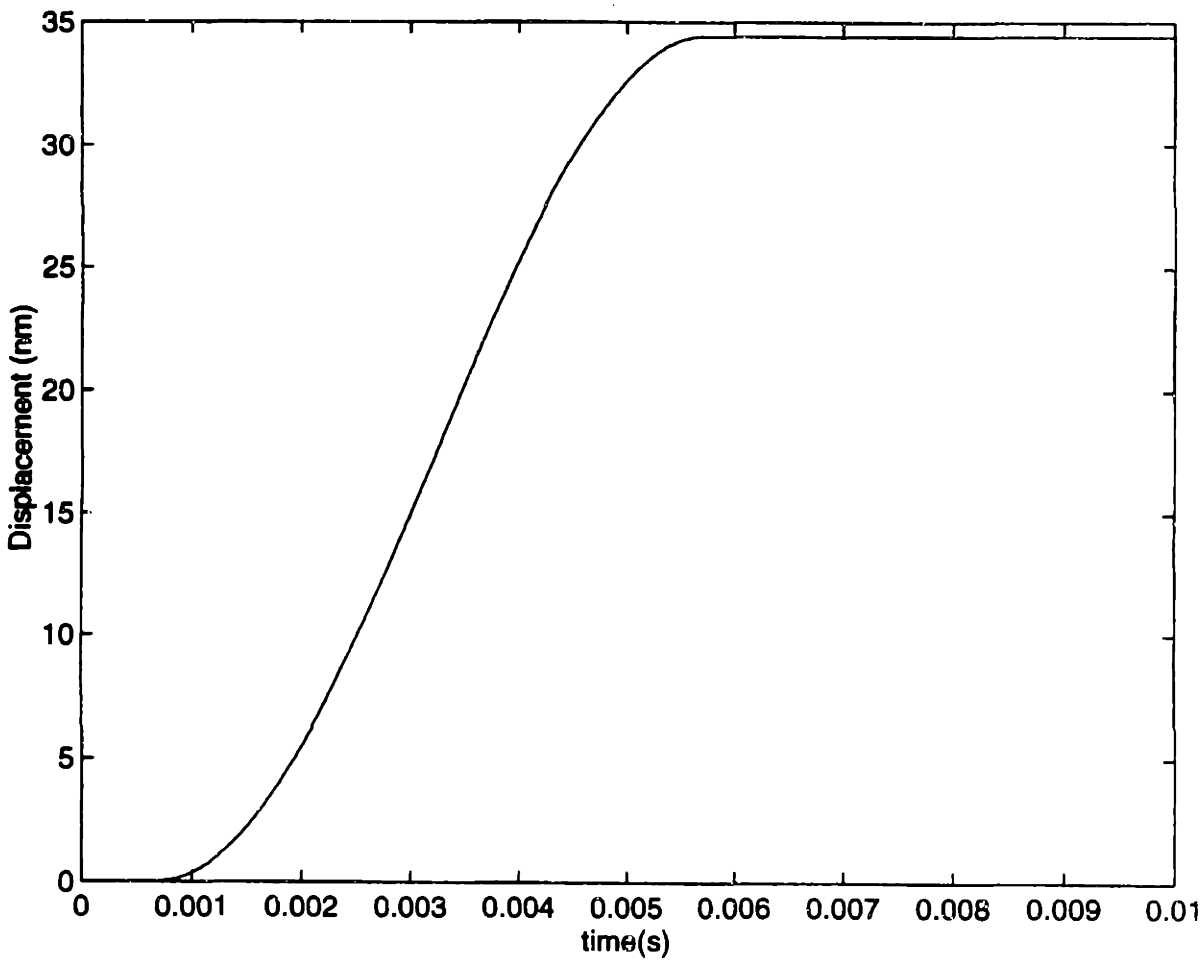

Figure 4.16 Impulse Response Displacement, a1 / fsm = 1.5 , a2 / fsm = 12.5

In general, the displacement of the system due to an impulse is a function of a1 and a2 when T is constant. For this investigation T was set equal to 1ms to simplify analysis. This value seemed to provide good control performance. It is desirable to have T as short as possible to provide insensitivity to friction parameter uncertainty, but in practice system bandwidth limitation, amplifier saturation, and unwanted excitation of mechanical vibrations tend to limit the input frequency.

The displacement δ over the range $0 < a1 < 5$ fsm, $0 < a2 < 20$ fsm is shown in Figure 4.17. It is apparent that the system moves forward only when a1 is above some threshold. In other words there is a dead zone with

respect to a1. It is also evident that the size of the dead zone can be decreased by increasing a2. Since a dead zone is undesirable for control system design a2 will be chosen to eliminate the dead zone. This occurs when a2 = 12.5 fsm. The response of the system as a1 is varied for a2 = 12.5 fsm is shown in Figure 4.18. It can be seen that the displacement is approximately a parabolic function of a1:

$$\delta = f(a1) = b \cdot a1^2 \, sgn(a1) \tag{4.8}$$

where $a2 = 12.5\,fcm \cdot sgn(a1)$, T = 1ms, and b is an empirical constant. It is important in control system design for this relationship to be insensitive to system parameter uncertainties within a given range. From experiments and simulations it was found that the most significant factors are the static friction level of the load fsl and more subtly the internal state of the system. In physical terms, the transmission spring energy can be stored in the system as a result of friction and suddenly released after an impulse resulting in a much larger displacement than anticipated. This effect can be eliminated by moving to motor inertia q_m (with a linear or impulse controller) so that no spring energy is stored in the timing belt. However, practical limitations on the measurement resolution of q_m results in some uncertainty in the knowledge of the system spring energy. The uncertainty in q_m can be used as a direct measure of system energy uncertainty if q_l is initially zero. The uncertainty of the system based on encoder resolution is δq_m=3.0E-4rad. The uncertainty of fsl is 10%. Figure 4.19 shows the range of response for the combined parameter variations. It is apparent that the dead zone is small and the parabolic relationship holds for the range of parameters. From these results it can be concluded that the system sensitivity to uncertainties is significant but acceptable.

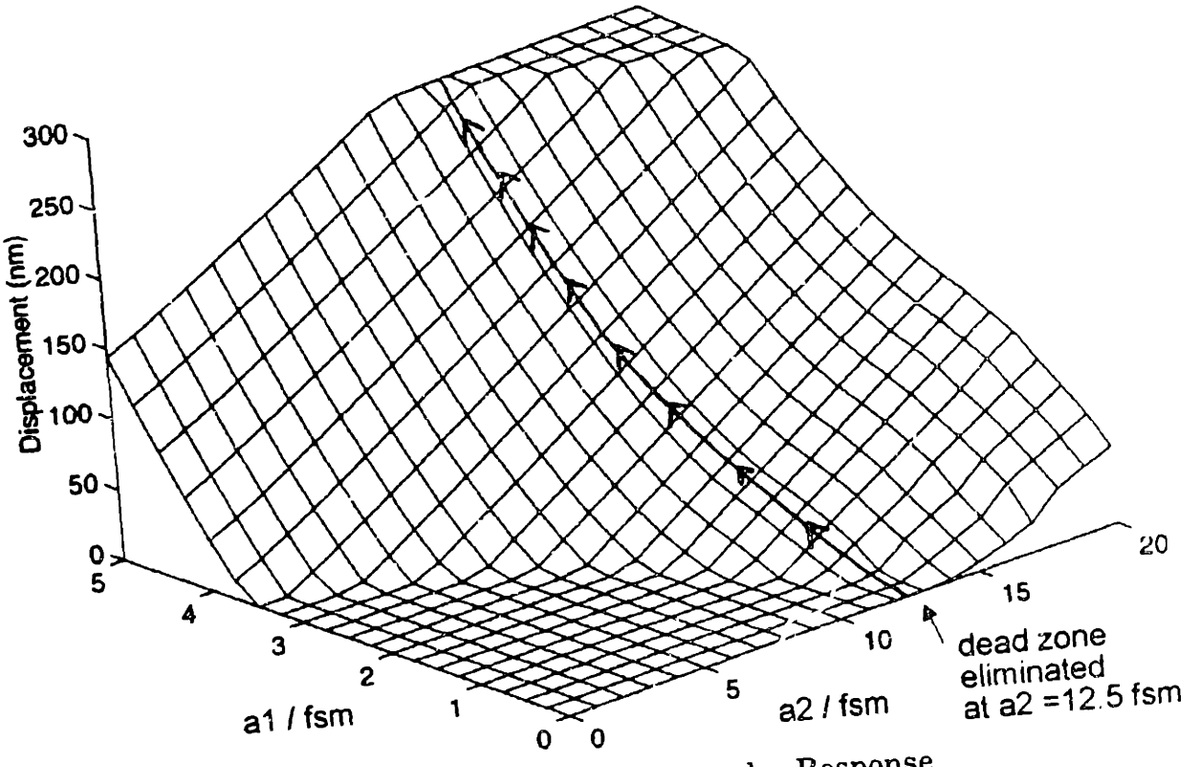

Figure 4.17 Generalized Impulse Response

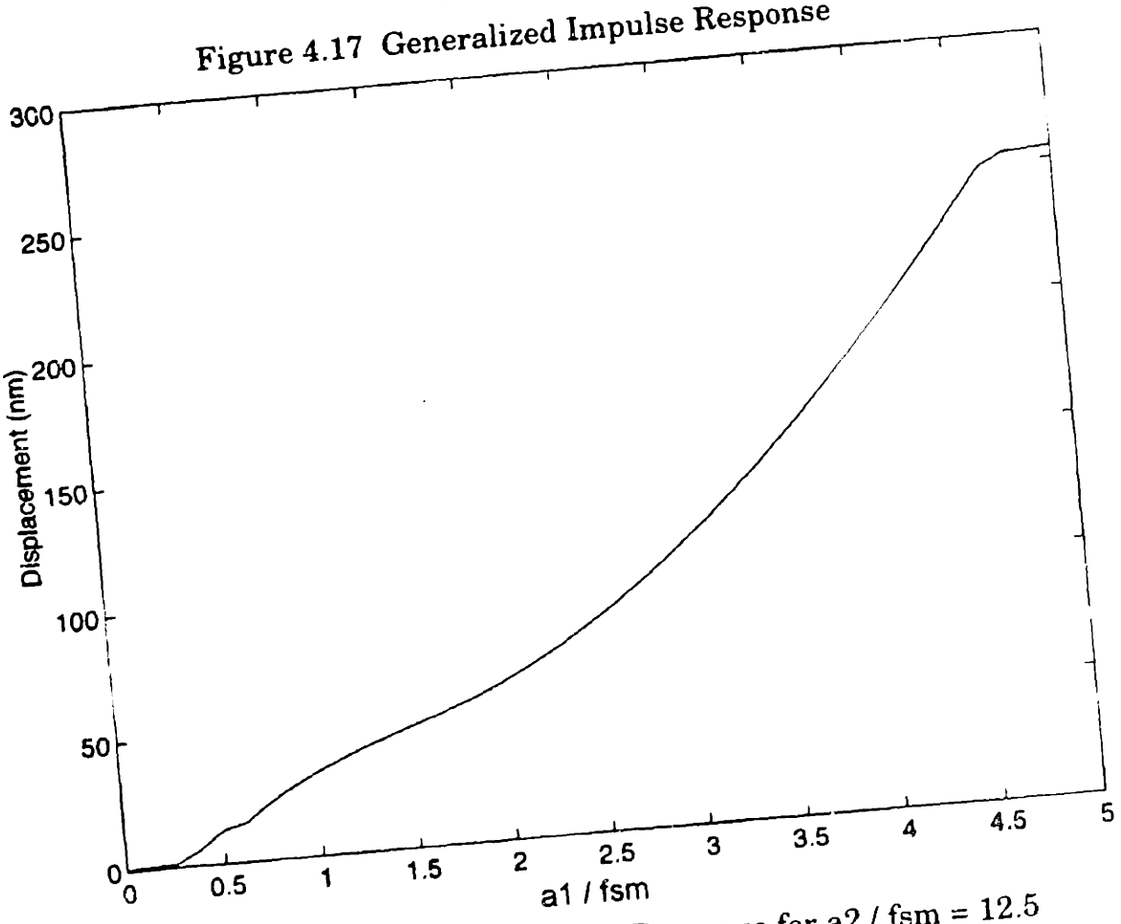

Figure 4.18 Generalized Impulse Response for a2 / fsm = 12.5

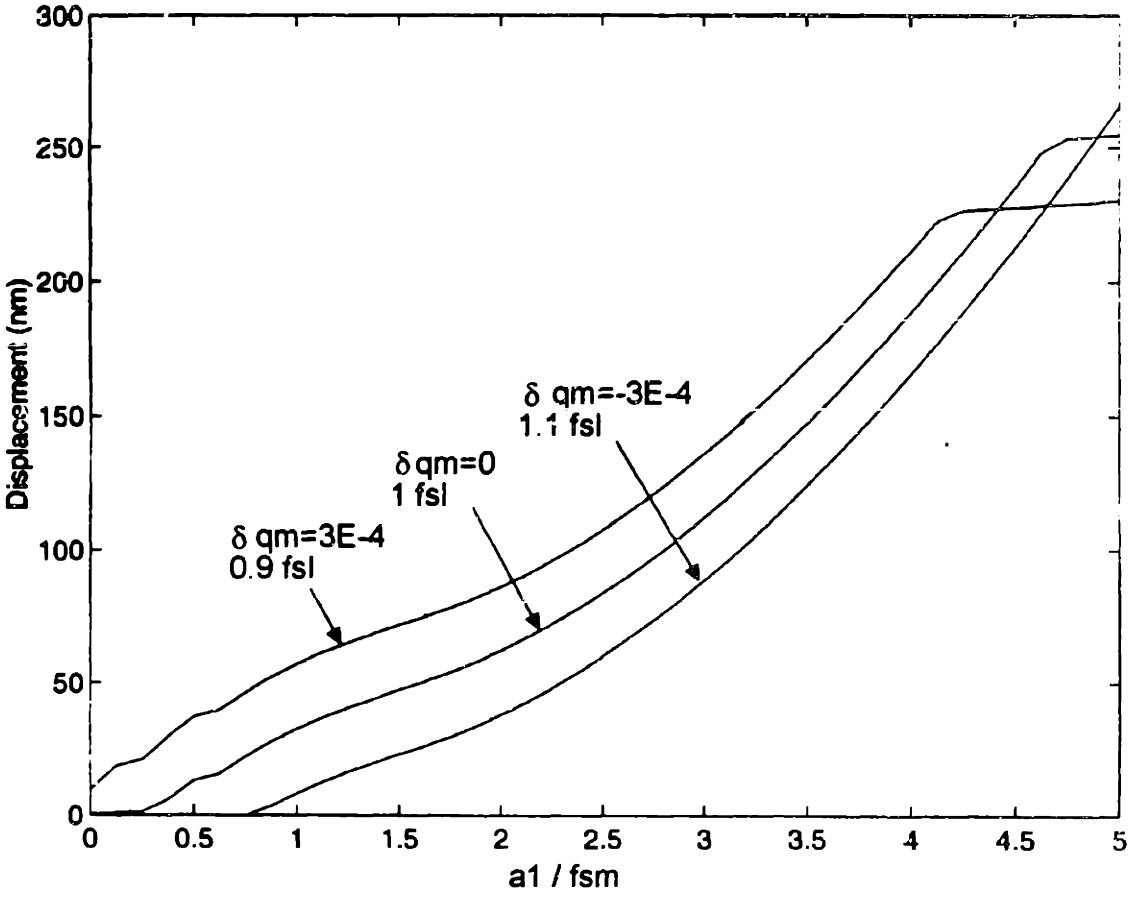

Figure 4.19 Impulse Response Parameter Sensitivity

4.3.2 Impulse Controller

A closed loop feedback control system based on discrete impulses has the form:

$$x[k+1] = x[k] + \delta[k+1] \tag{4.9}$$

x[k] and x[k+1] represent the x position at time t and t + Δt. δ[k + 1] is the x displacement due to an impulse input at time t. This equation represents a

first order difference equation with input $\delta[k+1]$. $\delta[k+1]$ can be considered as an input variable since for any desired displacement value within a given range we can calculate using equation (4.8) the required a1. This technique is dependent on our ability to invert the relationship between δ and a1 which shows why a dead zone is highly undesirable in the system response as it makes the relationship difficult to invert. With this in mind asymptotic tracking can be achieved using the simple proportional control law:

$$\delta[k+1] = k_c e[k] \tag{4.10}$$

where:

$$e[k] = x_d - x[k] \tag{4.11}$$

and xd is the desired x position. The controller is asymptotically stable for:

$$0 < k_c < 2 \tag{4.12}$$

This result depends on whether equation (4.8) is insensitive to system uncertainties which was earlier verified.

The impulse control system developed was simulated for a desired x position of 100nm and kc = 1. The simulation includes Guassian uncertainty of the friction parameters (10%), internal state (3.0E-4 for q_m) and position measurement (4nm). The results are illustrated in Figure 4.20. It is apparent that a tracking error of less than 10nm is achieved after an initial overshoot. This implies a resolution of 10nm which is a factor of 12 better than conventional linear control.

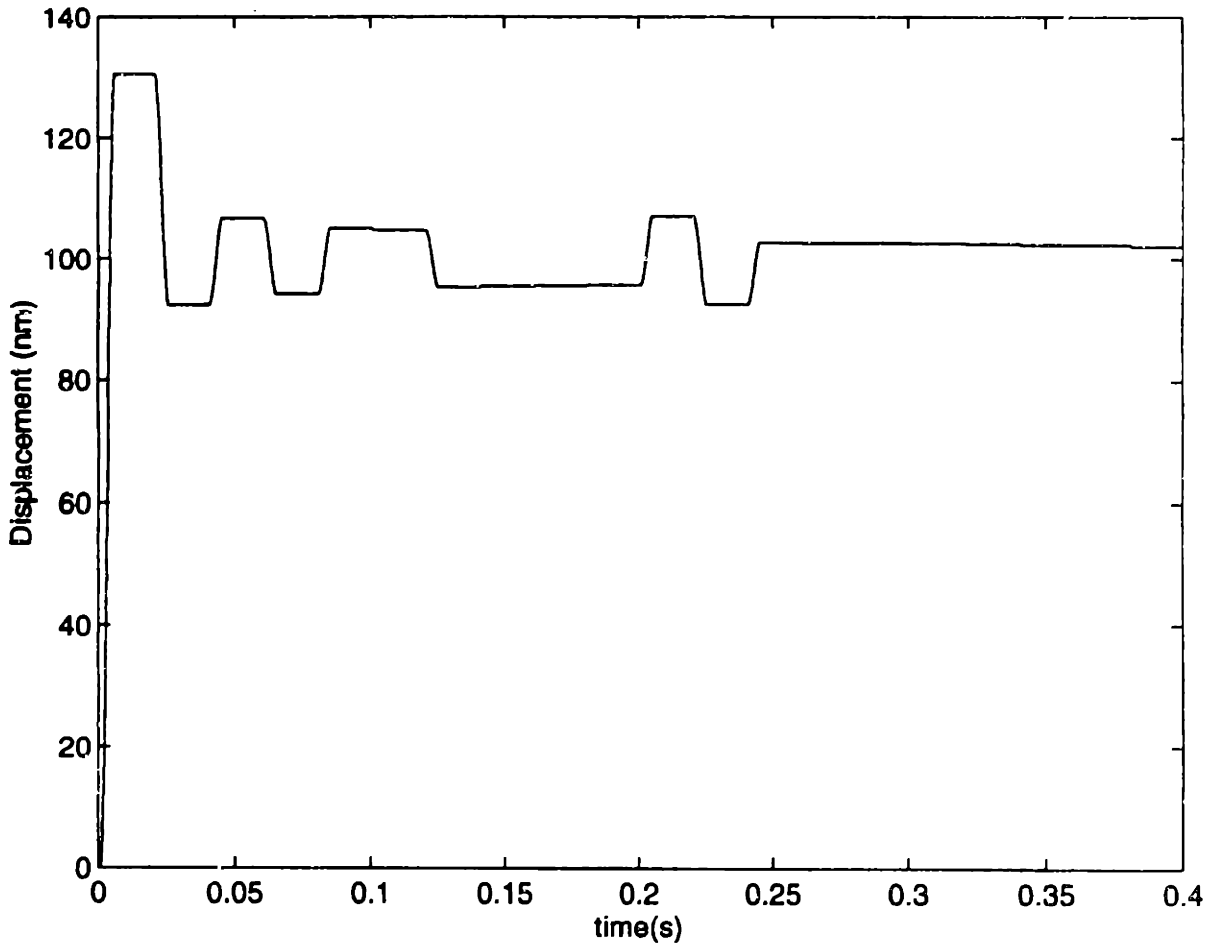

Figure 4.20 Impulse Control Response for xd = 100nm, kc = 1

4.3.3 Experimental Results

The response of the five-bar to a generalized impulse was experimentally determined. The results are in Figure 4.21. It can be seen that a similar pattern to the z-stage occurs and that the dead zone can be removed for a2 = 2.3 fsm. The response for a2 = 2.3 fsm shows the parabolic relationship between a1 and displacement that was previously observed. The impulse controller was implemented for the five-bar using capacitance sensors for feedback and using a sample rate of 250ms. The results for four different

initial conditions are shown in Figure 4.22. It is apparent that the system has a settling time of under 3s and that a steady state error of less than 0.15um could be achieved. This is equal to less than one tenth of an encoder tic. It was found that the sample rate could not be increased much beyond 250ms without the impulse response becoming less predictable. The physical reason for this is that the inertia must slide to a complete stop in order for the next impulse response to be consistent. The resolution performance of the five-bar and the z-stage under open loop impulse control was also determined. The results for the five-bar are shown in Figure 4.23. It is apparent that a resolution of 0.2um is achieved. This is a factor of 18 times better than that achieved using PID control in chapter 2. The position as a function of time shows consistent one directional motion as expected. The resolution of the z-stage is shown in Figure 4.24. It can be seen that the impulse response is not as consistent as the five-bar, but at 20nm still represents a factor of 7 improvement over PID control. The position response seems to decrease with time for the z-stage. The reason for this unexpected behavior was unclear and not predicted by the model. This could be an indication that true sliding is not occurring at the frictional interface. However, this hypothesis could be difficult to verify. It may indicate a need for on-line estimation of the impulse response relationship or perhaps an adaptive control approach.

It is evident from the experimental tests that a dramatic improvement in resolution is possible using impulse control. This improved resolution performance could make it possible to perform a complete alignment using the macro manipulator without the need for constant light feedback. However, the sample rate limitation would increase the time required for alignment. The increased resolution could also be used for other applications not requiring high bandwidth.

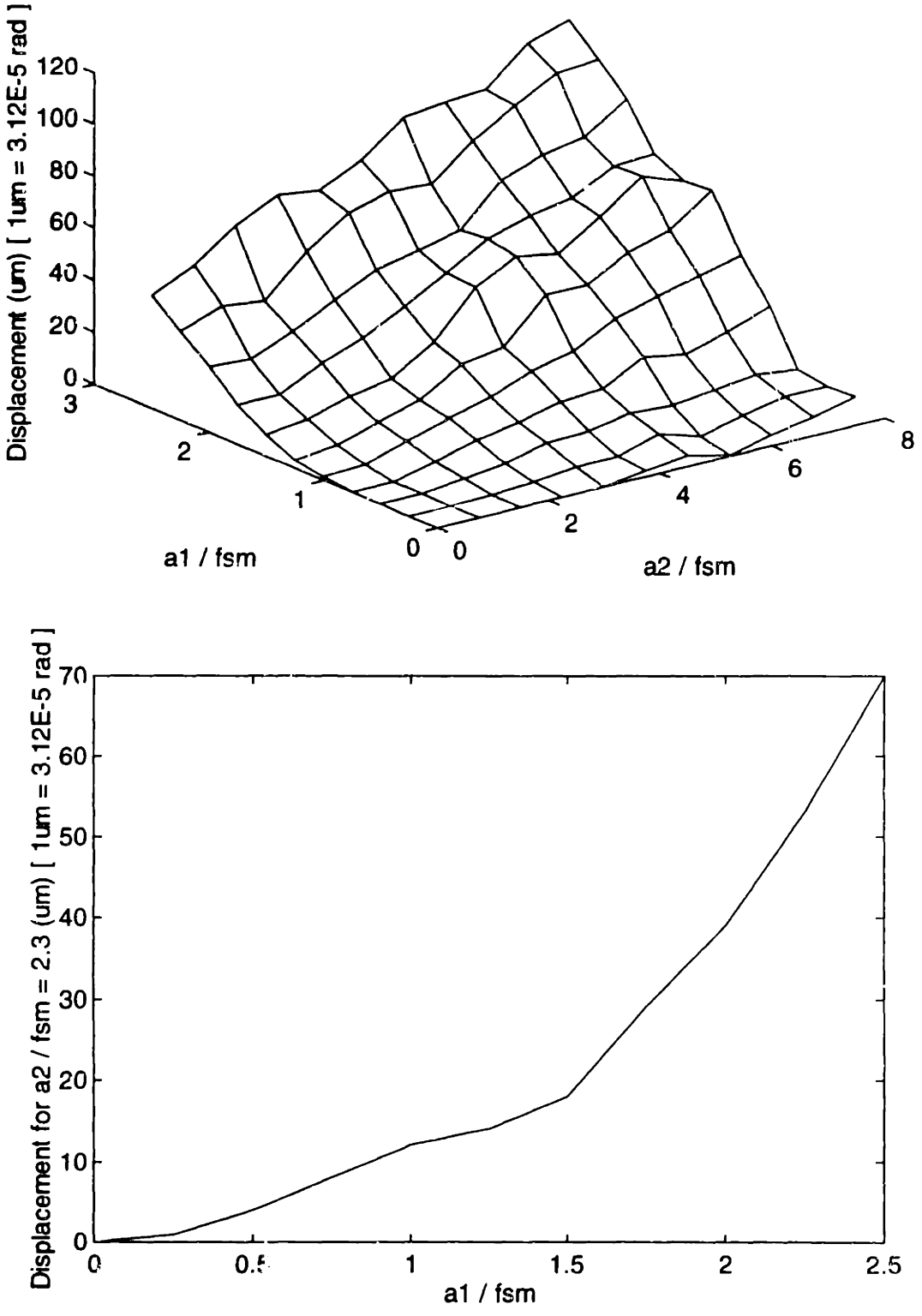

Figure 4.21 Generalized Impulse Response of Five-bar

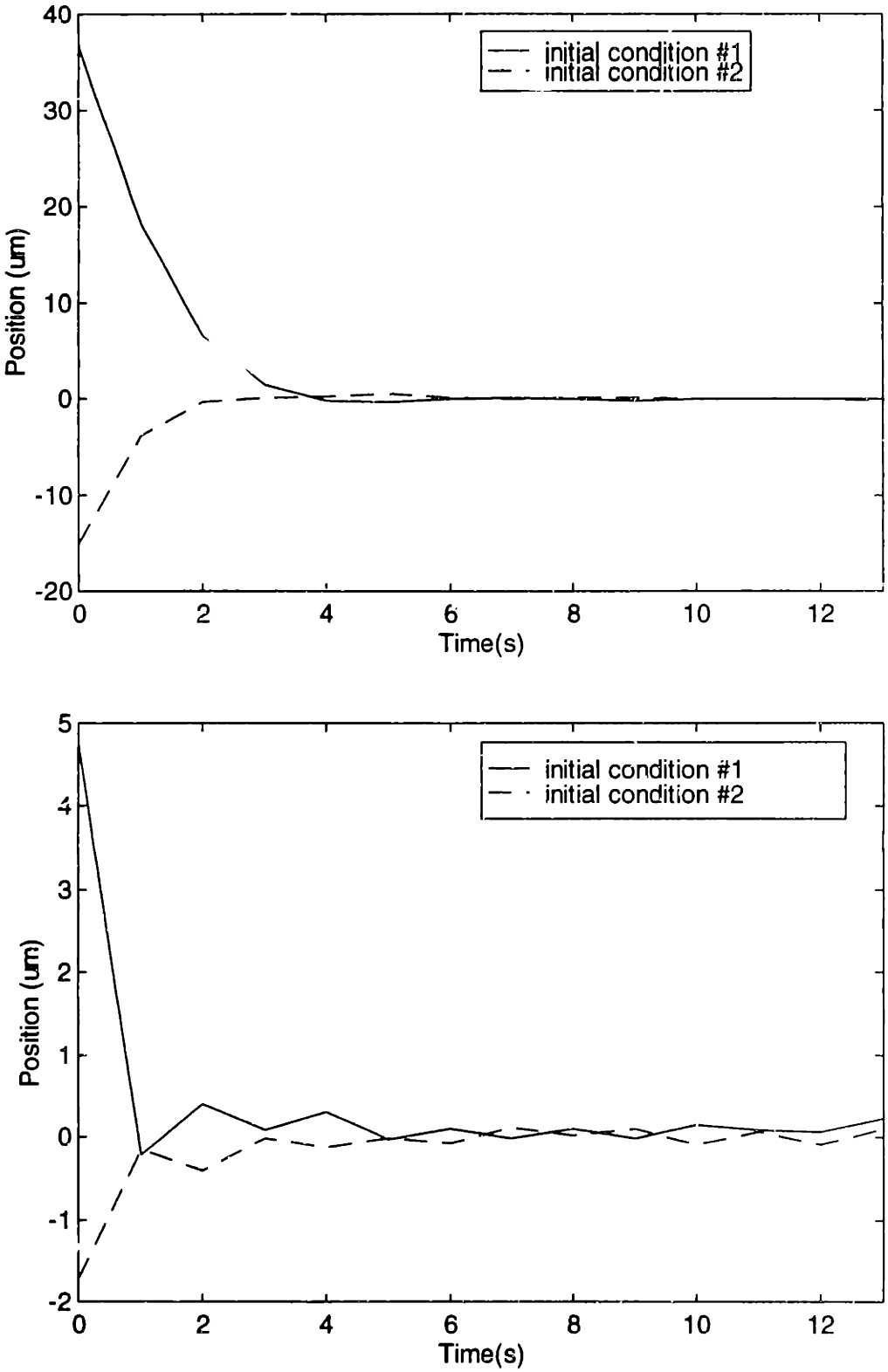

Figure 4.22 Impulse Control Response of Five-bar for xd = 0, kc=1

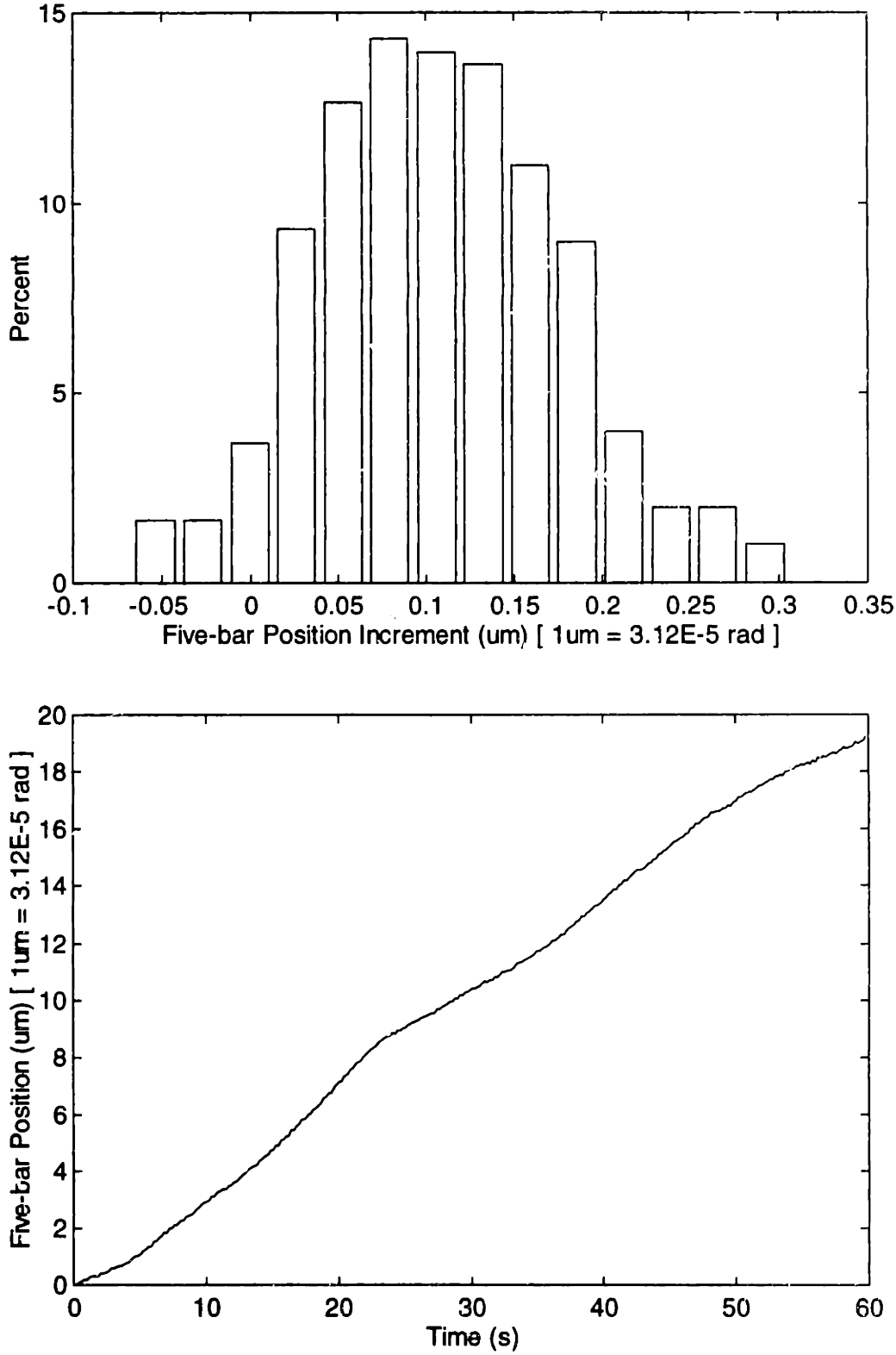

Figure 4.23 Impulse Resolution Test for Five-bar

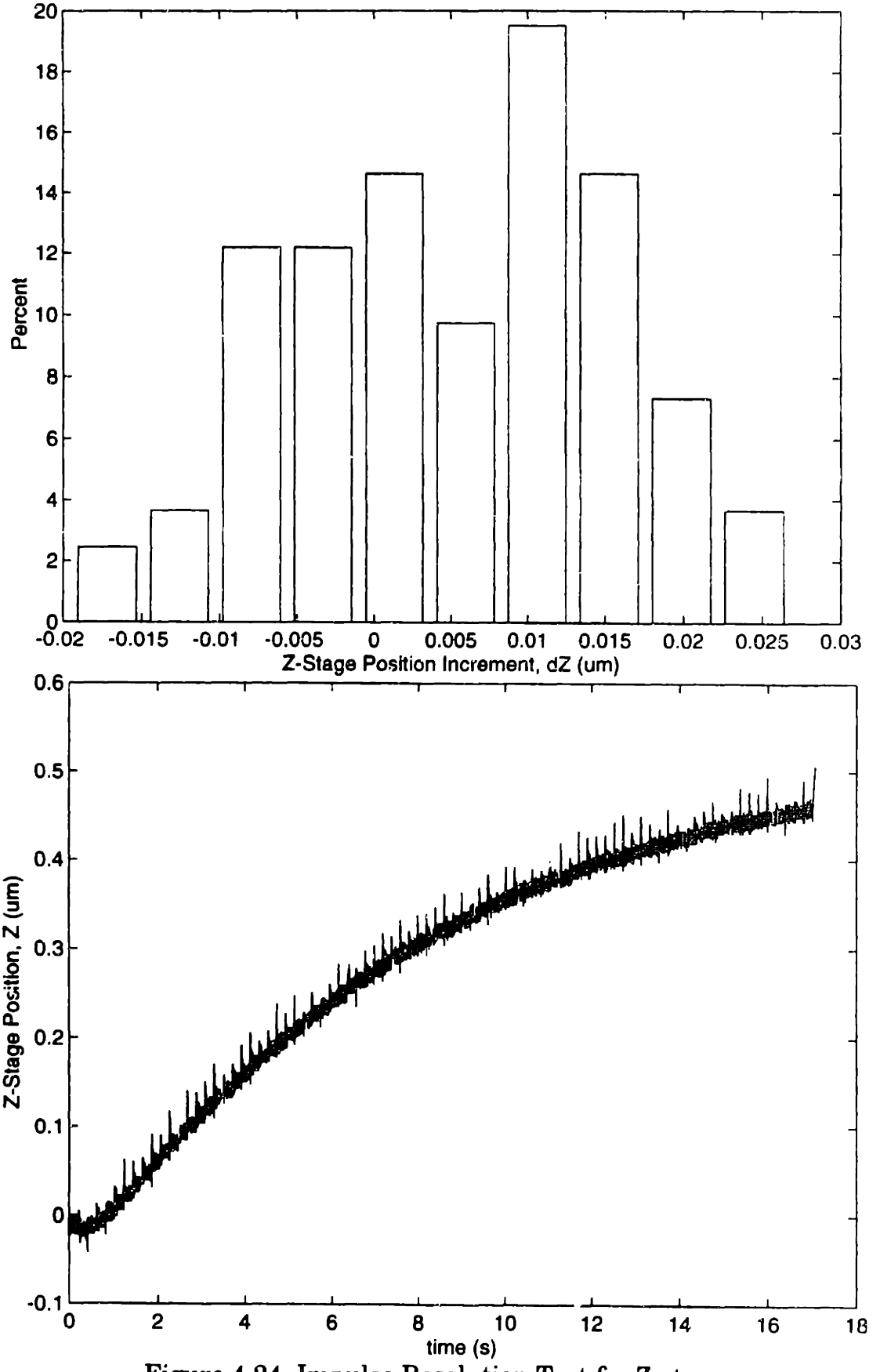

Figure 4.24 Impulse Resolution Test for Z-stage

4.3.4 Conclusions

An impulse controller was shown to be highly effective for the precise positioning of a precision mechanism with transmission flexibility, stiction, and Coulomb friction. It was shown that adding a second harmonic to the impulsive wave form could eliminate a dead zone which facilitates the development of a discrete control law. A tracking error an order of magnitude smaller than conventional linear control could consistently be obtained. In addition, it was experimentally found that the resolution of the z-stage and five-bar could be improved by a factor of 7 and 18 respectively over conventional linear control.

Further investigations could examine the effects of adding more harmonics to the input in attempt to improve performance. Varying the impulse period might also give better results and produce less excited vibrations. Alternatively, using different eigenfunctions or a radial basis function neural network may yield improved performance. Further, on-line estimation of the impulse response equation could yield improved performance and robustness to parameter variations. An analytical approximation of the system could provide insight into the system dynamics which may suggest improved control methods and indicate under what range of parameters is impulse control possible.

5. Conclusions

In this thesis control and path planning methods were developed for two macro/micro manipulators employed in a new automated fiber pigtailing process recently developed at the Manufacturing Institute at MIT. The main results are summarized as follows:

Mathematical Model of the Macro Manipulator

A mathematical model of the macro manipulator is developed that accounts for frictional effects, transmission flexibility and presliding displacement of the output inertia. It was observed that the system dynamics are highly nonlinear due to the influences of static and Coulomb friction and the nonlinear flexible transmission connecting the input and output inertia. Further, it is shown that the motor actuator dynamics of the macro manipulator are essentially decoupled due to the large gear reductions employed.

Optimal PID Control Method for the Macro Manipulator

An optimal control method based on the PID controller structure and ITAE performance index is developed. A random neighborhood search algorithm is implemented that automatically tunes the PID gains on-line to find the global minimum of the performance index. It was found that averaging the index for more than one step size increased the convergence rate by reducing the number of local minima associated with the inertia sticking near the desired position.

Transmission Windup Compensation

It is shown that the interaction of transmission flexibility of the harmonic drive motors employed in the macro manipulator with friction present produces a transmission windup effect that introduces backlash into the system. To reduce this effect a transmission windup compensation technique is developed which uses an empirical model based estimate of the transmission windup from previous input. An equivalent reversal position concept is introduced to accurately estimate the internal state of the transmission windup. It is experimentally shown that this compensation method reduces the effects of transmission windup by a factor of 8 over a broad range of operating conditions.

Resolution Characterization of the Macro Manipulator

The ability of the macro manipulator to consistently move small increments is critical for light coupling initialization and alignment. Statistical tests performed indicate that the resolution capability is 0.14um in the z direction and 3.5um in the x-y plane. This is well within the performance requirements for the AFPM process.

New Alignment Method for Pigtailing Optoelectronic Devices

A new light coupling initialization method for pigtailing optoelectronic devices is presented which employs a large diameter core sensing fiber to decouple an inherently four dimensional search process into successive two dimensional searches. This method is shown to reduce the time required by over two orders of magnitude while substantially increasing robustness to process uncertainties.

Two Nonlinear Control Methods for Precision Applications

An investigation of two promising nonlinear control methods for precision applications is performed. In particular, a feed forward neural network controller is developed that can linearize the hysteresis behavior of piezoelectric actuators employed in the micro manipulator. It is shown that this control scheme can increase open loop accuracy by a factor of 20. Further, a controller that uses torque impulses to move the macro manipulator very small increments is developed. It is shown that adding a second harmonic to the impulsive waveform can eliminate a dead zone which facilitates the development of a discrete control law. Experimental results indicate that this control method can improve the resolution of the macro manipulator by more than an order of magnitude.

References

[1] Sharon, Andre, "The Macro/Micro Manipulator: An Improved Architecture for Robot Control", PhD Thesis, Mechanical Engineering Department, Massachusetts Institute of Technology, 1988.

[2] Spong, M. W., Vidyasagar, M., "Robot Dynamics and Control", Wiley, New York, 1989.

[3] Armstrong-Helouvry, B., and Dupont, P., and De Wit, C. C., "A Survey of Compensation Methods for the Control of Machines with Friction", Automatica, July 1994.

[4] Dorf, R. C., "Modern Control Systems", Sixth Edition, Addison-Wesley, New York , 1992.

[5] Brogan, W. L., "Modern Control Theory", Third Edition, Prentice-Hall, New Jersey, 1991.

[6] Franklin, G. F., Powell, J. D., and Workman, M. L., "Digital Control of Dynamic Systems", Second Edition, Addison-Wesley, New York , 1990.

[7] Slotine, J. E., Li, W., "Applied Nonlinear Control", Prentice Hall, New Jersey, 1991.

[8] Bassiouny, E., Ghaleb, A. F., and Maugin, G. A., "Thermodynamical Formulation for Coupled Electromechanical Hysteresis Effects - I. Basic equations .", Int. J. Engng Sci. v26, 1279-1295, 1988.

[9] Yang, S., and Tomizuka, M., "Adaptive Pulse Width Control for Precise Positioning Under the Influence of Stiction and Coulomb Friction", ASME J od Dynamic Systems, Measurement and Control, 110(3), 221-227, 1988.

[10] Hojjat, Y., and Higuchi, T., "Application of Electromagnetic Impulsive Force to Precise Positioning", Int. J. Japan Soc. Precision Engineering, 25(1), 39-44, 1991.

[11] Slocum, A. H., "Precision Machine Design", Prentice Hall, New Jersey, 1992.

[12] Hentschel, C., "Fiber Optics Handbook", Hewlett-Packard, GmbH, 1988.

[13] Hämeenanttila, Tiina, "Design and Implementation of Fiber Pigtailing Automation", MS Thesis, Mechanical Engineering Department, Massachusetts Institute of Technology, 1996.